Coupled diffusion and mechanics in battery electrodes

Ahmadreza Eshghinejad

A dissertation submitted in partial fulfillment of the
requirements for the degree of

Doctor of Philosophy

University of Washington

2016

Reading Committee:

Jiangyu Li, Chair

Mark E Tuttle

Junlan Wang

Program Authorized to Offer Degree:
Mechanical Engineering

University of Washington

Abstract

Coupled diffusion and mechanics in battery electrodes

Ahmadreza Eshghinejad

Chair of the Supervisory Committee:
Professor Jiangyu Li
Department of Mechanical Engineering

We are living in a world with continuous production and consumption of energy. The energy production in the past decades has started to move away from petrochemical sources toward sustainable sources such as solar, wind and geothermal. Also, the energy consumption is further adapting to the sustainable sources. For instance, in recent years electric vehicles are growing fast that can consume sustainable electric energy stored in their batteries. In this direction, in order to further move toward sustainable energy, materials are becoming increasingly important for storing electric energy. Although, currently the technologies such as Li-ion batteries and solid-oxide fuel cells are commercially available for energy applications, improvements are crucial for the next generation of many other technologies producing or consuming sustainable energies.

A critical aspect of the electrochemical activities involved in energy storage technologies such as Li-ion batteries and solid-oxide fuel cells is the diffusion of ions into the electrode materials. This process ultimately governs various functional properties of the batteries such as capacity and charging/discharging rates. The first goal of this dissertation is to develop mathematical tools to analyze the ionic diffusion and investigate its coupling with mechanics in electrodes. For this purpose, a thermodynamics-based modeling framework is developed and numerically solved using two numerical methods to analyze ionic diffusion in heterogeneous and structured electrodes.

The next goal of this dissertation is to develop and analyze characterization techniques to probe the electrochemical processes at the nano-scale. To this end, the mathematical models are first employed to model a previously developed Atomic Force Microscopy based technique to probe local electrochemical activities called Electrochemical Strain Microscopy (ESM). This method probes the activities by inducing AC electric field to perturb ionic activities and measuring the surface vibrations. Different aspects of this technique are analyzed and the limitations are discussed. Such limitations moves the dissertation toward development of a new technique for probing the electrochemical activities, to overcome the previous limitations, called Scanning Thermo-ionic Microscopy (STIM). In this method, the local activities are probed by inducing AC temperature oscillations to perturb ionic activities and measuring the surface vibrations. The principle mathematical analysis of the coupled governing equations and the method of probing electrochemical activities are discussed in detail. Also, the method is implemented into the AFM hardware/software and the STIM response is confirmed using experiments on $LiFePO_4$ and Sm-doped Ceria as well-known battery and fuel cell electrodes. The STIM method provides a clean method for analyzing energy storage materials and designing novel nano-structured materials for improved performance.

Finally, conclusion of the presented work is discussed in the last chapter and the future works to continue the development of the modeling and experiments are listed.

TABLE OF CONTENTS

LIST OF FIGURES

LIST OF TABLES

ACKNOWLEDGMENTS

First of all, I would like to thank my family who have always been the greatest support in my life. During the past four years they have continuously sent their love from thousands miles away.

I would like to express my gratitude to my advisor, Dr. Jiangyu Li, who has supported me with his guidance and expertise. I could not accomplish my present achievements without his supports and motivation.

Besides, I would like to express my sincere regards to the committee members, Professors David Ginger, Mark Tuttle and Junlan Wang for their guidance and time for evaluating my work.

I also would like to acknowledge UW Clean Energy Institute for the financial and intellectual support.

A spacial thank you to the members of the Multifunctional Material Laboratory for all the discussions and friendship during the past four years.

Last but not least, I would like to thank my friends all over the world and specially my friends in Seattle for their true friendship and support. I lived a great four years with them.

,

Chapter 1

INTRODUCTION

1.1 Motivation

The energy storage in the global landscape has become one of the limitations of many of the recent technologies. The demand for uninterrupted motion and communication in our world urges the necessity for energy storage systems with high energy density and specific power in order to provide the energy required for portable devices. Currently in portable electronics, battery modules are considered as the heaviest, bulkiest and costly parts [5]. Furthermore, recent technologies are gradually moving away from the traditional gasoline-fueled energy sources toward the more environmentally friendly sources and the demand for energy storage devices with high power density and fast charging time is increasing. In the recent years, the demand for electric vehicles is increasing dramatically while the main challenge for this industry is producing cost effective batteries with high energy and power density with a long life cycle. Also, as the clean energy sources such as solar cells and wind turbines are providing energies, high capacity with compatible power availability energy storage systems are crucial in integrating such sources in the power grids. [45].

Improvements in all aspects of energy storage technologies are essential for technologies not only in our planet, but also for space explorations [85]. In the International Space Station, all the activities from communication to scientific studies rely on the electrical energy that harvested from solar panels. In the ambitious Mars exploration and colonization missions that NASA and SPACEX are working on for the next decades, the unique source possible of energy is solar and stored in batteries. For development of such emerging technologies, the

batteries are required not only to have high density but also to resist temperature variations and radiation activities [96].

In order to meet the wide range of required improvements, possible forms of the next generation of energy storage devices are need to be investigated. Probably, there is not unique solution that can address all the shortcomings. Therefore, all forms of energy storage, from batteries to fuel cells are required to be investigated to be able to approach to the optimum solutions.

Among all energy storage systems, Li-ion batteries have shown the highest energy density, superb cycling stability and design flexibility [98]. A battery is made up several cells connected in parallel or series which provide the required electric potential and capacity. Each battery cell is composed of two electrodes separated by an ion conducting electrolyte and an external circuit which conducts the electrons. With the chemical reactions at the surface of the electrodes, electrons are produced or consumed and flow through the circuit and proved electrical power. The amount of energy a battery can provide is measured either per unit weight ($W\,h\,kg^{-1}$) or per unit volume ($W\,h\,l^{-1}$). As shown in Figure 1.1, among all the various existing technologies Li-based batteries have the highest energy density which explains the 63% of the worldwide sales in the portable batteries market [98]. However, the recent researches in advancing the performance of the Li-ion batteries has been criticized for the slow growth and the electrodes as the key part of the batteries are considered to be the weak point.

A possible direction that can transform all the developments of batteries and their electrodes is nano-structured materials [67]. Because of the specific surface structure, the non-structured materials show very different mechanical and chemical properties not found in bulk materials. For the Lithium-Ion batteries, the nano-structured electrodes could affect the chemical reactions at the surface due to the surface effects [4] and improve the cycling sta-

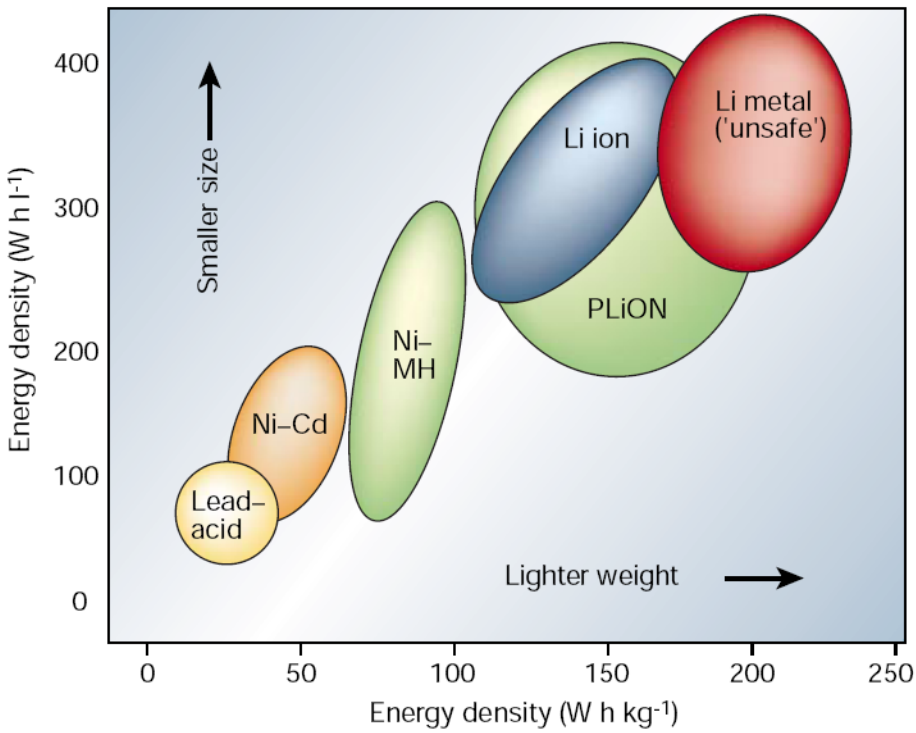

Figure 1.1: Comparison of different battery technologies in terms of volumetric and gravimetric energy density [98].

bility of the electrodes [39]. Furthermore, the geometry condition could increase the amount of ions the electrode can be accommodated during the charging condition. The higher surface area could drastically improve the total reaction rate and possibly the electronic conductivity of the electrodes[109].

One of the main goals of this dissertation is to develop a thermodynamics-based continuum model for the coupled diffusion and mechanics in battery electrodes and analyze the effect of nano-structure modification on the performance of the electrodes. For this purpose, the numerical tools to solve the governing PDEs was developed. Furthermore, the recent wide application and utilization of nano-structures in developing the new electrodes geared the research toward the electrochemical characterization of the electrode materials at the

nano-scale. The method that is available for such characterization is an Atomic Force Microscopy based method called Electrochemical Strain Microscopy [10, 53]. This method is a relatively new method that combines AC and DC electric bias applied to the AFM tip to probe electrochemical activities at the nano-scale. This dissertation partly investigates different aspects of this method both mathematically and experimentally. However, there are some difficulties involved in the ESM probing because of applying electric bias to the AFM tip. The shortcomings of this method derived my research toward developing a new AFM-based method to address the issues. The new method combines the available thermal probing with the fundamentals of ionic motion, to probe the electrochemical activities at the nano-scale.

As the battery electrode materials development and characterization is becoming increasingly important for the future of many technologies. The suggested future works in this area are presented in the last chapter.

1.2 Basics of Li-ion battery

Li-ion battery converts chemical energy into electrical energy and vice-versa. Li ions can react and diffuse into any material, however a material which conduct electrons can be used as an electrode. When two intercalation electrodes are contacted the Li-ions diffuse from the electrode with higher chemical potential to the electrode with lower chemical potential. This chemical potential difference is the driving force in Li-ion batteries.

Earlier lithium ion rechargeable batteries were based on an intercalation electrode as the cathode and lithium metal as the anode, taking advantage of the low density and electropositivity of the lithium metal [2]. However, the safety issues restricted the development of this technology. Current Li-ion batteries use two intercalation compounds as the cathode and anode electrodes, and are separated by an electrolyte which conducts the ions but not

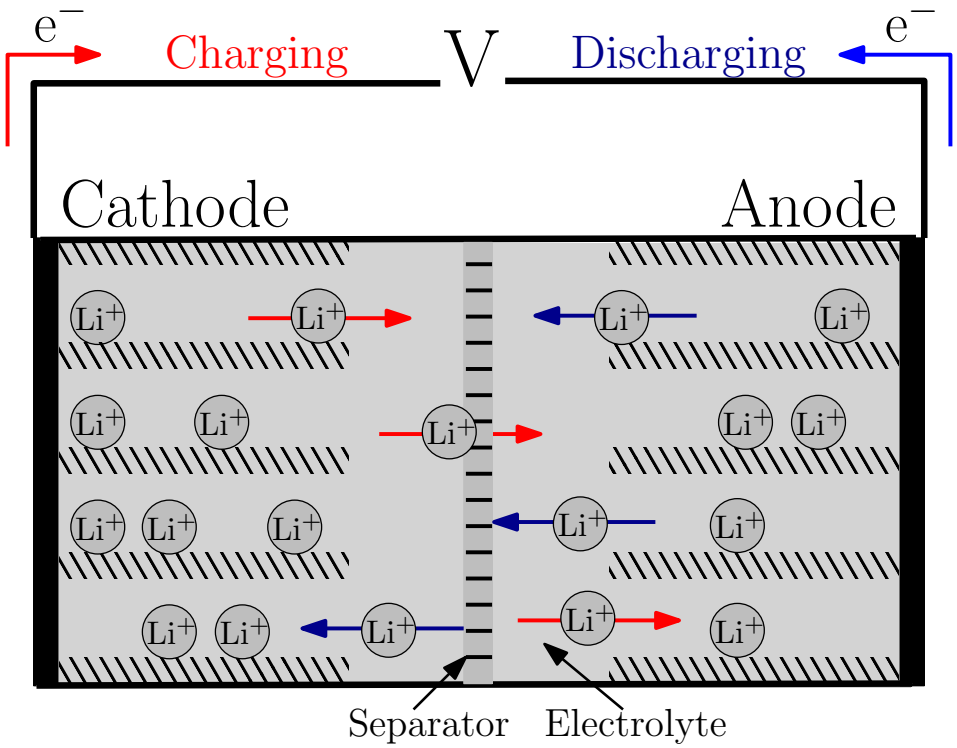

Figure 1.2: Schematic of lithium-ion battery operation

electrons. In the fully charged state as shown in Figure 1.2, all the mobile Li-ions are accumulated inside the anode. By discharging the battery, the chemical potential difference between the two electrodes drives the Li-ion to diffuse out of the anode, move them through the electrolyte toward the cathode and eventually derives the intercalation and diffusion into the cathode. The electrochemical reactions occurring over the electrode-electrolyte interface produce or consume electrons which are required to pass through an external circuit.

Although the working concept in Li-ion batteries is simple, the physics of the processes are complicated, involving diffusion and migration of Li-ions in the electrolyte and electrodes, electrochemical reactions at the electrode-electrolyte interface, and intercalation of Li-ions into and out of the electrodes. The commercial Li-ion batteries consist of a lithium metal oxide, such as $LiCoO_2$ as the cathode, graphite as the anode, a polypropylene separator

which electrically separates the cathode and anode, and an organic electrolyte [93].

1.3 Coupled electrochemistry and mechanics

The main body of this dissertation is about the coupling between electrochemistry and mechanics in battery electrode materials. Insertion of atoms into a solid host lattice induces volume expansion. In case of inhomogeneous volume expansion or mechanically constrained condition, the insertion-induced stress arises [46, 118]. A well-known example is during the insertion of lithium atoms into a spherical host particle that the stress is generated due to the higher volume expansion in the outer shell compared to the core. Christensen and Newman developed a continuum model for the insertion/extraction -induced stress of lithium atoms into a spherical carbon particle [27]. They predicted a compressive stress in the outer shell and expansive in the core during the insertion and vice versa during the extraction. Zhang et al. modeled the intercalation-induced stress in LiMnO4 electrodes of spherical and ellipsoidal particles [39]. They showed that the larger particle size and larger insertion current generates higher stress within particles. Chen and Verbrugge and coworkers developed analytical linear-elastic solutions for diffusion induced stress under various conditions [106, 33, 23]. They developed an analytical expression for the stress evolution in an spherical battery electrode under galvanostatic and potentiostatic charging conditions [22].

The developed stress results in crack propagation and eventually lead to fracture and capacity fade of electrode. High insertion rates don't let the ions to homogenize in the electrode particles leading to large enough stress to fracture the electrodes [14, 107]. Such insertion-induced stress and the resultant cracks formation occurs almost all types of electrodes as shown Figure 1.3. Intercalation induced deformation and the resultant fracture criteria limits the applicable materials for high capacity electrodes [55, 115]. Today, in the commercial Li-ion batteries, graphite is the anode material which accommodates one Li-ions

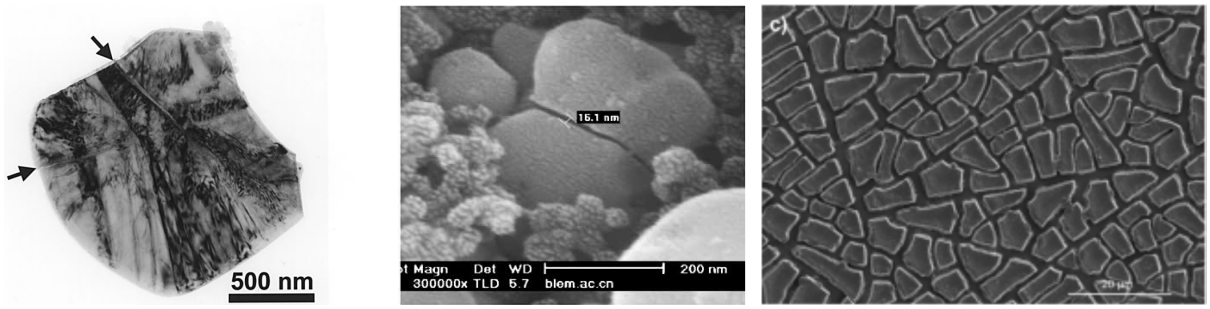

(a) (b) (c)

Figure 1.3: Li insertion-induced stress caused cracks a) in $LiCoO_2$ particle [108], b) $LiFePo_4$ particles [107] and c) Si thin film [66]

per six carbon atoms. However Si accommodates 4.4 Li atoms per atom of the host, but experiences about 400% expansion resulting in fracture of the electrode leading to capacity fade after a few cycles.

Moreover, such electrode mechanics also affects the electrochemistry in the Li-ion batteries. The mechanical energy associated with the insertion contributes to the free energy influences the Lithium atom motion in the electrode [61]. Numerical results have shown that contribution of the stress-induced diffusion enhances the diffusivity of the solute atoms and has concentration homogenization effect over electrode [27]. The electrode stress state also affects the electrochemical reactions occurring at the electrode-electrolyte interface [41, 95], and the interface progress in two-phase lithiation materials [119, 69].

There are also numerous experimental works that confirm the effect of mechanics on the electrochemistry. Arnold et. al. [17] reported that the mechanical pressure applied to the battery affects the capacity of battery as shown in Figure 1.4(a). The battery cell under higher applied pressure shows higher capacity fade over the cycling of the cell . This experiments directly confirm the coupling between mechanics and electrochemistry in battery cells. In another example, Kim et. al. [56] built a battery cell for mechanical energy harvesting.

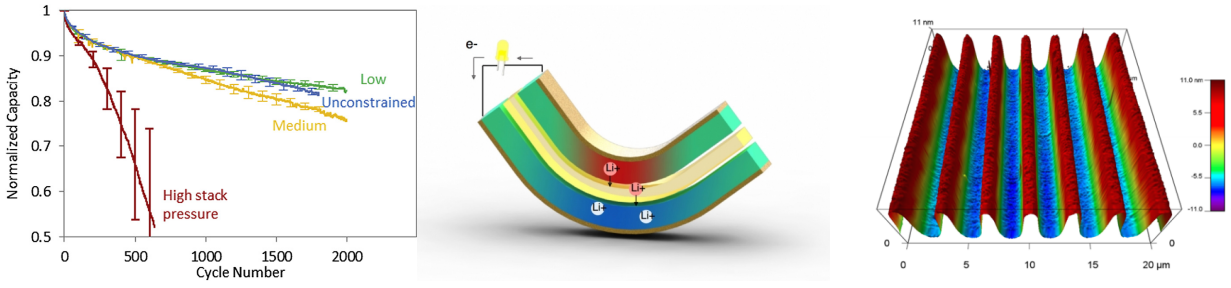

(a) (b) (c)

Figure 1.4: Effect of mechanics on electrochemistry. a) Capacity fade in lithium-ion cells under different levels of pressure [17]. b) Harvester mechanical bending energy via stress induced ionic transfer between electrodes [56]; and c) the surface topography of patterned electrodes with reduced stress and high capacity [109].

In this configuration of cell, as shown in Figure 1.4.(b), bending of the cell creates a difference between the stress state in the two electrodes that results in ionic transport between electrodes and power generation. In the third example, Wang et. al. [109] modified the topography of a graphite electrode by imprinting a surface pattern as shown in Figure 1.4.(c) which lead to relaxing the stress distribution during the ionic intercalation. They found that this stress relaxation could improve the battery capacity and the battery cell with patterned electrodes showed higher capacity compared to the bulk electrode (unpatterned). In Chapter 4 of this dissertation, the effect of structured electrodes on the capacity is investigated.

1.4 Atomic force Microscopy

Throughout this dissertation, in Chapter 6 and 7, the developed framework is used for simulation and experimentation of the ionic motion in an atomic force microscopy hardware. Atomic force microscopy or scanning probe microscopy is a microscopy hardware with the resolution of nano-meter, based on the principle of touching or feeling the sample. As

schematically shown in Figure 1.5, the AFM consists of a cantilever with a sharp tip at its end that is usually in contact with the sample that is precisely positioned with a piezoelectric actuator. The deformation of the sample surface causes bending of the cantilever and that is precisely measured through a laser-photodiode system. A feedback electronic controls the vertical movement of the cantilever for different purposes (e.g. sample topography mappings).

The simplest mode of measurement for AFM is mapping the topography of the sample at the nano-scale resolution. At this mode, as the stage piezoelectric actuator moves the sample line by line, a certain deflection is maintained for the cantilever through the laser-photodiode system and the feedback system that controls the vertical movement of the cantilever. By mapping the vertical movement of the cantilever to keep certain deflection, the topography mapping of the sample is formed.

Furthermore, various modes have been developed by researchers to probe physical properties of the materials. For example, the magnetic force microscopy (MFM) reveals the magnetic nano-structure, electrostatic force microscopy (EFM) maps the electric charge distribution of the sample and conductive mode (ORCA) maps the electric conductivity structure.

A well-known probing technique is called piezoelectric force microscopy (PFM), and is used to map the ferroelectric nano-structure of materials. In this technique, an AC bias is applied to the probe that results in an electric field beneath the tip that produces a piezoresistive deformation corresponding to the ferroelectric state at that location. The deformation is measured by the cantilever and laser-photodiode system and mapping of the deformation reveals the nano-structure of the ferroelectric domains.

Another mode is Electrochemical Strain Microscopy (ESM), that is recently developed to probe the ionic materials. In 2010, Balke et al. at Oakridge national laboratory introduced the ESM techniques to map the ionic transport in the electrodes at nanometer scale [11, 9].

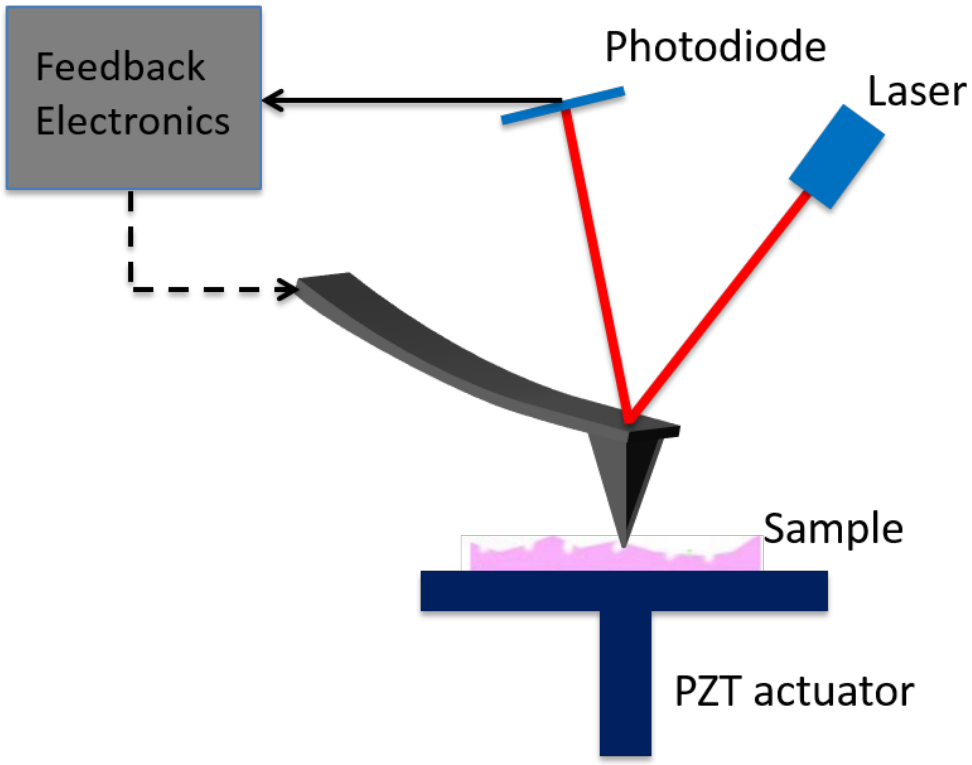

Figure 1.5: Schematic of atomic force microscopy (AFM)

In this technique, the coupling between ion concentration and electrode lattice strain (Vegard strain) is exploited to map the ion transport with high resolution. Similar to PFM, a periodic bias is applied to the scanning probe to locally induce intercalation/de-intercalation of ions resulting in periodic deformation of the electrode surface beneath the tip proportional to the ionic concentration. This deformation is measured by the same tip and produces an ionic transport activity map with nanometer resolution providing detailed insight to the electrode operation. In chapter 6, the ESM technique is further discussed and the modeling framework is applied to investigate different aspects of this technique. In chapter 7, another novel AFM-based technique is developed to probe the ionic materials. This technique resolves some of the shortcomings of the ESM technique.

1.5 Dissertation overview

This dissertation covers the research materials over four years on modeling and characterization of materials for energy storage. A thermodynamics based continuum modeling framework for the coupled diffusion and mechanics in solid electrodes are adopted and the detailed derivation is explained in Chapter 3.7. The ionic motion model as well as surface kinetics models are explained in this chapter.

In Chapter 3 and Chapter 4 the developed model is solved numerically to investigate heterogenous and complex geometry electrodes that analytical solutions are unable to provide solution. In 3, Fast Fourier transform and finite difference methods are used to numerically solve the governing equations and investigate heterogeneous electrodes. The advantages and disadvantages of the developed numerical methods are discussed. In Chapter 4, the governing equations are implemented into Comsol Multiphysics to numerically investigate the electrodes with various complex geometries and boundary conditions. In Chapter 5, the developed modeling framework in Comsol is combined with automatization programming in

Matlab to study the effect of geometry designs on its performance. Finally, an electrode geometry with optimum performance is introduced.

Chapter 6 is devoted into analyzing the Electrochemical Strain Microscopy technique for analyzing ionic materials. The method is analyzed by extending the developed model in previous chapters and numerical implementation in Comsol. The results are verified by experimental measurements. The limitations of this technique are discussed that motivates the next chapter for developing a novel technique for probing electrochemical activities.

In Chapter 7 a novel AFM-based probing technique, Scanning Thermo-Ionic Microscopy, is developed on the foundations of the previous chapters of this dissertation. The analysis and implementation methods are described in details. Also, the results of probing a battery electrode material, $LiFePo_4$, and a fuel cell electrode material, Ceria, using this technique are presented for validation.

Finally, in Chapter 8, the conclusion of this dissertation is described and the future work remarks are listed.

Chapter 2

MODELING FRAMEWORK

2.1 Introduction

The associated elastic energy to the volume expansion upon atom insertion into a host material alters the thermodynamic equilibrium state. The fundamental framework for the thermodynamic equilibrium of diffusing solute atoms in a network structure of the host solid is first established by the works of Larche and Cahn and Li et al. [61, 64]. In their model, the equilibrium conditions within the solid host places conditions on the chemical potential, temperature and stress. They assumed a network for the solid host, which permits the definition of a displacement, and the associated strain. They studied various conditions on the stress, composition and chemical potential. For example, they showed that the application of stress under restricted chemical potential produces composition changes. As an example they predicted a composition variation due to an edge dislocation stress field in a constant composition material. They introduced a modified chemical potential of the diffusing species under spherical composition strain considering the stress field contribution. Note that this form of chemical potential is only valid for small elastic and compositional strains.

In the continuation of this work, Wu proposed an improved diffusion chemical potential where the trace of the Eshelby stress tensor instead of Cauchy stress tensor contributes to the stress-dependent chemical potential [112]. They identified three states of initial (reference state), stress-free and spatial states. All the thermodynamic quantities are uniform in the reference state and deviation of composition from the reference state causes volumetric expansion. In case of uniform composition deviation with no mechanical constraint produces

no stress in the solid. However, if the volume expansion is not uniform or the solid is mechanically constrained, the elastic deformation needs to be generated to ensure the compatibility of deformation.

In a more comprehensive study, Cui et al. modified the stress-dependent portion of the chemical potential considering nonlinear, inelastic and finite deformation [29]. In their modified relation, the contributions of the stress tensor, composition dependent stiffness tensor and strain energy show up in the chemo potential. The proposed chemical potential reduces to the proposed formulation by Wu [30], in case of elastic stiffness not a function of composition, and reduces to the proposed formulation by Larche and Cahn in case of small elastic and compositional strain. They implemented their relation numerically to predict the lithium insertion-induced elastic-plastic stress in a spherical silicon particle. They predicted the hoop stress at the surface of the particle to be compressive at the beginning of insertion but evolve to tensile stress at the later stages of insertion due to the large expansion of the core. Such loading condition predicts crack formation at the surface of the Si particle.

There are numerous authors considering the stress contribution in their chemical potential modeling that affects the predicted diffusion behavior. Christensen and Newman included the stress-dependent chemical potential in their mathematical model to predict the mechanical compressive and expansive stress during insertion and extraction of ions into/out of a spherical electrode [27]. Their results indicated that accounting for stress-induced diffusion results in a more gentle concentration distribution within the particle as shown in Figure 1.b. The enhanced diffusion effect results in less maximum stress and lattice mismatch in the particle.

In a recent study, Haftbaradaran et al. presented a coupled continuum model for the highly nonlinear diffusion of non-dilute solute atoms in a solid host and validated the results using atomistic simulations [42]. They modeled a special case of infinitely extended freestand-

ing electrode nickel host, which was subjected to uniform flux of hydrogen atoms from the top and bottom surfaces and studied the effect of various conditions on the concentration and stress distribution. In another study they showed that coupling between concentration and mechanics can result in nonconventional electrochemistry predictions [41]. They adopted a stress-dependent energy barrier for diffusion of solute atoms diffusivity. Such representation of diffusivity under galvanostatic charging resulted in a critical limit (function of electrode dimension and surface flux) under which the solution of concentration at the surface becomes unstable. This instability is induced by the compressive stress near the surface resulting in a slowed down diffusivity, which under galvanostatic charging leads to accumulation of ions near the surface.

In this chapter we develop a thermodynamics-based model incorporating coupled stress and diffusion of ions within electrode that is described in details in section 2.2. The model is built on the Gibbs free energy of the system and uses the chemo-mechanical potential of the system to express the ionic motion model. In constructing the free energy of the system, the effects of entropy is fully derived. A stress-induced chemical potential is also incorporated in the total chemical potential. Finally, the evolution of ionic concentration is derived, with Arrhenius kinetics adopted to address the chemical potential dependent reaction rate at the electrode-electrolyte interface.

2.2 Continuum modeling

In this section we develop a thermodynamics based model for intercalation and diffusion of ions in an electrode incorporating entropy and mechanics of intercalation.

2.2.1 Diffusion of atoms

We start by introducing the mass transport of the solute species governing the ionic motion in the host as:

$$\frac{\partial \tilde{c}}{\partial t} = -\nabla \cdot \boldsymbol{j} \tag{2.1}$$

where $\boldsymbol{j}$ is the flux of the solute species (Li ions in our case) in the unit of moles per unit area per unit time, $\tilde{c}$ is the concentration of the solute species in mole per unit volume, and t represent the time. In the current model, flux of the diffusing species in the host material is a function of the mobility and gradient of the chemical potential writes as [117, 42, 26]:

$$\boldsymbol{j} = -\tilde{c} M \nabla \mu(\tilde{c}, \boldsymbol{\sigma}) \tag{2.2}$$

where M is the mobility of the solute atoms. The chemical potential of atoms is denoted by μ, which is a function of concentration and stress field ($\boldsymbol{\sigma}$) in the system, and is required to be determined from the free energy of the system.

Gibbs free energy of the system:

In order to obtain a realistic model for the concentration distribution in electrode, we need to characterize the process accurately. For this purpose, we follow an approach for breaking the process into the basic thermodynamic components [15]. Assuming only one mobile species, which hope between the host sites, the Gibbs free energy of the system is introduced as:

$$G(\sigma_h, T) = U - TS - \sigma_h V \tag{2.3}$$

where U is the internal energy of system and T and S are the absolute temperature and entropy of the system respectively. The volume of the system and the hydrostatic stress are

represented by V and σ_h, respectively. The chemical potential of the solute species is then found as:

$$\mu = \frac{\partial G}{\partial M}\Big|_{\sigma_h,T} = \frac{\partial U}{\partial M}\Big|_{\sigma_h,T} - T\frac{\partial S}{\partial M}\Big|_{\sigma_h,T} - \sigma_h\frac{\partial V}{\partial M}\Big|_{\sigma_h,T} \tag{2.4}$$

where M represents the amount of solute ions in the system in moles. In the current model, we assume that the internal energy of the system does not change upon insertion of ions into the host lattice. This is a valid approximation for the electrode materials not experiencing phase separation (e.g. graphite), which is assumed in numerous related works [63, 117].

Entropy:

Based on the standard thermodynamics theory, the entropy of a system is related to all possible combinations of the solute atoms in the host lattice. Note that the total number of lattice host vacancies are fixed throughout the intercalation process represented by $N_t = M_t N_A$. Also the number of occupied sites are represented by $N = MN_A$ where N_A is the Avogadro number. The number of possible configurations can be then expressed as:

$$W(c) = \frac{N_t!}{N!(N_t - N)!} \tag{2.5}$$

For each ion host, the same probability is applied and the ion-ion intercalation is neglected in the current entropy calculation. Hence the entropy difference between the host without and with the intercalated ions read as:

$$\Delta S(N) = k_B \ln W = k_B \ln \frac{N_t!}{N!(N_t - N)!} \tag{2.6}$$

where k_B is the Boltzmann constant. The entropy change due to adding another ion to the system can be found by subtracting the entropy of a system with $N+1$ ions and the reference

system with N number of ions where $(0 < N < N_t - 1)$. The entropy change due to adding a mole of ions in a constant volume can be found as:

$$\frac{\partial \Delta S}{\partial M} \approx N_A \frac{\Delta S(N+1) - \Delta S(N)}{1} = -R \ln \frac{N+1}{N_t - N} \tag{2.7}$$

Note $R = N_A \, k_B$ is used. Since the constant volume for small displacements is equivalent to constant pressure:

$$\frac{\partial \Delta S}{\partial M}\Big|_{\sigma_h, T} = -R \ln \frac{c + 1/N_t}{1 - c} \tag{2.8}$$

where c is the fractional filling of ions defined as $c = \frac{\tilde{c}}{c_{max}}$ that is referred as concentration throughout this chapter. Note that $1/N_t \ll c$ assumption results in neglecting the $1/N_t$ term.

A different approach in expressing the entropy of nondilute solute atoms in a host material is to construct the entropy of binary mixing of the solute atoms and the vacancies in the host. The resulting entropy variation in the material can be expressed as:

$$\Delta S_{mix} = M_t R[c \ln c + (1 - c) \ln(1 - c)] \tag{2.9}$$

where the first term represents the entropy of solute atoms and the second term represents the entropy of the vacancies in the host material. The chemical potential of the mixed solution can be found as:

$$\frac{\partial \Delta S}{\partial M} = R \ln \frac{c}{1 - c} \tag{2.10}$$

Chemical potential

Given the relation for the entropy of the system, the Gibbs free energy variation of the system due to intercalation of M moles of ions into host can be written as:

$$\Delta G = M\mu_0 - T\Delta S - (V_0 + \Omega M)\sigma_h \tag{2.11}$$

where μ_0 is the chemical potential of an infinitely dilute solution. We assumed that the intercalation of ions results in a volume expansion proportional to the partial molar volume, Ω with unit $\mathrm{m}^3.\mathrm{mol}^{-3}$, and the amount of ions, which agrees with the Vegard's law. The chemical potential of the system can then be written as:

$$\mu = \frac{\partial \Delta G}{\partial M} = \mu_0 + RT \ln \frac{c}{1-c} - \Omega\sigma_h \tag{2.12}$$

At the atomistic scale, diffusion of solute atoms is a series of jumps between vacancies of the host lattice. However the solute atoms need to overcome the energy barrier caused by the interactions with the neighboring atoms. Atomistic simulations reveal the strong dependency of the activation energy of diffusion on internal stress [79], which is also referred as strain-dependent mobility by Aziz et al. [8]. The energy barrier decreases with a tensile stress acting on the area of diffusion and increases with compressive stress. Hence, the modified diffusivity D as introduced by Haftbaradaran et al. [42] takes the form:

$$D = D_o e^{\beta\alpha\Omega\sigma_h/RT}, \tag{2.13}$$

where D_0 is the diffusivity in the absence of stress and α is a positive dimensionless coefficient determining the linear dependency of diffusion activation energy on hydrostatic stress.

Finally, the in order to plug back the chemical potential into the Fick's law, one can

derive the gradient of chemical potential as,

$$\nabla\mu = RT\frac{\nabla c}{c(1-c)} - \Omega\nabla\sigma_h. \tag{2.14}$$

which gives the ionic flux,

$$\boldsymbol{j} = D_o e^{\beta\alpha\Omega\sigma_h/RT}\big(-\frac{\nabla c}{1-c} + \beta\frac{\Omega}{RT}c\nabla\sigma_h\big). \tag{2.15}$$

Considering balance of ionic species for an infinitesimal volume, we obtain

$$\frac{\partial c}{\partial t} = -\nabla\cdot\boldsymbol{j} = \nabla\cdot\left[D_o e^{\beta\alpha\Omega\sigma_h/RT}\big(\frac{\nabla c}{1-c} - \beta\frac{\Omega}{RT}c\nabla\sigma_h\big)\right], \tag{2.16}$$

which governs the evolution of ion concentration.

2.2.2 Interface reaction

For the electrochemical reaction at the interface between electrode and electrolyte, we adopt what was introduced by Bazant et. al. [95], that the reaction rate is governed by Arrhenius kinetics. The activation energy is taken as the chemical potential difference across the electrode-electrolyte interface, which provides the thermodynamic driving force. In contrast, in the standard models of interfacial kinetics, such as Butler-Volmer equation [35], the activation energy only depends on the electrostatic potential difference across the electrode-electrolyte interface. Accordingly, the net flux into the electrode normal to the surface, with unit normal vector $\boldsymbol{n}$, is governed by the difference between insertion and extraction kinetics rates,

$$\boldsymbol{j}_s\cdot\boldsymbol{n} = k_{in}c_e e^{(\mu_e-\mu_s)/(RT)} - k_{ext}c_s e^{(\mu_s-\mu_e)/(RT)}, \tag{2.17}$$

where k_{in} and k_{ext} are the insertion and extraction reaction rates with the unit of $\mathrm{mol}\cdot\mathrm{m}^{-2}\cdot\mathrm{s}^{-1}$. Concentration and chemical potential of ions at the electrolyte exposed to the solid surface are represented by c_e and μ_e respectively, while c_s and μ_s are concentration and chemical potential of ions at the solid surface. Note that in the limit of small activation potential ($|\mu_e - \mu_s| \simeq 0$) and taking $k_{in} = k_{ext} = k$, the flux is simplified as $\boldsymbol{j}_s \cdot \mathbf{n} = k(c_e - c_s)$, which is the linearized form of the Butler-Volmer kinetics that is often used as the active surface ion flux [38, 29].

2.2.3 Mechanical equilibrium

As is well known, the diffusion of ions is coupled with molar volume change that induces the internal stress field, which in turn affects diffusion. Thus we need to solve for the stress field within the electrode. In this study the electrode material is assumed to be isotropic, homogeneous and linear elastic. It is commonly assumed that ionic insertion in the electrode generates an eigen-strain that is proportional to the concentration as

$$\varepsilon^*_{ij} = \frac{\Omega}{3} c_{max} c \delta_{ij}, \tag{2.18}$$

which generate an internal stress field

$$\sigma_{ij} = C_{ijkl}(\varepsilon_{kl} - \frac{\Omega}{3} c_{max} c \delta_{kl}), \tag{2.19}$$

where C_{ijkl} is the stiffness tensor, ε_{kl} is the total strain and δ_{kl} is Kronecker delta. Because of the relatively slow electrochemical processes in electrodes, mechanics of intercalation can be solved with quasistatic assumption. The stress field can then be solved from the mechanical equilibrium equation:

$$\nabla \cdot \boldsymbol{\sigma} = 0. \tag{2.20}$$

2.3 Nondimensionalization

In this section nondimensionalization of the governing equations is explained. We first introduce the normalized coordinate, time and hydrostatic stress,

$$\hat{\boldsymbol{x}} = \frac{\boldsymbol{x}}{b}, \quad \hat{t} = \frac{tD_o}{b^2}, \quad \hat{\sigma}_h = \frac{\sigma_h}{E}, \tag{2.21}$$

where E is the elastic modulus of the electrode and b is the reference length, taken as the width of periodic unit cell of the electrode (see next sections). In the following formulations ∇ operator acts on a domain with normalized coordinate $\hat{\boldsymbol{x}}$. Hence, the expression for the evolution of ion concentration, found in Equation 2.16, can be rewritten as:

$$\frac{\partial c}{\partial t} = \frac{1}{b}\nabla \cdot \left[D_0 e^{\beta\alpha\hat{\sigma}_h E\Omega/RT} \big(\frac{\frac{1}{b}\nabla c}{1-c} - \beta \frac{\Omega}{RT} c \frac{1}{b} \nabla E\hat{\sigma}_h \big) \right]. \tag{2.22}$$

which gives the dimensionless form of the relation for evolution of concentration,

$$\frac{\partial c}{\partial \hat{t}} = \nabla \cdot \left[e^{\beta\alpha\hat{\sigma}_h E\Omega/RT} \big(\frac{\nabla c}{1-c} - \beta \frac{E\Omega}{RT} c \nabla \hat{\sigma}_h \big) \right]. \tag{2.23}$$

Note that the dimensionless quantity $\frac{E\Omega}{RT}$ determines the coupling strength of ionic diffusion with mechanics.

Furthermore, assuming that the introduced chemical potential in Equation 2.12 is valid at the surface of electrode as well, plugging it in Equation 2.17 gives:

$$\boldsymbol{j} \cdot \boldsymbol{n} = k_{in} c_e e^{\frac{\mu_e}{RT} - \ln\frac{c_s}{1-c_s} + \frac{\beta\Omega}{RT}\sigma_h} - k_{ext} c_s e^{-\frac{\mu_e}{RT} + \ln\frac{c_s}{1-c_s} - \frac{\beta\Omega}{RT}\sigma_h} \tag{2.24}$$

that reduces to:

$$\boldsymbol{j}\cdot\boldsymbol{n}=k_{in}c_e\frac{1-c_s}{c_s}e^{\frac{\mu_e}{RT}+\frac{\beta\Omega}{RT}\sigma_h}-k_{ext}\frac{c_s^2}{1-c_s}e^{-\frac{\mu_e}{RT}-\frac{\beta\Omega}{RT}\sigma_h}. \tag{2.25}$$

Now we define the ratio of insertion to extraction as:

$$\hat{S}=\frac{k_{in}}{k_{ext}}. \tag{2.26}$$

Also, from the mass balance formulation,

$$\frac{\partial cc_{max}}{\partial\hat{t}b^2/D_0}=-\frac{1}{b}\nabla\cdot\hat{\boldsymbol{j}}j_0 \tag{2.27}$$

we find the reference flux j_0, which the extraction reaction rate is normalize with respect to,

$$\hat{K}=\frac{k_{ext}b}{D_0c_{max}} \tag{2.28}$$

Therefore, the normal component of the electrode surface flux can be found in dimensionless form as:

$$\hat{\boldsymbol{j}}_s\cdot\mathbf{n}=\hat{K}\left(\hat{S}\frac{1-c_s}{c_s}c_e e^{\frac{\mu_e}{RT}+\beta\frac{E\Omega}{RT}\hat{\sigma}_h}-\frac{c_s^2}{1-c_s}e^{-\beta\frac{E\Omega}{RT}\hat{\sigma}_h-\frac{\mu_e}{RT}}\right), \tag{2.29}$$

2.4 Conclusion

In this chapter, a continuum model for the coupled electrochemistry and mechanics in solid host electrodes was developed. The thermodynamics based model accounted for the entropy and mechanical energy associated with intercalation of non-dilute solute ions, resulting in coupled diffusion-mechanics relation with the recognition of a maximum concentration of solute ions in the host. Arrhenius type of kinetics was employed at the electrode-electrolyte

interface, with chemical potential difference serving as the activation energy, providing an ion flux normal to the electrode surface as a function of ion concentration and hydrostatic stress. Finally, the developed model is nondimensionalized to be used in the numerical methods explained in the next chapters.

Chapter 3

NUMERICAL METHODS: FAST FOURIER TRANSFORM AND FINITE DIFFERENCE

3.1 Introduction

Designing of composite electrodes consisting of one or more active and matrix materials can enhance the structural stability of electrodes [100, 32, 68]. An examples is amorphous silicon coated carbon composite which has shown advantages. The combination of high capacity Si and stability of the carbon layer is shown to be beneficial to the overall performance of the electrode. Silicon experiences 300% expansion due to lithiation which is much higher than the 10% volume expansion of the carbon layer. This provides flexibility to the capacity and the mechanical stability of the electrode. Also, there have been attempts to embed active particles (Sn, Fe, Mn) in a carbon matrix [4, 32]. A role of such electrodes is the structural stability of the material under large volume expansions which results in enhanced life cycle.

Understanding of the ionic transport in composite electrodes would provide insight for designing new electrodes. Because of the spatial variation of material properties in such electrodes the conventional analytical or numerical 1D simulations available in literature is not applicable. Therefore we need to solve the governing equations considering the full spatial dependency of the problem. To this end, we develop a numerical framework in two dimensions for planar electrodes in this chapter to simulate the physics of ionic transport in composite electrodes.

We employ the described thermodynamics-based model incorporating coupled stress and diffusion of ions within electrode. In section 3.2, the numerical discretization and imple-

mentation of the governing equations using Fast Fourier transform and Finite difference methods are described in details. The developed numerical framework is then employed to investigate ionic diffusion in a homogeneous electrode resembling bulk electrodes. Finally two heterogeneous electrode structures resembling composite materials is investigated.

3.2 Numerical methods

In this section, we explain configuration of the investigated electrodes and the employed numerical methods to solve the governing equations. In the schematic of the domain configuration shown in Figure 3.1, the electrochemical governing equations and the boundary conditions are shown in the left domain while the mechanical ones are shown in the right domain. Because of the coupling, at each time-step the eigen-strain and hydrostatic fields are calculated by the electrochemical and mechanics solvers respectively, and passed to counterpart solver. Here, we consider a unit cell of the electrode extended periodically in the lateral direction. Over the top surface, electrode is exposed to electrolyte resulting in normal ion flux, $J_s = J_0(1 - c_s)$ (considering the limiting case of kinetics) into the electrode, while the mechanics is traction free. Over the bottom surface, the normal ion flux is zero and the mechanical displacements are fixed. Also, the domain is assumed to be very long in the out of plane direction resulting in plane strain mechanical condition.

The governing equations are numerically solved using Fast Fourier Transform (FFT), in the lateral direction x, and finite difference through the thickness direction y. The governing equation for the concentration of ions can be expressed as:

$$\frac{\partial c}{\partial t} = \nabla \cdot (D\nabla c - c\nabla\tau) \tag{3.1}$$

where, the stress is embedded in τ. To integrate this equation we used Matlab ODE 45. For the differentiation in the x direction we used Fast Fourier method for the periodic condition.

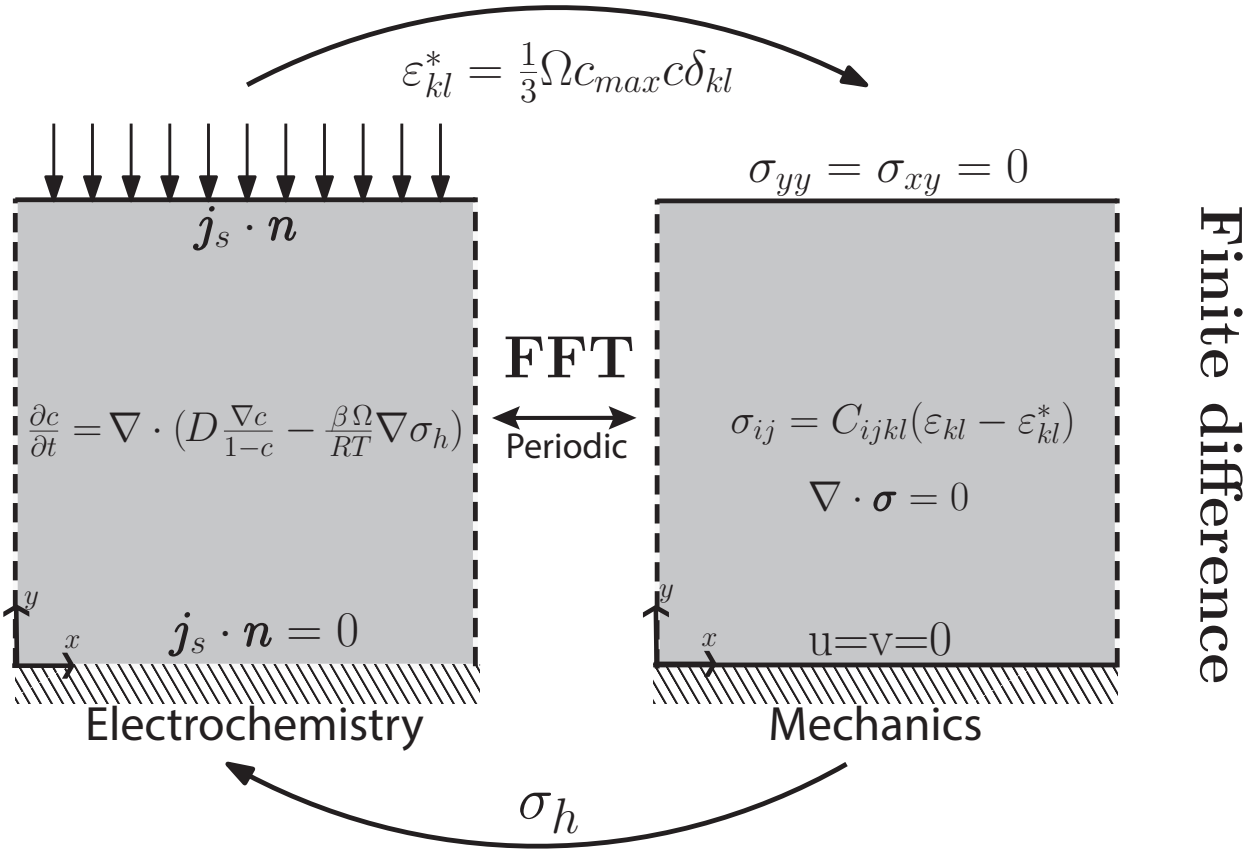

Figure 3.1: Configuration of a unit cell of the periodic domain and the governing equations of electrochemistry and mechanics. The top surface is exposed to electrolyte with traction free mechanics, while the lower surface is fixed to the current collector with zero normal surface flux. Fast Fourier transform is used to numerically solve the governing equations in the lateral direction (x), while finite difference is used in the vertical direction (y).

The differentiation for the first term is shown here.

$$\frac{\partial}{\partial x}(f(c)\frac{\partial c}{\partial x}) = \mathcal{F}^{-1}\left[i\mathbf{k}\mathcal{F}\left(f(c)\mathcal{F}^{-1}(i\mathbf{k}\mathcal{F}(c))\right)\right] \tag{3.2}$$

Also, finite difference methods is used for the spatial differentiation in the y direction.

$$\frac{\partial}{\partial y}(D(c)\frac{\partial c}{\partial y}) = \left[\frac{D_{j+1}+D_j}{2}\frac{c_{j+1}-c_j}{dy} - \frac{D_j+D_{j-1}}{2}\frac{c_j-c_{j-1}}{dy}\right]/dy \tag{3.3}$$

where dy is the mesh size in the y direction. The mechanics is also solved using the Fast Fourier transform and finite difference methods which takes a matrix form for implicit calculations.

It is also worth introducing the unconventional numerical method used in this chapter. One of the investigated cases, which will be shown in the next section, is an electrode with periodic inclusion of modulus of elasticity. For this case, with inhomogeneous stiffness matrix, the mechanical equilibrium equation in its expanded form gives:

$$\mathcal{C}_{ijkl,j}(\frac{\partial u_k}{\partial x_l} - \varepsilon^*_{kl}) + \mathcal{C}_{ijkl}(\frac{\partial {u_k}^2}{\partial x_j \partial x_l} - \varepsilon^*_{kl,j}) = 0, \tag{3.4}$$

where $\mathcal{C}_{ijkl}$, u_k and x_i are the indicial notation form of the stiffness matrix, displacement and spatial variables. This differential equation is solved using FFT in the lateral spatial directions (x). However, taking Fourier transform from this equation brings up complications. For example, taking Fourier transform of the first term in this equation and considering the spatial variation of the stiffness matrix gives:

$$\mathcal{F}\{\mathcal{C}_{ijkl,j}(\frac{\partial u_k}{\partial x_l})\} = \mathcal{F}\{\mathcal{C}_{ijkl,j}\} * \mathcal{F}\{\frac{\partial u_k}{\partial x_l}\} \tag{3.5}$$

where $*$ represents the convolution, which increases the complexity of the numerical imple-

Table 3.1: Material properties of graphite [27, 58, 63] and parameters used in simulations [42].

Modulus of elasticity E	15 GPa
Poisson's ratio ν	0.3
Partial molar volume Ω	4.926×10^{-6} m^3/mol
Maximum concentration c_{max}	2.64×10^4 mol/m^3
Chemical potential in electrolyte μ_e	RT
Gas constant R	8.314 JK^{-1}mol^{-1}
Temperature T	300 K
Coefficient α	0.18
Dimensionless reaction rate $\hat{\mathrm{K}}$	3×10^{-2}
Insertion to extraction ratio $\hat{S}$	2

mentation. A numerical method called circular convolution is used to handle such complication and is presented in Appendix B. For demonstration, the electrode material is taken to be graphite for the following simulations with the properties presented in table 3.1.

3.3 Homogeneous electrode

Here we investigate the diffusion of ions within a homogeneous electrode. The homogeneous material properties within this electrode results in no variation of field variables along the lateral direction (x), while due to the surface flux on the top surface, concentration and stress field evolve with time along the thickness (y). Hence, the electrode model reduces to one-dimension and the variations will be presented along the thickness axis.

The concentration distribution along the depth (y) for two cases of diffusion under coupled and uncoupled with stress models at and intermediate state of charging is shown in Figure 3.2.a. Note that the ions are inserted at $y = 1$ where the surface reaction occurs and their flux is zero at $y = 0$. The concentration starts from the fully discharged state, and as the time goes on, the electrode state of charge increases. An increasing diffusivity at higher

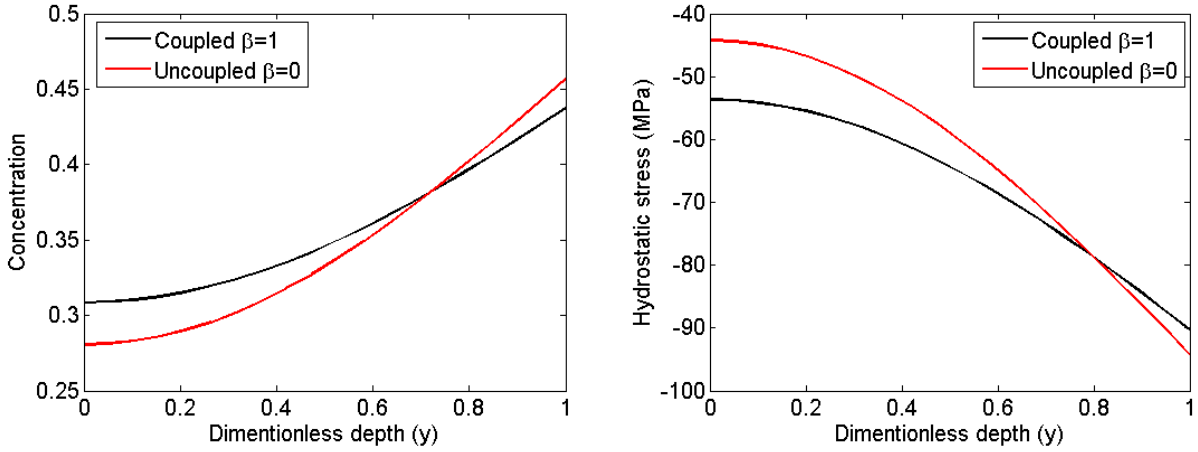

(a) (b)

Figure 3.2: Distribution of a) concentration and b) hydrostatic stress at an intermediate state of charging.

concentrations is noticed with more homogenized concentration profile. Also, the effect of stress on the concentration distribution within an electrode can be realized by comparing the coupled and uncoupled models in Figure 3.2.a. The concentration profile is more homogenized under coupled model illustrating the enhanced diffusivity effect of stress in homogenous materials, which was also reported before [26]. The distribution of hydrostatic stress within the electrode under coupled and uncoupled models are shown in Figure 3.2.b. In this case the gradient of the concentration distribution happens to help the diffusion process in the electrode. The ions are further pushed from the electrolyte side toward the current collector by the compressive stress field. The coupled model predicts more gentle stress distribution due to the more homogenized concentration distribution. Such difference in the developed stress under the coupled and uncoupled models affects the fracture predictions in particles as reported in [26]. The coupled model predicts larger critical sizes due to less sever stress prediction reported in [47, 111] that agrees with experimental results.

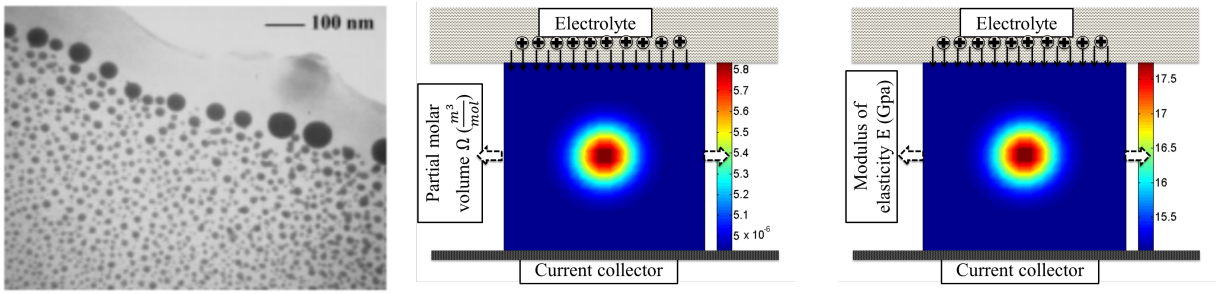

(a) (b) (c)

Figure 3.3: a) Composite electrode of Sn particles embedded in a Carbon matrix [32]. Spatial variation of the introduced periodic inclusions in b) partial molar volume Ω and c) modulus of elasticity E in heterogeneous electrodes. Note that in both cases, the maximum inclusion magnitude is 20% higher than that of the substance.

3.4 Heterogeneous electrodes

Herein we investigate ionic diffusion within two periodic heterogeneous electrodes resembling nanostructured composite electrodes as shown in Figure 3.3.a. First, we study a heterogeneous structure with periodic inclusion in partial molar volume (Ω), while other material properties are constant within the electrode. Next, we investigate a heterogeneous electrode with periodic inclusion in the modulus of elasticity (E), while other material properties are constant within that electrode. The introduced inclusions are assumed to have Gaussian spatial distribution in both heterogeneous electrodes as shown in Figure 3.3. In the electrode configuration, the ions are inserted from the top surface where exposed to electrolyte with traction-free mechanics, and there is no normal ion flux from the bottom surface where mechanically fixed to current collector. The unit cells shown are periodic in lateral direction. The investigated electrodes start from fully discharged state with $c = 0$ and the simulation stops at equilibrium around fully charged state.

Partial molar volume inclusion

The time evolution of concentration and hydrostatic stress distributions within a heterogeneous electrode with periodic inclusions of partial molar volume at different times are shown in Figure 3.4. The ions are gradually inserted from the top surface and stored within the electrode, while at all times, the concentration is the lowest at the center of inclusion. The reason is the higher energy cost of the inclusion, with higher Ω, for ions diffusing within the electrode. The corresponding hydrostatic stress distributions show that the center of the inclusion experiences the highest compressive stress. Such correlation between the concentration distribution and the mechanical compressive stress within the electrode illustrates the coupling between ion concentration and stress. In order to further investigate the effect of inclusion on the ionic diffusion, we study the individual components of the thermodynamic force acting on ions. In our model, there are two thermodynamic forces acting on ions and contribute to the total ion flux (see flux equation). One produces the entropy-induced flux, and the other produces the stress-induced flux. For the purpose of visualization, the normalized total flux and the contributing fluxes at $\hat{t} = 1$ are shown in Figure 3.5. As can be seen, entropy drives the ions from the higher concentration locations toward the center of inclusion with lower concentration, while stress drives the ions out of the center of inclusion with high compressive stress. Superposition of the two competing flux gives the total flux which drives the ions from the insertion interface toward the lower surface while avoiding the inclusion.

3.4.1 Modulus of elasticity inclusion

The evolution of concentration and the developed hydrostatic stress distribution within a heterogeneous electrode with periodic inclusions of modulus of elasticity are shown in Figure 3.6. The area closer to the insertion surface on top, accommodate a higher concentration

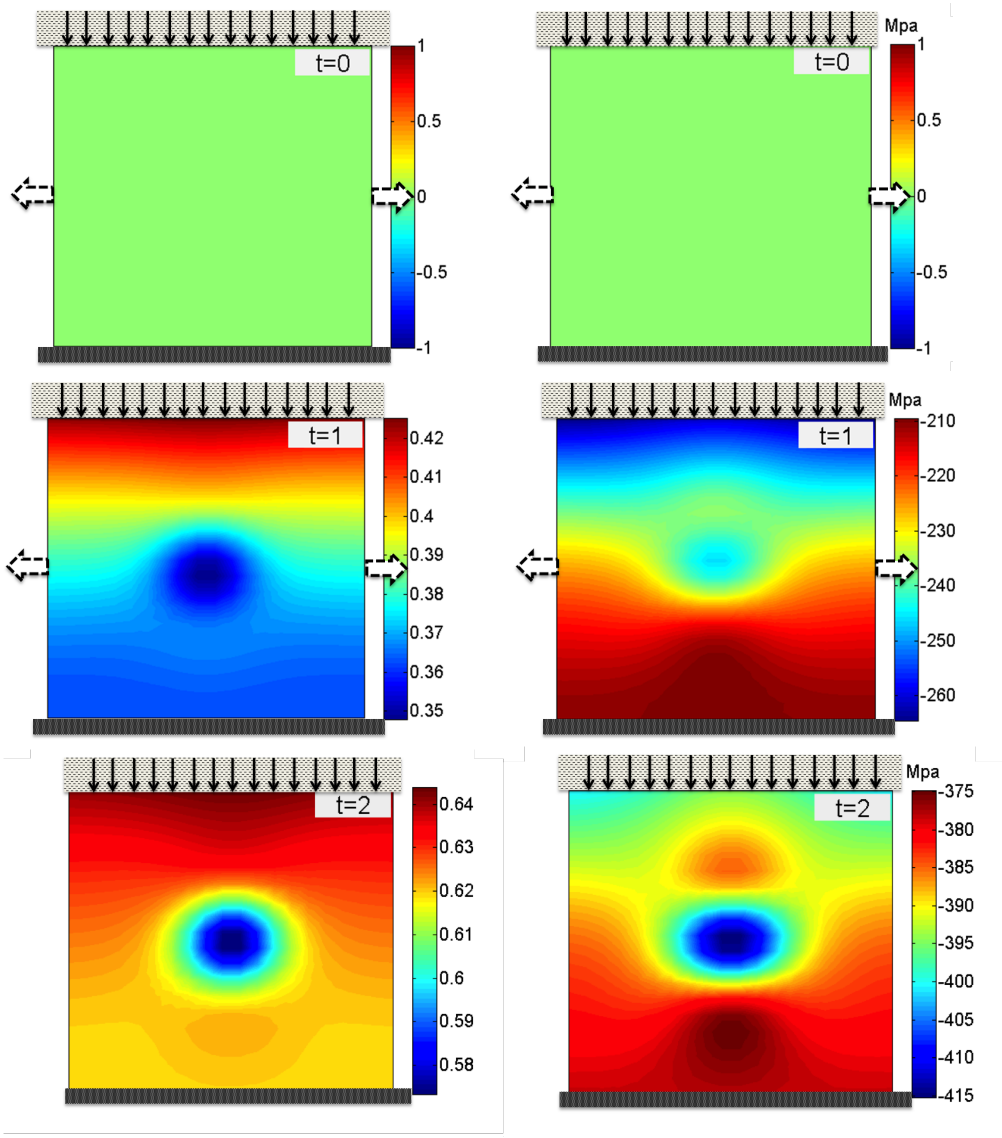

Figure 3.4: Distribution of concentration (left) and hydrostatic stress (right) at different times within a unit cell of electrode with heterogeneous partial molar volume.

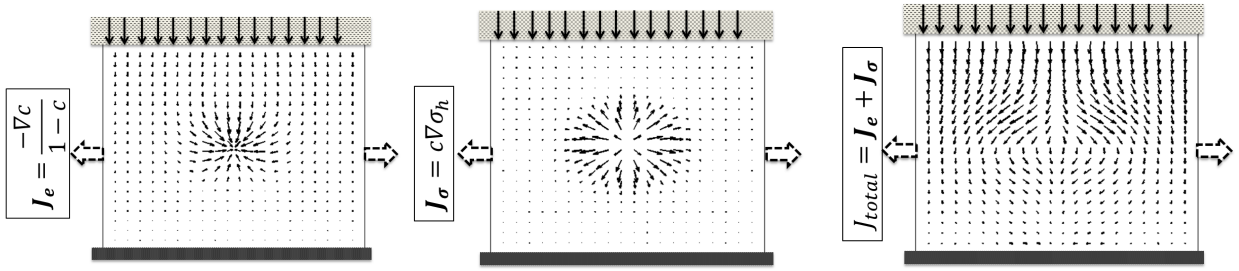

(a) (b) (c)

Figure 3.5: Normalized (a) entropy-induced and (b) stress-induced flux fields contributing to (C) total flux at $\hat{t} = 1$.

at all times. Also, same as the heterogeneous partial molar volume electrode, the concentration of ions over the locations with higher compressive stress is lower. However, in this type of inclusion, the ion depletion over the inclusion is spread out in the lateral direction due to the corresponding developed hydrostatic stress field.

Lastly, the developed von Mises stress at equilibrium is compared for the investigated heterogeneous electrodes in Figure 3.7. Although the concentration distributions are almost similar for both cases, the developed von Mises stresses are different. The electrode with partial molar volume heterogeneity experiences the highest Mises stress at the lateral sides of the inclusion, while the electrode with modulus of elasticity heterogeneity experiences the highest Mises stress at the center of inclusion. This comparison predicts the location of possible failure for such heterogeneous electrodes.

3.5 Conclusion

In this chapter planar electrodes with homogeneous and periodic heterogeneous material properties, resembling nanostructured composite electrodes, were investigated using the developed model. The electrodes were analyzed in a charging period until reaching the fully

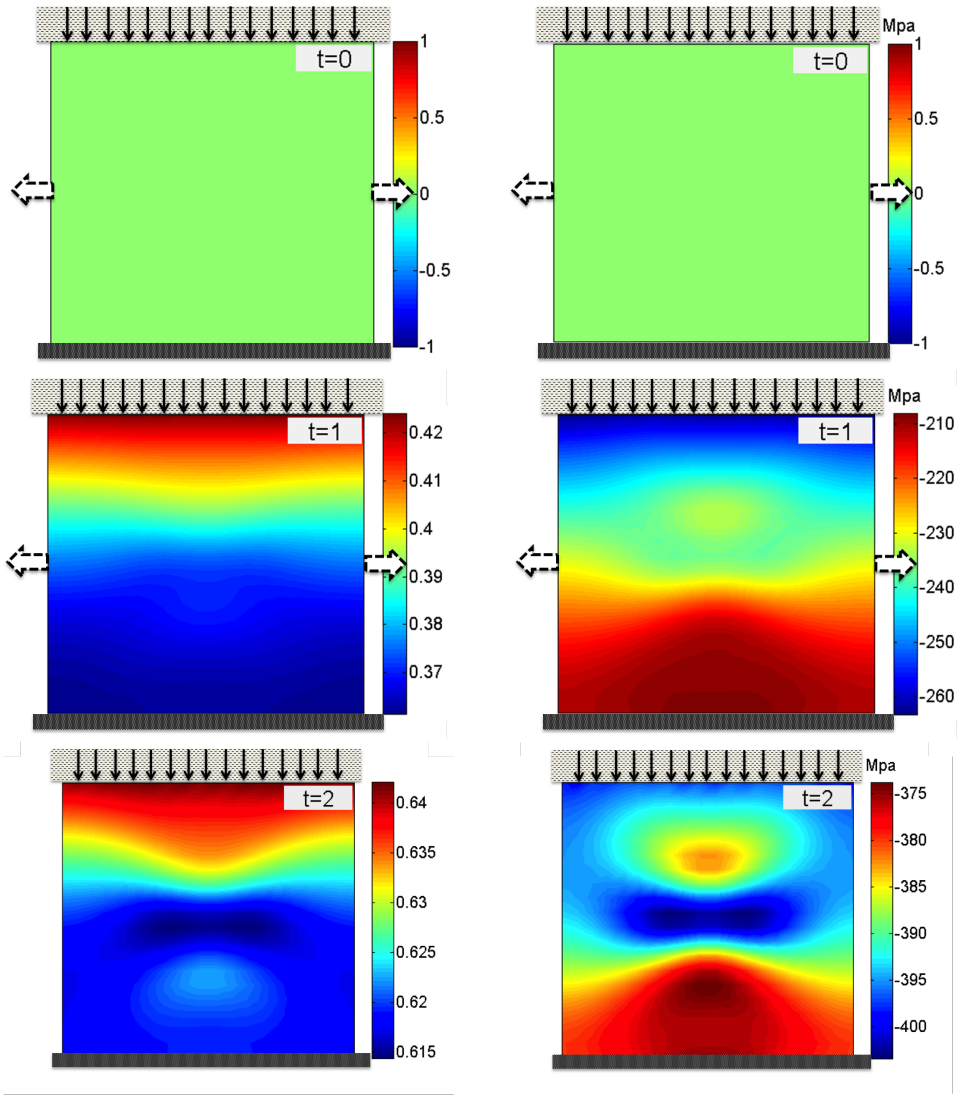

Figure 3.6: Distribution of concentration (left) and hydrostatic stress (right) at different times within a unit cell of electrode with heterogeneous modulus of elasticity.

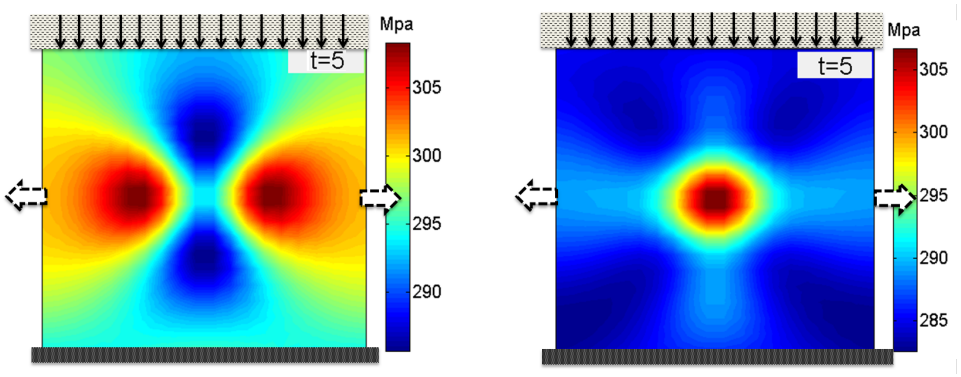

Figure 3.7: Comparison of the generated von Mises stress within the heterogeneous electrodes with inhomogeneity of partial molar volume (left) and modulus of elasticity (right) at different times.

charged state. The concentration distribution comparison within the homogeneous electrode under coupled and uncoupled models revealed that stress helps further diffusion of ions within electrode. The ion flux contribution of the competing thermodynamic forces, entropy and stress, acting on the diffusing atoms were illustrated for the heterogeneous electrode. The evolution of concentration distribution within two heterogeneous electrodes, with periodic partial molar volume and modulus of elasticity inclusions, during the charging process were analyzed. In both electrodes, the ions were diffusing within electrodes while avoiding the inclusions with higher energy cost. Lastly, the evolution of the von Mises stress was compared for the two heterogeneous electrodes.

The current model will be further developed in Chapter 3 to incorporate the effect of boundary conditions and geometry of electrodes on electrochemistry. Moreover, as will be discussed in the next chapters, Electrochemical Strain Microscopy (ESM) technique can provide measurements of the ionic transport in nanoscale. Such combination of experiments and numerical modeling not only brings great insight into the coupling between electrochemistry and mechanics in electrodes, but also can be used to design novel nanostructure composite

electrodes.

Appendix A - Numerical discretization in 2D

In this appendix the numerical methods used for solving the governing differential equations are explained. Because of the periodic condition in the lateral direction, Fast Fourier transform (FFT) is used for discretization and solving the partial differential equations in lateral direction x, while finite difference (FD) method is employed in the y direction. Note that since planar electrodes are investigated, the governing diffusion and mechanics equations are discretized in two-dimension (2D) as following.

Diffusion

The concentration evolution equation, as was expressed in the previous chapter, in a general form is,

$$\frac{\partial c}{\partial t} = \nabla \cdot (f(c)\nabla c) + \nabla \cdot c\nabla\tau \tag{3.6}$$

where concentration dependent diffusivity is defined as $f(c) = \frac{1}{1-c}$ and $\tau \equiv -\frac{\Omega}{RT}\sigma_h$. By expanding the equation in a 2D domain:

$$\frac{\partial c}{\partial t} = \frac{\partial}{\partial x}(f(c)\frac{\partial c}{\partial x}) + \frac{\partial}{\partial y}(f(c)\frac{\partial c}{\partial y}) + \frac{\partial}{\partial x}(c\frac{\partial \tau}{\partial x}) + \frac{\partial}{\partial y}(c\frac{\partial \tau}{\partial y}) \tag{3.7}$$

We conduct the time integration using MATLAB ODE45 and the right-hand-side (RHS) of the equation with spatial differentiation is required to be passed on to. Hence we conduct the spatial differentiation which are explicitly calculated at each time step. The x differentiation is conducted using FFT:

$$\frac{\partial}{\partial x}(f(c)\frac{\partial c}{\partial x}) = \mathcal{F}^{-1}\left[i\mathbf{k}\mathcal{F}\left(f(c)\mathcal{F}^{-1}(i\mathbf{k}\mathcal{F}(c))\right)\right] \tag{3.8}$$

$$\frac{\partial}{\partial x}(c\frac{\partial \tau}{\partial x}) = \mathcal{F}^{-1}\left[i\mathbf{k}\mathcal{F}\left(c\mathcal{F}^{-1}(i\mathbf{k}\mathcal{F}(\tau))\right)\right] \tag{3.9}$$

where i is the imaginary number and $\mathbf{k}$ is the wave vector of FFT. The Fourier transform is also shown with $\mathcal{F}(.)$. The differentiation in y direction using finite difference for each term gives:

$$\frac{\partial}{\partial y}(f(c)\frac{\partial c}{\partial y}) = \left[\frac{f_{j+1}+f_j}{2}\frac{c_{j+1}-c_j}{dy} - \frac{f_j+f_{j-1}}{2}\frac{c_j-c_{j-1}}{dy}\right]/dy \tag{3.10}$$

$$\frac{\partial}{\partial y}(c\frac{\partial \tau}{\partial y}) = \left[\frac{c_{j+1}+c_j}{2}\frac{\tau_{j+1}-\tau_j}{dy} - \frac{c_j+c_{j-1}}{2}\frac{\tau_j-\tau_{j-1}}{dy}\right]/dy \tag{3.11}$$

where dy denotes the mesh size in y direction. The flux boundary condition over the top and bottom surfaces at $y = 1, 0$ are:

$$J_s\big|_{ny} = J_0(1-c_s), J_s\big|_0 = 0 \tag{3.12}$$

which derivation with respect to y can be directly conducted to take the y component of the RHS as:

$$\frac{\partial}{\partial y}(J_y)\big|_{ny} = (3J_0(1-c) - 4J_{ny-1} + J_{ny-2})/(2dy) \tag{3.13}$$

$$\frac{\partial}{\partial y}(J_y)\big|_0 = (+4J_1 - J_2)/(2dy) \tag{3.14}$$

The x component is found based on FFT as explained before.

Mechanics

The mechanics of intercalations is also required to be solved numerically. The mechanical equilibrium equations in solid with eigen strain as was expressed in the previous chapter gives:

$$\sigma_{ij,j} = \mathbb{C}_{ijkl}(\varepsilon_{kl,j} - \varepsilon^*_{kl,j}) = 0 \tag{3.15}$$

where the strain tensor is,

$$\varepsilon_{kl} = \frac{\partial u_k}{\partial x_l}. \tag{3.16}$$

By plugging back in mechanical equilibrium equation:

$$\mathbb{C}_{ijkl} \frac{\partial {u_k}^2}{\partial x_l \partial x_j} = \mathbb{C}_{ijkl} \varepsilon^*_{kl,j} \tag{3.17}$$

Now we expand this expression in the spatial directions of a 2D domain. In expansion one should consider that $\mathbb{C}_{ijkl} = 0$ for all i, j, k, l except 1111, 2222, 1212 , 2121 , 1221 and 2112 combinations. Note that the only not repeated index in this equation is i. By setting the following elasticity matrix with the plain strain condition and expanding the described equations one can get the following set of equations for $i = 1, 2$.

$$\mathbb{C} = \begin{bmatrix} C1 & C2 & 0 \\ C2 & C1 & 0 \\ 0 & 0 & C3 \end{bmatrix}$$

$$C_1 \frac{\partial^2 u}{\partial x^2} + C_2 \frac{\partial^2 v}{\partial y \partial x} + C_3 \frac{\partial^2 u}{\partial y^2} + C_3 \frac{\partial^2 v}{\partial x \partial y} = C_1 \frac{\partial \varepsilon^*_{11}}{\partial x} + C_2 \frac{\partial \varepsilon^*_{22}}{\partial x} + C_3 \frac{\partial \varepsilon^*_{12}}{\partial y} + C_3 \frac{\partial \varepsilon^*_{21}}{\partial y} \tag{3.18}$$

$$C_1 \frac{\partial^2 v}{\partial y^2} + C_2 \frac{\partial^2 u}{\partial x \partial y} + C_3 \frac{\partial^2 u}{\partial y \partial x} + C_3 \frac{\partial^2 v}{\partial x^2} = C_1 \frac{\partial \varepsilon^*_{22}}{\partial y} + C_3 \frac{\partial \varepsilon^*_{21}}{\partial x} + C_3 \frac{\partial \varepsilon^*_{12}}{\partial x} + C_2 \frac{\partial \varepsilon^*_{11}}{\partial y} \tag{3.19}$$

Taking Fourier transform in x direction gives:

$$-C_1 \mathrm{k}^2 \bar{u} + C_2 \mathrm{ik} \frac{\partial \bar{v}}{\partial y} + C_3 \frac{\partial \bar{u}}{\partial y^2} + C_3 \mathrm{ik} \frac{\partial^2 \bar{v}}{\partial y} = C_1 \mathrm{ik} \bar{\varepsilon^*_{11}} + C_2 \mathrm{ik} \bar{\varepsilon^*_{22}} + C_3 \frac{\partial \bar{\varepsilon^*_{12}}}{\partial y} + C_3 \frac{\partial \bar{\varepsilon^*_{21}}}{\partial y} \tag{3.20}$$

$$C_1 \frac{\partial^2 \bar{v}}{\partial y^2} + C_2 \mathrm{ik} \frac{\partial \bar{u}}{\partial y} + C_3 \mathrm{ik} \frac{\partial \bar{u}}{\partial y} - \mathrm{k}^2 C_3 \bar{v} = C_1 \frac{\partial \bar{\varepsilon^*_{22}}}{\partial y} + C_3 \mathrm{ik} \bar{\varepsilon^*_{21}} + C_3 \mathrm{ik} \bar{\varepsilon^*_{12}} + C_2 \frac{\partial \bar{\varepsilon^*_{11}}}{\partial y} \tag{3.21}$$

Using finite difference method in y direction and putting it into the matrix form for a position in x direction (say index i) gives:

$$\Big[-C_1 \mathrm{k}^2(i)\mathbf{I_1} + (C_2+C_3)\mathrm{ik}(i)\mathbf{B_2}\frac{1}{2\Delta y} + C_3\mathbf{T_1}\frac{1}{\Delta y^2} \tag{3.22}$$

$$+ C_1\mathbf{T_4}\frac{1}{\Delta y^2} + (C_2+C_3)\mathrm{ik}(i)\mathbf{B_3}\frac{1}{2\Delta y} - C_3\mathrm{k}^2\mathbf{I_4} + \bar{\mathbf{R}}\Big]\bar{\mathbf{X}} = \bar{\mathbf{f}} + \bar{\delta} \tag{3.23}$$

where the $\mathbf{T}$ and $\mathbf{B}$ matrices are the second and first derivation matrices with $2(n-1)\times 2(n-1)$ dimensions and the subscript shows the quarter which $(n-1)\times(n-1)$ matrices are placed. Note that n is the size of the nodes in each direction. Also, $\bar{\mathbf{f}}$ is a $2(n-1)\times 1$ vector corresponding to the RHS of the Equations 3.20,3.20. Also note that that the unknown matrix is formed as:

$$\mathbf{X} = \begin{bmatrix} \bar{u_2} \\ \vdots \\ \bar{u_n} \\ \bar{v_2} \\ \vdots \\ \bar{v_n} \end{bmatrix}_{2(n-1)\times 1} \tag{3.24}$$

Assembling of the introduced matrices are straightforward so we just mention the $\bar{\delta}$ vector here, which is derived from the boundary conditions. As boundary conditions we have the traction free condition at one side in y direction that needs to be translated as Neumann boundary condition and displacement condition at one side that needs to be reformed as Dirichlet boundary condition. The traction boundary condition at $y = L$ on $\bar{\sigma}_{yy}$ and $\bar{\sigma}_{xy}$ gives:

$$\bar{\sigma}_{xy} = 2C_3(\frac{\partial \bar{u}}{\partial y} - \bar{\varepsilon}^*_{xy}) \rightarrow \left.\frac{\partial \bar{u}}{\partial y}\right|_n = \frac{\bar{\sigma}_{xy}}{2C_3} + \bar{\varepsilon}^*_{xy} \equiv \alpha \tag{3.25}$$

$$\bar{\sigma}_{yy} = C_1(\frac{\partial \bar{v}}{\partial y} - \bar{\varepsilon^*_{yy}}) + C_2(ik\bar{u} - \bar{\varepsilon^*_{xx}}) \rightarrow \left.\frac{\partial \bar{v}}{\partial y}\right|_n = \frac{\bar{\sigma}_{yy}}{C_1} + \bar{\varepsilon^*_{yy}} - \frac{C_2}{C_1}(ik\bar{u} - \bar{\varepsilon^*}_{xx}) \tag{3.26}$$

we define:

$$\beta \equiv \frac{\bar{\sigma}_{yy}}{C_1} + \bar{\varepsilon^*_{yy}} + \frac{C_2}{C_1}\bar{\varepsilon^*}_{xx} \tag{3.27}$$

therefore,

$$\bar{v}_{n+1} = 2\frac{\partial \bar{v}}{\partial y}dy + \bar{v}_{n-1}$$

$$\left.\frac{\partial^2 \bar{v}}{\partial y^2}\right|_n = \frac{2\bar{v}_{n-1} - 2\bar{v}_n}{dy^2} + 2(\beta - \frac{C_2}{C_1}ik\bar{u})/dy$$

Eventually by implementing the above boundary conditions in the matrix form:

$$\bar{\delta} = \begin{bmatrix} (C_2+C_3)ik\bar{v_1}(i)/(2dy) - C_3\bar{u_1}/(dy^2) \\ 0 \\ \vdots \\ 0 \\ -(C_2+C_3)ik\beta - 2C_3\alpha/dy \\ (C_2+C_3)ik\bar{u}_1/(2dy) - C_1\bar{v}_1/(dy^2) \\ 0 \\ \vdots \\ 0 \\ -(C_2+C_3)ik\alpha - C_1 2\beta/dy \end{bmatrix}_{2(n-1)\times 1} \tag{3.28}$$

and the differentiation at the boundary $y = L$ needs residual R matrix as:

$$\bar{\mathbf{R}}(n-1, n-1) = k^2 C_2(C_2 + C3)/C_1 \tag{3.29}$$

$$\bar{\mathbf{R}}(2(n-1), n-1) = -2ikC_2 \tag{3.30}$$

Appendix B- Numerical discretization of mechanics using circular convolution:

The mechanical equilibrium equation with spatial variable stiffness matrix leads to:

$$\mathcal{C}_{ijkl,j}(\varepsilon_{kl} - \varepsilon^*_{kl}) + \mathcal{C}_{ijkl}(\varepsilon_{kl,j} - \varepsilon^*_{kl,j}) = 0 \tag{3.31}$$

we know that:

$$\varepsilon_{kl} = \frac{\partial u_k}{\partial x_l} \tag{3.32}$$

by substitution:

$$\mathcal{C}_{ijkl,j}(\frac{\partial u_k}{\partial x_l} - \varepsilon^*_{kl}) + \mathcal{C}_{ijkl}(\frac{\partial {u_k}^2}{\partial x_j \partial x_l} - \varepsilon^*_{kl,j}) = 0 \tag{3.33}$$

Next step is to expand the terms by having $\mathcal{C}_{ijkl} = 0$ for all i, j, k, l except 1111, 2222, 1212 , 2121 , 1221 and 2112 combinations. Note that the free index in this equation is i.

$$\begin{aligned}
&\mathcal{C}_{1111}(\frac{\partial u_1}{\partial x_1 \partial x_1} - \frac{\partial \varepsilon^*_{11}}{\partial x_1}) + \mathcal{C}_{1212}(\frac{\partial u_1}{\partial x_2 \partial x_2} - \frac{\partial \varepsilon^*_{12}}{\partial x_2}) + \mathcal{C}_{1221}(\frac{\partial u_2}{\partial x_2 \partial x_1} - \frac{\partial \varepsilon^*_{21}}{\partial x_2}) \\
&+ \mathcal{C}_{1122}(\frac{\partial u_2}{\partial x_1 \partial x_2} - \frac{\partial \varepsilon^*_{22}}{\partial x_1}) + \mathcal{C}_{1111,1}(\frac{\partial u_1}{\partial x_1} - \varepsilon^*_{11}) + \mathcal{C}_{1212,2}(\frac{\partial u_1}{\partial x_2} - \varepsilon^*_{12}) \\
&+ \mathcal{C}_{1221,2}(\frac{\partial u_2}{\partial x_1} - \varepsilon^*_{21}) + \mathcal{C}_{1122,1}(\frac{\partial u_2}{\partial x_2} - \varepsilon^*_{22}) = 0
\end{aligned} \tag{3.34}$$

$$\begin{aligned}
&\mathcal{C}_{2222}(\frac{\partial u_2}{\partial x_2 \partial x_2} - \frac{\partial \varepsilon^*_{22}}{\partial x_2}) + \mathcal{C}_{2121}(\frac{\partial u_2}{\partial x_1 \partial x_1} - \frac{\partial \varepsilon^*_{21}}{\partial x_1}) + \mathcal{C}_{2112}(\frac{\partial u_1}{\partial x_1 \partial x_2} - \frac{\partial \varepsilon^*_{12}}{\partial x_1}) \\
&+ \mathcal{C}_{2211}(\frac{\partial u_1}{\partial x_2 \partial x_1} - \frac{\partial \varepsilon^*_{11}}{\partial x_2}) + \mathcal{C}_{2222,2}(\frac{\partial u_2}{\partial x_1} - \varepsilon^*_{11}) + \mathcal{C}_{2121,1}(\frac{\partial u_2}{\partial x_1} - \varepsilon^*_{21}) \\
&+ \mathcal{C}_{2112,1}(\frac{\partial u_1}{\partial x_2} - \varepsilon^*_{12}) + \mathcal{C}_{2211,2}(\frac{\partial u_1}{\partial x_1} - \varepsilon^*_{11}) = 0
\end{aligned} \tag{3.35}$$

For simplicity the following notations are used as the elasticity terms.

$$\begin{cases} \mathcal{C}_{1111} = \mathcal{C}_{2222} = \mathcal{C}_1 \\ \mathcal{C}_{1122} = \mathcal{C}_{2211} = \mathcal{C}_2 \\ \mathcal{C}_{1212} = \mathcal{C}_{1221} = \mathcal{C}_{2121} = \mathcal{C}_{2112} = \mathcal{C}_3 \end{cases}$$

Taking Fourier transform in x direction and knowing that $\mathcal{C}_1, \mathcal{C}_2$ and $\mathcal{C}_3$ are functions of x requires using convolution. Applying Fourier transform and rearranging the equations gives:

$$\begin{aligned} &\overline{\mathcal{C}_1} * (-k_x k_x \overline{u}) + \overline{\mathcal{C}_3} * (\frac{\partial^2 \overline{u}}{\partial y^2}) + \overline{\mathcal{C}_3} * (\frac{\partial}{\partial y} \mathbf{i} k_x \overline{v}) + \overline{\mathcal{C}_3} * (\mathbf{i} k_x \frac{\partial \overline{v}}{\partial y}) + (\mathbf{i} k_x \overline{\mathcal{C}_1}) * (\mathbf{i} k_x \overline{u}) \\ &+ (\overline{\frac{\partial \mathcal{C}_3}{\partial y}}) * (\frac{\partial \overline{u}}{\partial y}) + (\overline{\frac{\partial \mathcal{C}_3}{\partial y}}) * (\mathbf{i} k_x \overline{v}) + (\mathbf{i} k_x \overline{\mathcal{C}_2}) * (\frac{\partial \overline{v}}{\partial y}) \\ &= \overline{\mathcal{C}_1} * (\mathbf{i} k_x \overline{\varepsilon_1^*}) + 2\overline{\mathcal{C}_3} * (\frac{\partial \overline{\varepsilon_3^*}}{\partial y}) + \overline{\mathcal{C}_2} * (\mathbf{i} k_x \overline{\varepsilon_2^*}) + (\mathbf{i} k_x \overline{\mathcal{C}_1}) * (\overline{\varepsilon_1^*}) + 2(\overline{\frac{\partial \mathcal{C}_3}{\partial y}}) * (\overline{\varepsilon_3^*}) \\ &+ (\mathbf{i} k_x \overline{\mathcal{C}_2}) * (\overline{\varepsilon_2^*}) \end{aligned} \tag{3.36}$$

$$\begin{aligned} &\overline{\mathcal{C}_1} * (\frac{\partial^2 \overline{v}}{\partial y^2}) + \overline{\mathcal{C}_3} * (-k_x k_x \overline{v}) + \overline{\mathcal{C}_3} * (\mathbf{i} k_x \frac{\partial \overline{u}}{\partial y}) + \overline{\mathcal{C}_2} * (\frac{\partial}{\partial y} \mathbf{i} k_x \overline{u}) + (\overline{\frac{\partial \mathcal{C}_1}{\partial y}}) * (\frac{\partial \overline{v}}{\partial y}) \\ &+ (\mathbf{i} k_x \overline{\mathcal{C}_3}) * (\mathbf{i} k_x \overline{v}) + (\mathbf{i} k_x \overline{\mathcal{C}_3}) * (\frac{\partial \overline{u}}{\partial y}) + (\overline{\frac{\partial \mathcal{C}_2}{\partial y}}) * (\mathbf{i} k_x \overline{u}) \\ &= \overline{\mathcal{C}_1} * (\frac{\partial \overline{\varepsilon_2}}{\partial y}) + 2\overline{\mathcal{C}_3} * (\mathbf{i} k_x \overline{\varepsilon_3^*}) + \overline{\mathcal{C}_2} * (\frac{\partial \overline{\varepsilon_1^*}}{\partial y}) + (\overline{\frac{\partial \mathcal{C}_1}{\partial y}}) * (\overline{\varepsilon_2^*}) + 2(\mathbf{i} k_x \overline{\mathcal{C}_3}) * (\overline{\varepsilon_3^*}) + \\ &+ (\frac{\partial \overline{\mathcal{C}_2}}{\partial y}) * (\overline{\varepsilon_1^*}) \end{aligned} \tag{3.37}$$

For the boundary conditions we have:

$$\begin{cases} u, v & @y = 0 \\ \sigma_{22}, \sigma_{12} & @y = L \end{cases}$$

For the $y = L$ B.C.s:

$$\overline{\sigma_{22}}^n = \overline{\mathbf{C}_1}^n * (\frac{\partial \overline{v}}{\partial y}^n - \overline{\varepsilon_2^*}^n) + \overline{\mathbf{C}_2}^n * (\mathbf{i}k_x\overline{u}^n - \overline{\varepsilon_1^*}^n) \tag{3.38}$$

$$\frac{\partial \overline{v}}{\partial y}^n = \overline{\mathbf{C}_1}^{-1} * \overline{\sigma_{22}}^n + \overline{\varepsilon_2^*}^n + \nu(\overline{\varepsilon_1^*}^n - \mathbf{i}k_x\overline{u}^n) \tag{3.39}$$

for simplicity we introduce:

$$\frac{\partial \overline{v}}{\partial y}^n = \beta - \nu\mathbf{i}k_x\overline{u}^n \tag{3.40}$$

$$\frac{\partial^2 \overline{v}}{\partial y^2}^n = \frac{2\overline{v}^{n-1} - 2\overline{v}^n}{\Delta y^2} + 2(\beta - \nu\mathbf{i}k_x\overline{u}^n)/\Delta y \tag{3.41}$$

$$\overline{\sigma_{12}}^n = \overline{\mathbf{C}_3}^n * (\frac{\partial \overline{u}}{\partial y}^n - \overline{\varepsilon_3^*}^n) + \overline{\mathbf{C}_3}^n * (\mathbf{i}k_x\overline{v}^n - \overline{\varepsilon_3^*}^n) \tag{3.42}$$

$$\frac{\partial \overline{u}}{\partial y}^n = \overline{\mathbf{C}_3}^{-1} * \overline{\sigma_{12}}^n + 2\overline{\varepsilon_3^*}^n - \mathbf{i}k_x\overline{v}^n \tag{3.43}$$

and,

$$\frac{\partial \overline{u}}{\partial y}^n = \alpha - \mathbf{i}k_x\overline{v}^n \tag{3.44}$$

$$\frac{\partial^2 \overline{u}}{\partial y^2}^n = \frac{2\overline{u}^{n-1} - 2\overline{u}^n}{\Delta y^2} + 2(\alpha - \mathbf{i}k_x\overline{v}^n)/\Delta y \tag{3.45}$$

and for the B.C.s at $y = 0$:

$$\frac{\partial \bar{u}}{\partial y}^2 = \frac{\bar{u_3}}{2\Delta y} - \frac{\bar{u_1}}{2\Delta y} \tag{3.46}$$

$$\frac{\partial \bar{u^2}}{\partial y^2}^2 = \frac{\bar{u_3} - 2\bar{u_2}}{\Delta y^2} - \frac{\bar{u_1}}{\Delta y^2} \tag{3.47}$$

$$\frac{\partial \bar{v}}{\partial y}^2 = \frac{\bar{v_3}}{2\Delta y} - \frac{\bar{v_1}}{2\Delta y} \tag{3.48}$$

$$\frac{\partial \bar{v^2}}{\partial y^2}^2 = \frac{\bar{v_3} - 2\bar{v_2}}{\Delta y^2} - \frac{\bar{v_1}}{\Delta y^2} \tag{3.49}$$

Using finite difference method in y direction and circular convolution method we have:

$$\Big[- \mathbb{C}_1\mathbb{K}_x\mathbb{K}_x\mathbb{I}_{11} + (\mathbb{C}_2 + \mathbb{C}_3)\mathbf{i}\mathbb{K}_x\mathbb{B}_{12}/2\Delta y + \mathbb{C}_3\mathbb{T}_{11}\frac{1}{\Delta y^2} \tag{3.50}$$

$$- (\mathcal{K}_x.\mathbb{C}_1)\mathbb{K}_x\mathbb{I}_{11} + \frac{\partial \mathbb{C}_3}{\partial y}\mathbb{B}_{11}/(2\Delta y) + \frac{\partial \mathbb{C}_3}{\partial y}\mathbf{i}\mathbb{K}_x\mathbb{I}_{12} + (\mathbf{i}\mathcal{K}_x.\mathbb{C}_2)\mathbb{B}_{12} \tag{3.51}$$

$$+ \mathbb{C}_1\mathbb{T}_{22}/\Delta y^2 + (\mathbb{C}_2 + \mathbb{C}_3)\mathbf{i}\mathbb{K}_x\mathbb{B}_{21}/2\Delta y - \mathbb{C}_3\mathbb{K}_x^2\mathbb{I}_{22} + \frac{\partial \mathbb{C}_1}{\partial y}\mathbb{B}_{22}/\Delta y \tag{3.52}$$

$$- (\mathcal{K}_x.\mathbb{C}_3)\mathbb{K}_x\mathbb{I}_{22} + (\mathbf{i}\mathcal{K}_x.\mathbb{C}_3)\mathbb{B}_{21}/\Delta y + \frac{\partial \mathbb{C}_2}{\partial y}\mathbf{i}\mathbb{K}_x\mathbb{I}_{21} + \mathbb{R}\Big]\bar{\mathbf{X}} \tag{3.53}$$

$$= \mathbb{R}\mathbb{H}\mathbb{S} + \mathbb{D} \tag{3.54}$$

where:

$$\overline{\mathbf{X}} = \begin{bmatrix} \overline{u}_{1,2} \\ \vdots \\ \overline{u}_{1,ny-1} \\ \overline{v}_{1,2} \\ \vdots \\ \overline{v}_{1,ny-1} \\ \vdots \\ \overline{u}_{nx,2} \\ \vdots \\ \overline{u}_{nx,ny-1} \\ \overline{v}_{nx,2} \\ \vdots \\ \overline{v}_{nx,ny-1} \end{bmatrix}_{2nx(ny-1)\times 1} \tag{3.55}$$

and $\mathbb{I}_{mn}, \mathbb{B}_{mn}, \mathbb{T}_{mn}$ are $2nx(ny-1) \times 2nx(ny-1)$ matrices which subscript shows the quarter which $\mathbf{T}$, $\mathbf{B}$ and $\mathbf{I}$ matrices are placed to make the $2(ny-1) \times (ny-1)$ matrices. These matrices are then assembled diagonally to make the full $2nx(ny-1) \times 2nx(ny-1)$ matrices.

$\mathbb{RHS}$ is a $2nx(ny-1)$ vector corresponding to the R.H.S s of the equations 9 and 10 which is made by assembling $\mathbb{RHS}_1$ and $\mathbb{RHS}_2$. For each row of the $\mathbb{RHS}$:

$$\mathbb{RHS}_1^j = \mathbf{C}_1^j(\mathbf{i}\mathbf{k}_x.\overline{\varepsilon_1^*}^j) + 2\mathbf{C}_3^j\overline{\frac{\partial \varepsilon_3^*}{\partial y}}^j + \mathbf{C}_2^j(\mathbf{i}\mathbf{k}_x.\overline{\varepsilon_2^*}^j) + (\mathbf{i}\kappa.\mathbf{C}_1^j)\overline{\varepsilon_1^*}^j + 2\frac{\partial \mathbb{C}_3}{\partial y}^j\overline{\varepsilon_3^*}^j \tag{3.56}$$

$$+ (\mathbf{i}\kappa.\mathbf{C}_2^j)\overline{\varepsilon_2^*}^j \tag{3.57}$$

$$\mathbb{RHS}_2^j = \mathbf{C}_1^j \overline{\frac{\partial \varepsilon_2^*}{\partial y}}^j + 2\mathbf{C}_3^j(\mathbf{i}\mathbf{k}_x.^*\overline{\varepsilon_3^*}^j) + \mathbf{C}_2^j \overline{\frac{\partial \varepsilon_1}{\partial y}}^j + \frac{\partial \mathbb{C}_1}{\partial y}^j \overline{\varepsilon_2^*}^j + 2(\mathbf{i}\kappa.^*\mathbf{C}_3^j)\overline{\varepsilon_3^*}^j \tag{3.58}$$

$$+ \frac{\partial \mathbb{C}_2}{\partial y}^j \overline{\varepsilon_1^*}^j \tag{3.59}$$

$\mathbb{D}$ is a vector corresponding to the boundary conditions and is assembled from $\mathbf{D}_1$, $\mathbf{D}_2$, $\mathbf{D}_3$ and $\mathbf{D}_4$.

$$\mathbf{D}^1 = (\mathbf{i}\kappa.^*\mathbf{C}_2 + \mathbf{C}_2 + \mathbf{C}_3)\mathbf{i}\mathbf{k}_x\overline{v}_0/(2 * \Delta y) + (\mathbf{C}_3 + \mathbf{C}_1)\overline{u}_0/(\Delta y^2) \tag{3.60}$$

$$+ (\mathbf{d}\mathbf{C}_3)\overline{u}_0/(2\Delta y) + (\mathbf{i}\kappa.^*\mathbf{C}_2)\overline{v}_0/(2\Delta y) \tag{3.61}$$

$$\mathbf{D}^{ny-1} = -\mathbf{C}_3^n 2\alpha/\Delta y - \mathbf{C}_3^n\mathbf{i}\mathbf{k}_x.^*\beta - \mathbf{C}_2^n\mathbf{i}\mathbf{k}_x\beta - d\mathbf{C}_3^n\alpha - (\mathbf{i}\kappa.^*\mathbf{C}_2^n)\beta \tag{3.62}$$

$$\mathbf{D}^{ny} = -\mathbf{C}_1 2\beta/\Delta y - \mathbf{C}_3\mathbf{i}\mathbf{k}_x.^*\alpha - \mathbf{C}_2\mathbf{i}\mathbf{k}_x\alpha - d\mathbf{C}_1\beta - (\mathbf{i}\kappa.^*\mathbf{C}_3)\alpha \tag{3.63}$$

$$\mathbf{D}^{2(ny-1)} = -\mathbf{C}_1^n 2\beta/\Delta y - \mathbf{C}_3^n)\mathbf{k}_x.^*\alpha - \mathbf{C}_2^n\mathbf{i}\mathbf{k}_x\alpha - d\mathbf{C}_1^n\beta - (\mathbf{i}\kappa.^*\mathbf{C}_3^n)\alpha \tag{3.64}$$

$\mathbb{R}$ is the matrix resulted from the residual of the boundary conditions (u, v dependent parts). It is assembled from the $\mathbf{dV_{Res}}1$, $\mathbf{dV_{Res}}2$, $\mathbf{dU_{Res}}1$ and $\mathbf{dU_{Res}}2$ matrices with $nx \times nx$ dimension.

$$\mathbf{dV_{Res}}1(\overline{\mathbf{u}}^\mathbf{n}) = \left[(\mathbf{C}_2^n + \mathbf{C}_3^n)\mathbf{i}\nu\mathbf{K}_x\mathbf{K}_x + (\mathbf{i}\kappa_x.\mathbf{C}_2^n)\nu\mathbf{K}_x\right] \tag{3.65}$$

$$\mathbf{dV_{Res}}2(\overline{\mathbf{u}}^{\mathbf{n}}) = \big[-2\nu\mathbf{i}\mathbf{C}_1^n\mathbf{K}_x/\Delta y - \frac{\partial \mathbf{C_1}^n}{\partial \mathbf{y}}\,\nu\mathbf{i}\mathbf{K}_x\big] \tag{3.66}$$

$$\mathbf{dU_{Res}}1(\overline{\mathbf{v}}^{\mathbf{n}}) = \big[-2\mathbf{i}\mathbf{C}_3^n\mathbf{K}_x/\Delta y - \frac{\partial \mathbf{C_3}^n}{\partial \mathbf{y}}\,\mathbf{i}\mathbf{K}_x\big] \tag{3.67}$$

$$\mathbf{dU_{Res}}2(\overline{\mathbf{v}}^{\mathbf{n}}) = \big[(\mathbf{C}_2^n + \mathbf{C}_3^n)\mathbf{K}_x\mathbf{K}_x + (\kappa.\mathbf{C}_3^n)\mathbf{K}_x\big] \tag{3.68}$$

$\mathbf{C}_1^j$, $\mathbf{C}_2^j$ and $\mathbf{C}_3^j$ are the circular convolution matrices of the Fourier transform of $\mathcal{C}_1^j$,$\mathcal{C}_2^j$ and $\mathcal{C}_3^j$ at the jth row. $\mathbb{C}_1$, $\mathbb{C}_2$ and $\mathbb{C}_3$ are the corresponding $2nx(ny-1) \times 2nx(ny-1)$ matrices assembled from the $\mathbf{C}_1$, $\mathbf{C}_2$ and $\mathbf{C}_3$ $nx \times nx$ matrices.

$$\mathbf{C}^j = \begin{bmatrix} \overline{C}_1^j & \overline{C}_{nx}^j & \cdots & \overline{C}_3^j & \overline{C}_2^j \\ \overline{C}_2^j & \overline{C}_1^j & \cdots & \overline{C}_4^j & \overline{C}_3^j \\ \vdots & \vdots & \cdots & \vdots & \vdots \\ \overline{C}_{nx}^j & \overline{C}_{nx-1}^j & \cdots & \overline{C}_2^j & \overline{C}_1^j \end{bmatrix}_{nx\times nx} \tag{3.69}$$

$\mathbb{K}_x$ is the assembled diagonal wave matrix. And $\mathcal{K}$ is the made by assembling circular matrices of wave vector shown as κ. Note that this matrix is dot product with the $\mathbb{C}$ matrices.

$$\mathbb{K} = \begin{bmatrix} k_x^1 & & & & \\ & \ddots & & & \\ & & k_x^1 & & 0 \\ & & & \ddots & \\ & 0 & & & k_x^{nx} \\ & & & & & \ddots \\ & & & & & & k_x^{nx} \end{bmatrix}_{2nx(ny-1)\times 2nx(ny-1)} \tag{3.70}$$

$$\kappa = \begin{bmatrix} k_x^1 & k_x^{nx} & \cdots & k_x^3 & k_x^2 \\ k_x^2 & k_x^1 & \cdots & k_x^4 & k_x^3 \\ \vdots & \vdots & \cdots & \vdots & \vdots \\ k_x^{nx} & k_x^{nx-1} & \cdots & k_x^2 & k_x^1 \end{bmatrix}_{nx \times nx} \tag{3.71}$$

Chapter 4

NUMERICAL METHODS: FINITE ELEMENT IN COMSOL MULTIPHYSICS

4.1 Introduction

The capacity of electrode is directly related to the amount of ions that can be reversibly inserted and extracted into and out of electrode, and there are numerous continuum based studies addressing ionic transport inside bulk electrode, built on the thermodynamics of intercalation [75]. Due to the strong coupling between electrochemistry and mechanics, recent studies on continuum modeling of ionic diffusion account for the effects of stress as well [117, 116, 27, 22]. The thermodynamics of solute atoms in equilibrium inside an elastic host can be traced back to the works of Larch and Cahn [61] and Li et. al [64], and recent studies on the stress-induced diffusion in Li-ion battery electrodes have been based on this general framework. Some researchers have developed more general models of the stress-induced diffusion [29], and Haftbaradaran et. al. have validated diffusion induced by the hydrostatic stress using atomistic simulations [42].

The electrochemistry at the electrolyte-electrode interface is also critical, which is commonly governed by Butler-Volmer relation or its linearized form [76, 38]. In this kinetics, the activation energy depends on the electrostatic potential difference across the interface, and there is a continuous flux of ions into the electrode until it is filled to its maximum capacity. On the other hand, as was explained in the modeling framework Bazant et. al. treated reaction rates as governed by Arrhenius kinetics, with the activation energy depending on the chemical potential difference across the interface [95]. Such kinetic model enabled them

to predict intercalation phase separation waves propagating through the electrode.

These governing equations of ion intercalation, mechanics and surface kinetics are implemented and solved in COMSOL Multiphysics. We study diffusion of Li-ion in electrode, and its coupling with stress, with particular attention paid on the geometry of electrode and the corresponding boundary conditions. Lastly, the simulation platform is used to study the geometry design parameters of electrode topography on the capacity and charging time of the electrode.

4.2 Comsol implementation

Finite element method is used to numerically solve the coupled partial differential equations of diffusion and mechanics implemented in COMSOL Multiphysics platform. The evolution equation of concentration is solved via the General PDE mode as,

$$\frac{\partial c}{\partial \hat{t}} + \nabla \cdot \mathbf{\Gamma} = 0 \tag{4.1}$$

where we introduce

$$\mathbf{\Gamma} \equiv e^{\beta\alpha\sigma_h E\Omega/RT}\bigg(- \frac{\nabla c}{1-c} + \beta\frac{E\Omega}{RT} c \nabla \hat{\sigma}_h \bigg). \tag{4.2}$$

The dimensionless surface flux in Equation 2.29 is applied as the boundary condition where required. Furthermore, the diffusion-related eigen-strain is treated as thermal strain, and the resulting stress is solved under thermal-stress mode in the dimensionless form with plain strain condition. Note that Lagrangian elements are used to discretize the domains. The material properties of carbon and the parameters used in this investigation were presented in table.

4.3 Planar electrodes

We first investigate planar electrodes, as shown in Figure 4.1. Two configurations are considered, one an infinite electrode extended periodically in lateral direction, while the other with finite width identical to the periodicity of the infinite electrode. Over the top surface, electrode is exposed to electrolyte with constant chemical potential $\mu_e = RT$ and concentration $c_e = 1$ where the electrochemical reaction occurs, and this surface is assumed to be traction free as well. Over the bottom surface, where the electrode is attached to the current collector, no displacement ($u = v = 0$) and normal ionic flux are allowed. For finite electrode, the lateral surface is also exposed to electrolyte with traction free boundary condition. A uniform initial concentration of $c = 0.2$ is assumed, and the simulation stops when the electrode reaches the steady state condition.

In the infinite electrode, due to the periodic and uniform boundary conditions, the concentration profile and stress fields are actually uniform along the lateral direction. Thus, by exploiting the analogy with thermal-stress, the exact stress field at the free surface of the electrode, with ionic concentration c_s, can be found as:

$$\sigma_y = 0; \quad \sigma_x = \sigma_z = -\frac{\nu + 1}{3(1 - \nu^2)} \Omega E c_{max} c_s, \tag{4.3}$$

where ν is the Poisson's ratio and z is out-of-plane direction. This leads to an expression for the chemical potential of ions at the surface of electrode. Therefore, the analytic expression for the dimensionless normal surface flux from the electrolyte into the infinite electrode, as a function of surface concentration, can be found as

$$\hat{\boldsymbol{j}}_s \cdot \mathbf{n} = \hat{K} \left(\hat{S} \frac{1 - c_s}{c_s} e^{\frac{\mu_e}{RT} - \frac{2\beta E(\nu+1)}{9RT(1-\nu^2)} \Omega^2 c_{max} c_s} - \frac{c_s^2}{1 - c_s} e^{\frac{2\beta E(\nu+1)}{9RT(1-\nu^2)} \Omega^2 c_{max} c_s - \frac{\mu_e}{RT}} \right). \tag{4.4}$$

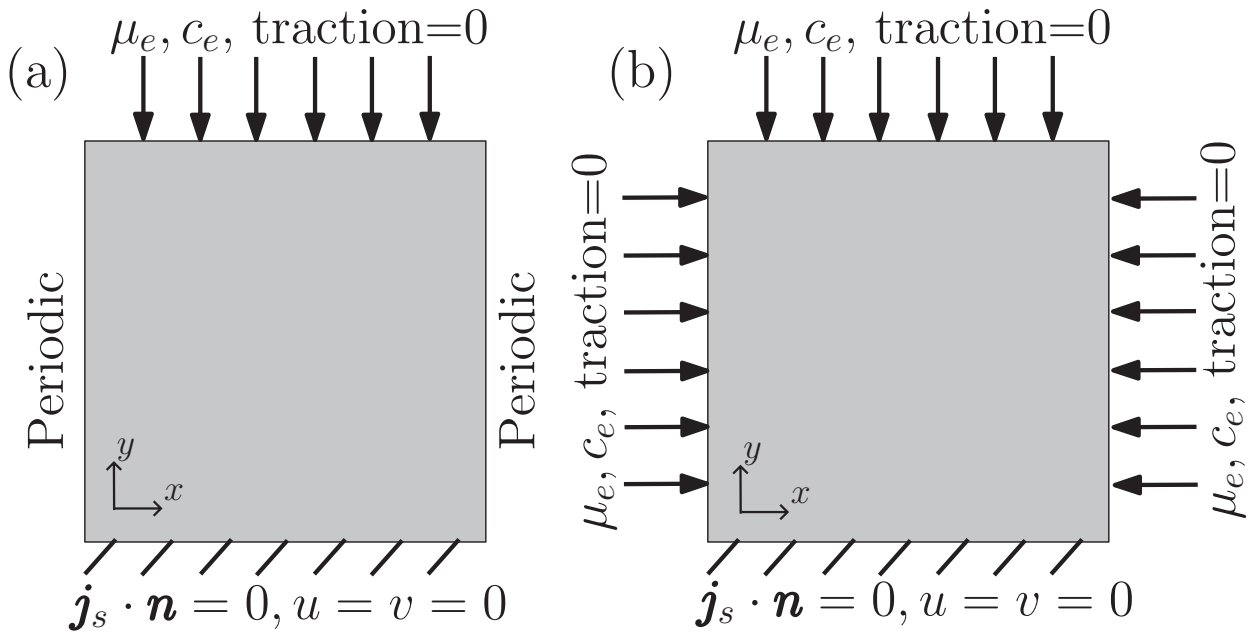

Figure 4.1: Configuration of planar electrodes; a) the unit cell of an infinite electrode extended periodically in lateral direction; and b) a finite electrode with width identical to that of the periodic unit cell and lateral surface exposed. The reactive surfaces are exposed to an electrolyte with ionic chemical potential of μ_e and concentration c_e. The bottom surfaces are attached to the current collector without any horizontal and vertical displacements ($u = v = 0$) and normal ionic flux.

The dimensionless normal surface flux as a function of surface concentration (c_s) for the planar infinite and finite electrodes under coupled and uncoupled ($\beta = 1, 0$) conditions are shown in Figure 4.2. The dots in this figure represent time snapshots of the simulations, and the results for the finite electrode are averaged over the exposed surface area. The analytic solutions for the infinite electrode, coupled or uncoupled with stress (Equation 4.4), are also shown for comparison and validation. Note that the surface flux in the uncoupled model is stress independent and hence is identical for both finite and infinite electrodes. For all cases, the surface flux starts from insertion into the electrode at lower surface concentrations and decreases as the surface concentration increases until reaching the equilibrium state with zero flux. The surface flux is then reversed to extraction for surface concentrations higher than that of equilibrium. This equilibrium concentration (concentration at zero flux) is a function of the stress at the surface of electrode. Therefore the equilibrium concentration is lowest in the infinite electrode, which experiences the highest insertion-induced compressive stress, and is the highest in the uncoupled model with $\beta = 0$. The finite electrode's average surface compressive stress and hence its equilibrium concentration lies in between the other two cases (see Figure 4.4), as the stress state is somewhat relaxed due to the geometry.

At this point, we introduce the capacity of an electrode as the total amount of ions within that electrode

$$\text{capacity} \equiv \int_V c \; c_{max} dV, \tag{4.5}$$

where V denotes the volume of electrode. The time evolution of normalized capacity ($\frac{\text{capacity}}{\text{capacity}_{\text{max}}}$) of the simulated infinite and finite electrodes for coupled and uncoupled models ($\beta = 1, 0$) are shown in Figure 4.3. Note that $\text{capacity}_{\text{max}}$ is defined as the capacity of an electrode containing uniform maximum concentration c_{max}. As can be seen, the finite electrode, in both models, reaches the equilibrium state in a shorter time due to its larger surface area exposed to electrolyte. Moreover, while both infinite and finite planar

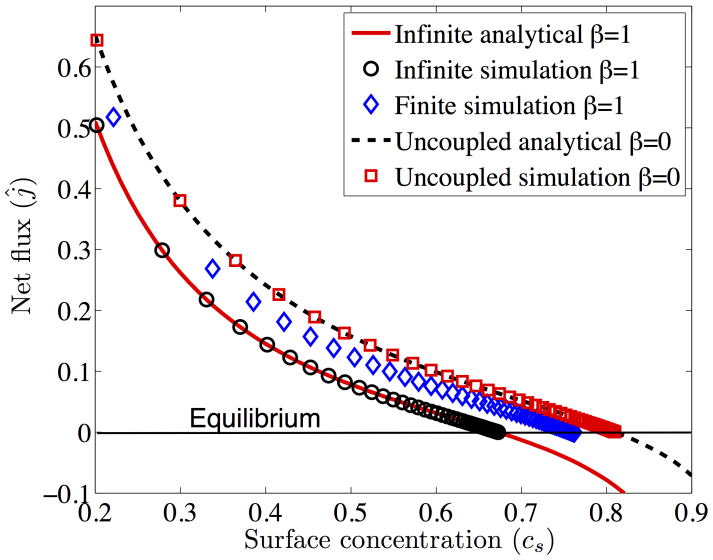

Figure 4.2: Normal surface flux as a function of surface concentration for the planar infinite and finite electrodes under coupled ($\beta = 1$) and uncoupled ($\beta = 0$) conditions.

electrodes under the uncoupled model ($\beta = 0$) converge to the same capacity, the coupled model ($\beta = 1$) predicts lower equilibrium capacities due to the stress effect. The equilibrium capacity of the finite electrode is higher compared to the infinite electrode due to the lower level of insertion-induced compressive stress, and such higher capacity in structured carbon electrodes has indeed been reported in the literature [109].

To appreciate the effect of stress on the kinetics as well as the capacity of electrodes, the distributions of equilibrium concentration and hydrostatic stress within the infinite and finite electrodes under the coupled and uncoupled models are shown in Figure 4.4. The first two rows represent the coupled models and the next two rows represent the uncoupled models. As can be seen, the concentration and hydrostatic stress are uniform within the infinite electrode under both models. This equilibrium concentration is higher in the uncoupled model compared to that of the coupled model, also seen in Figure 4.2. Moreover, within the finite electrode under coupled model (c,d), the location of stress concentration with higher

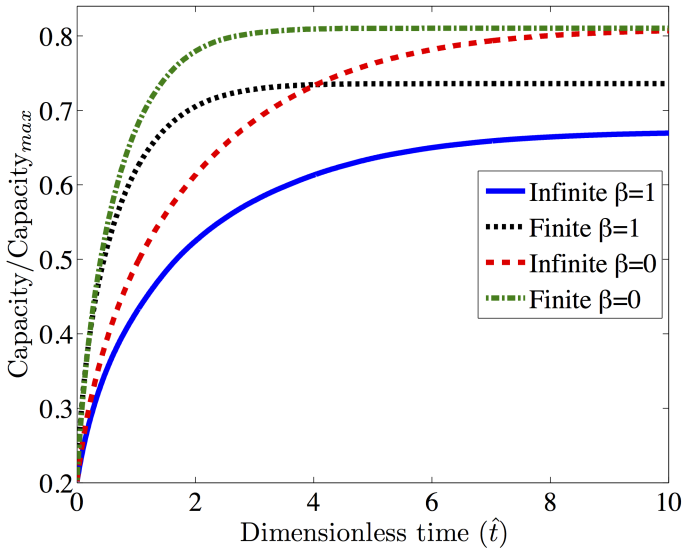

Figure 4.3: Time evolution of capacity of the planar infinite and finite electrodes for coupled ($\beta = 1$) and uncoupled ($\beta = 0$) models.

compressive stress exhibits lower equilibrium concentration, illustrating the coupling between mechanics and electrochemistry. Because of this coupling, finite electrode, with lower stress concentration, exhibit higher capacity than the infinite one. It is worth mentioning that in the uncoupled finite electrode (g,h), while the calculated stress varies, the concentration is uniform and is identical to that of the infinite electrode, because the stress has no influence on the ion concentration.

4.4 Structured electrodes

Based on the results in the last subsection, it is clear that geometry of an electrode has substantial influence on the stress distribution induced by the diffusion, which in turn affects the capacity and rate performance of electrodes. In order to further investigate this effect, we study three structured electrodes with periodic semi-circular, rectangular and triangular patterns using the coupled model $\beta = 1$, as shown in Figure 4.5. Note that the period length

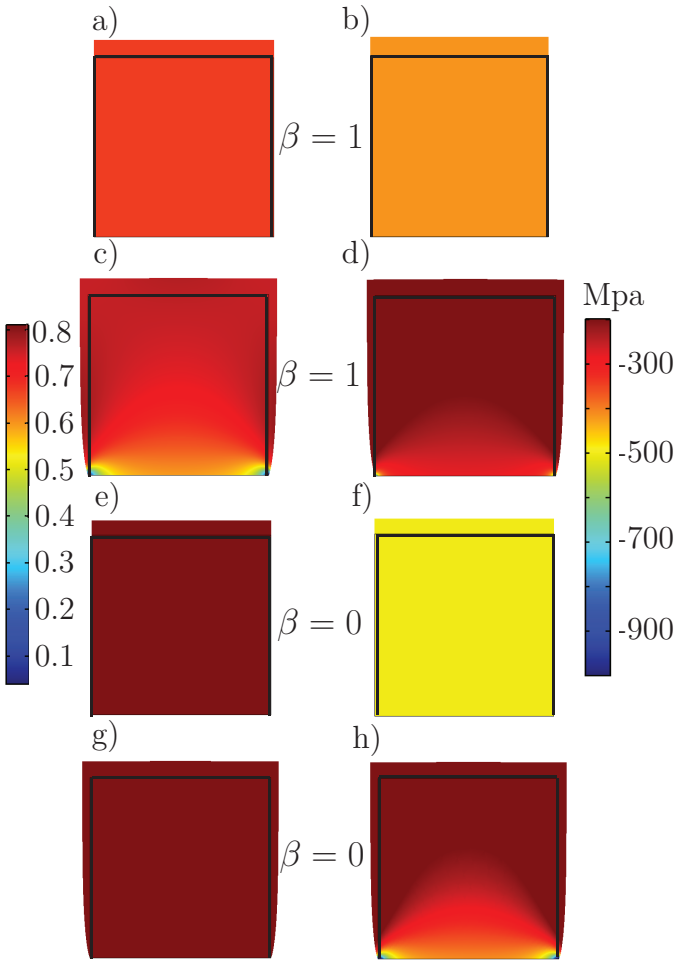

Figure 4.4: Distribution of equilibrium concentration (left) and hydrostatic stress (right) of planar (a,b,e,f) infinite and (c,d,g,h) finite electrodes under coupled $\beta = 1$ and uncoupled $\beta = 0$ models.

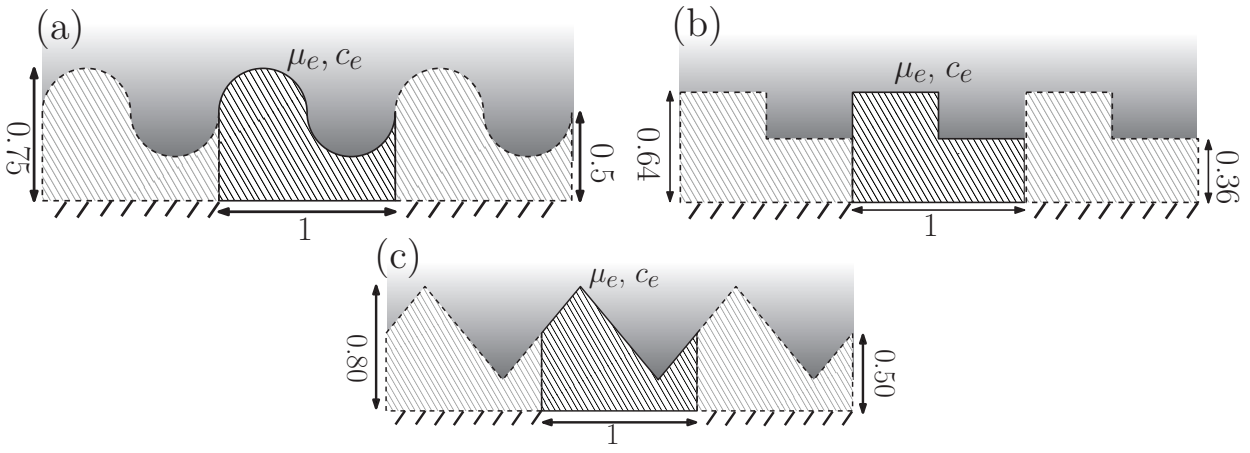

Figure 4.5: Configurations of structured electrodes; the unit cell of a) semi-circular, b) rectangular and c) triangular electrodes extended periodically in lateral direction. The reactive surfaces are exposed to an electrolyte with ionic chemical potential of μ_e and concentration c_e. The bottom surfaces are attached to the current collector without any horizontal and vertical displacements ($u = v = 0$) and normal ionic flux.

of the structures is chosen as the reference length scale (see Chapter 2), and the dimensions are set such that the reactive surface area and volume of all the electrodes are kept the same. For comparison, an infinite electrode with the same volume is investigated as well.

In the model configuration depicted in Figure 4.5, the top surfaces of electrodes are exposed to electrolyte with constant chemical potential $\mu_e = RT$ and concentration $c_e = 1$. The surface reaction over the top surfaces produces a flux normal to the electrode surface as was expressed in Equation 2.29. The bottom surfaces of the electrodes, attached to the current collector, are considered mechanically fixed with zero normal flux.

The equilibrium concentration along the arc-length of the electrode-electrolyte interface (top surface) for the structured electrodes are illustrated in Figure 4.6. The drastic drops of concentration for the triangular and rectangular electrodes corresponds to the concave edges of these electrodes, which experience the highest compressive stress. In contrast, the convex edges accommodate the maximum concentration due to the lowest compressive

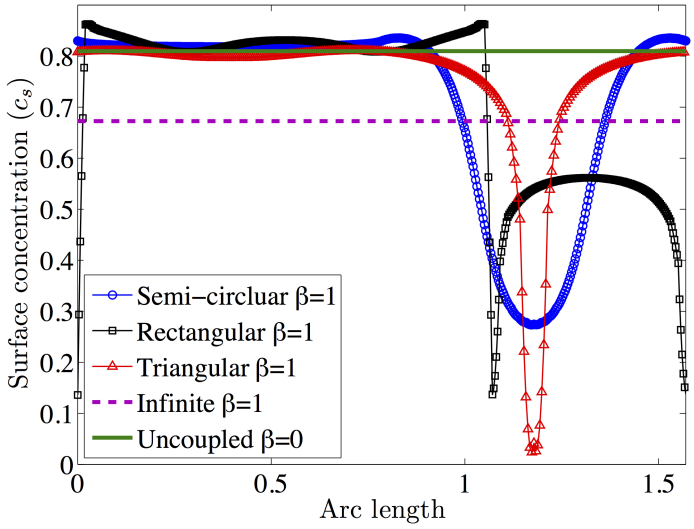

Figure 4.6: Equilibrium surface concentration along the reactive interface arc length.

stress level. The concentration profile over the semi-circular electrode is smooth, yet similar concentration drop can be observed in the concave area. Moreover, the concentration over the pillar section of the rectangular electrode is comparable to that of the uncoupled model, while the concentration over the base section is lower than that of the infinite electrode due to stress concentration.

The time evolution of normalized capacity of the semi-circular, triangular and rectangular electrodes as well as the infinite electrode are shown in figure 4.7. Electrodes with different structures converge to different equilibrium capacities, dependent on their respective stress state. The electrode with semi-circular structures converges to the maximum equilibrium capacity due to the the least average compressive stress state, while the electrode with rectangular structures converges to the minimum equilibrium capacity. This low capacity is associated with the high difference between the average hydrostatic stress in the base and pillar sections, which results in high concentration difference between these sections (as was also seen in Figure 4.6). Note that the time required for the infinite electrode to reach

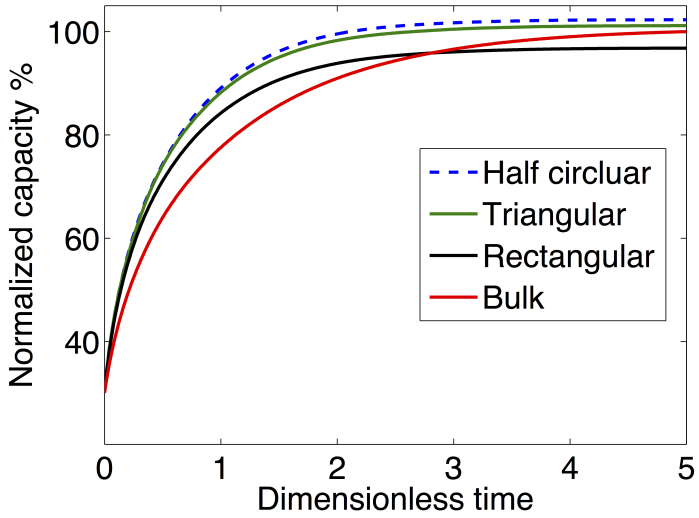

Figure 4.7: Time evolution of the normalized capacity of the structured electrodes.

equilibrium state is longer compared to the structured electrodes because of the least exposed area.

The distributions of equilibrium concentration and hydrostatic stress within the structured electrodes are shown in Figure 4.8. They are uniform within the infinite electrode while spatially varying for the structured electrodes. Because of the coupling, a correlation between concentration and induced hydrostatic stress within the electrodes is observed. For example, the areas close to the concave edges that experience the highest compressive stress accommodate the lowest ion concentration. Moreover, the previously discussed concentration difference between the base and pillar sections of the rectangular electrode can be observed as well.

4.5 Conclusion

In this study planar electrodes with different boundary conditions as well as structured electrodes with different geometries were investigated using the developed model. The elec-

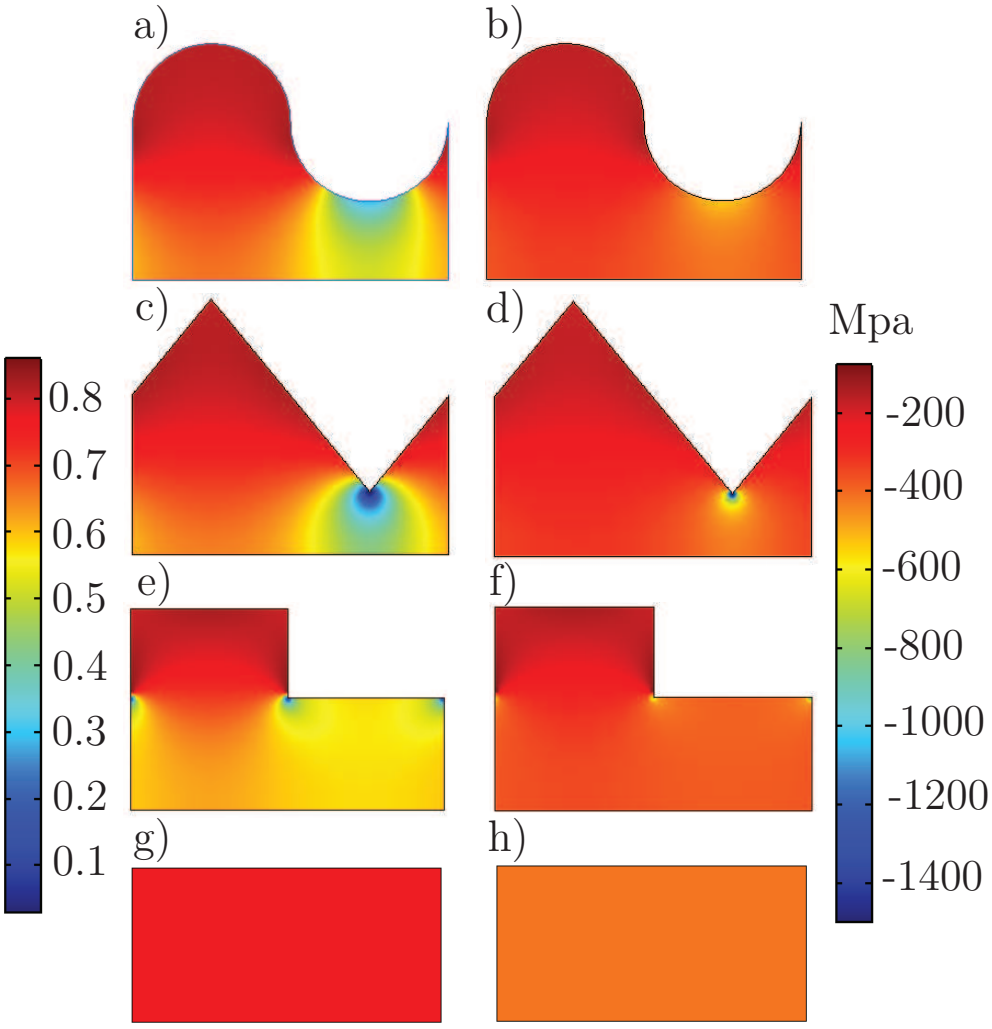

Figure 4.8: Distribution of equilibrium (a,b,c,g) concentration and (d,e,f,h) hydrostatic stress within a unit cell of the structured electrodes.

trodes were analyzed in charging condition until reaching an equilibrium with the exposed electrolyte. The coupled model predicted varying equilibrium concentration at the surface depending on the stress state of electrode, illustrating the important role of compressive stress, which tends to reduce the ion concentration, and thus the capacity. Furthermore, faster kinetics is also observed in the structured electrodes due to larger surface area and reduced stress. Among the geometries considered, semi-circular shaped electrode exhibits the highest capacity, though we believe that it can be further optimized. The presented modeling framework thus can be used to not only understand the effects of stress on the battery performance, but also design and optimize structured battery electrodes with improved performance. The conclusion of this chapter motivates the next chapter for optimizing the geometry of electrode to achieve the optimum performance.

Chapter 5

PERFORMANCE OPTIMIZATION OF STRUCTURED BATTERY ELECTRODES

5.1 Introduction

In Chapter 4 we analyzed the structured electrodes under charging with three different periodic geometry patterns using the described coupled model in Chapter 3.7. We observed that the investigated electrodes reach to different ultimate capacity levels, due to different stress states generated in that electrodes. Furthermore, faster kinetics was predicted in the structured electrode due to lower compressive stress state and larger surface area.

This observations motivates this chapter to find the optimum geometry this chapter. For this purpose, we employ the coupled modeling framework developed in Chapter 3.7. The numerical implementation and the optimization framework are discussed in Section 5.2. The geometry of structured electrode are expressed mathematically using Gaussian functions with three dimensionless design variables. The coupled model is implemented into COMSOL finite element platform and is operated via a Matlab code to simulate the electrodes performance with various geometries. The effect of the design parameters on the performance of the structured electrodes are investigated in Section 5.3, using the simulation results to find the geometry with the optimum capacity and charging time. Eventually the optimum design parameters are presented and discussed.

5.2 Optimization framework

The presented modeling framework in Chapter 3.7 is utilized to design a structured electrode pattern with improved performance. In this study, considering the experimental fabrication characteristics [109], we investigate 2D patterned electrodes with periodic structures as the schematic of a unit cell is shown in Fig 1(a). The structure extends periodically in the lateral direction, and the reactive top surface is exposed to an electrolyte with chemical potential μ_e and concentration $c_e = 1$. The bottom surface is fixed to the current collector with no horizontal or vertical displacement ($u = v = 0$) and no normal ionic flux. The third dimension is considered to be long resulting in plain strain mechanical condition.

For the considered electrode geometry, there are four lengths to be controlled and characterize the electrode geometry (as shown in Fig. 1(a)). However, for the simulation purpose in the dimensionless form, we normalize the lengths with respect to the reference length ($L = a + b$) and introduce three dimensionless design variables of, pattern fraction, electrode thickness and pattern height to thickness ratio respectively as,

$$\lambda = \frac{a}{a+b} \qquad T = \frac{d}{a+b} \qquad H = \frac{h}{d} \tag{5.1}$$

Furthermore, in order to fully represent the geometry for the simulations, we mathematically express the electrode surface profile $p(\hat{x})$ for one cell $0 \leq \hat{x} \leq 1$, with three fourth order Gaussian functions as,

$$p(\hat{x}) = \begin{cases} c + de^{-fs^4}, & 0 \leq s = \hat{x} \leq 0.5 - \lambda/2 \\ a + be^{-gs^4}, & -\lambda/2 \leq s = \hat{x} - 0.5 \leq \lambda/2 \\ c + de^{-fs^4}, & -(0.5 - \lambda/2) \leq s = \hat{x} - 1 \leq 0 \end{cases} \tag{5.2}$$

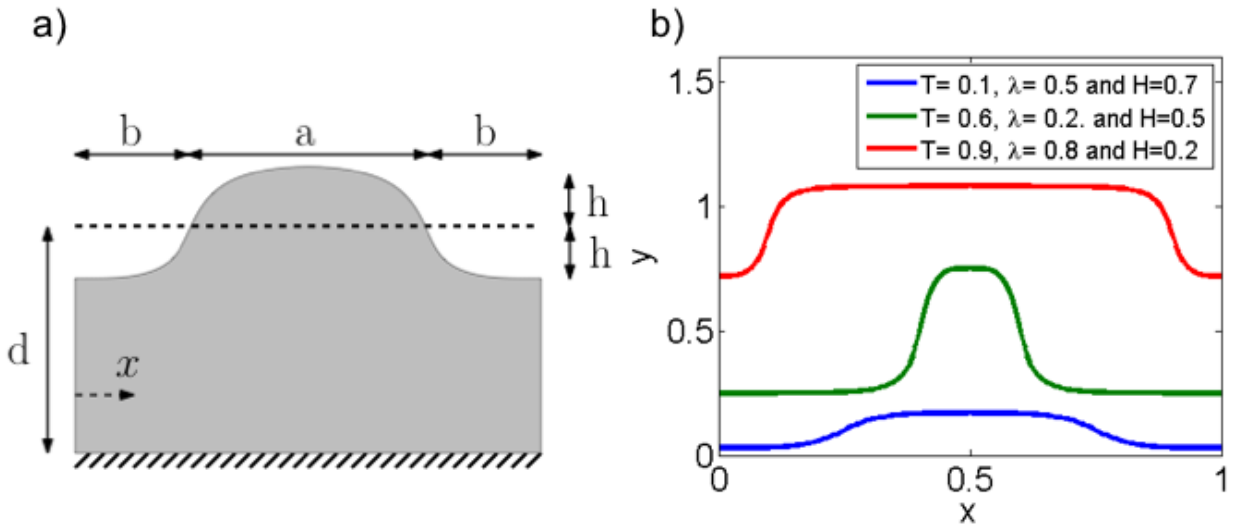

Figure 5.1: a) Configuration of a unit cell of structured electrodes with patterns extended periodically in the lateral direction. The reactive surface on top is exposed to an electrolyte with ionic chemical potential of μ_e and concentration c_e. The bottom surface is attached to the current collector without any horizontal and vertical displacements ($u = v = 0$) and normal ionic flux. b) The mathematically generated surface profiles with different design variables.

where s is the shifted position defined for each part of the profile and a, b, c, d, e, f, g are the coefficients of the profile that are needs to be determined from the smoothness and continuity of the profile and the geometry design variables λ,T and H. The mathematically formulated electrode geometry, is plotted in Fig. 1(b) for three different combinations of the design variables.

On every design process there are restrictions applied from the fabrication process condition. In this study we consider the fabrication process criteria for structred electrodes from [109], where the electrode lengths varies $200\mu m \leq a, b \leq 1000\mu m$, $400\mu m \leq d \leq 1000\mu m$ and the pattern height h varies from 5% to 99% percent of thickness. For the optimization, the considered ranges for and are discretized with $200\mu m$ steps, while the h range is discretized every 5% of the thickness. A directory of all possible combinations of the

dimensionless design variables λ, T and H corresponding to the discretized lengths is then prepared for simulations.

Finally, finite element method is used to numerically solve the governing coupled partial differential equations implemented in a Comsol Multyphysics Livelink model [72]. For each simulation case from the directory, Matlab is used to generate the electrode geometry from Eq. 8, run and postprocess the simulation results. In the following simulations results, for demonstration graphite is regarded as the electrode material, and its material properties as well as other parameters used are listed in Table 1.

5.3 Results and discussion

In this section we investigate the effect of the geometry deign variables λ, T and H on the diffusion of Li-ions in charging, the ultimate capacity and charging time. The electrode with optimum performance is then found among the considered geometries in the prepared directory. In order to examine the effect of stress on the capacity of electrodes, the equilibrium concentration and hydrostatic stress distributions for a structured electrode are shown in Fig. 2(a,b). Note that equilibrium condition is when the electrode is fully charged to its ultimate capacity. Due to the coupling, the locations with high compressive stress states correspond to a low concentration. Therefore, in general, higher generated compressive stress within the electrode volume results in lower ion concentration and thus lower capacity in that electrode. The evolution of the normalized capacity of electrodes with different geometries, shown in Fig. 2(c), reveals the electrode geometry effect on the ultimate capacity and charging time. Note that capacity of an electrode is defined as the total amount of ions within that electrode and are normalized with respect to the ultimate capacity of a bulk electrode with the same volume. Among the compared electrodes with variable pattern height (Fig. 2(c)), the electrode geometry with taller patterns relaxes the generated stress more and reaches

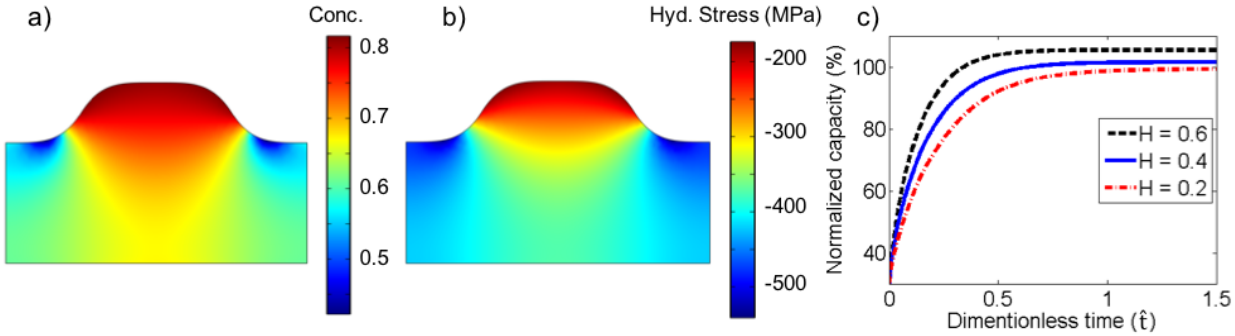

Figure 5.2: Distribution of equilibrium a) concentration, and b) hydrostatic stress of a structured electrode with $\lambda = 0.5$, $H = 0.2$, $T = 0.5$. c) Time evolution of normalized capacity of structured electrodes, with respect to the ultimate capacity of a bulk electrode with the same volume, for different H values and $\lambda = T = 0.5$.

to the higher ultimate capacity, while it is charged faster due to the higher surface area and more relaxed surface stress. This observation has indeed been experimentally reported before [109].

In order to find the optimum structured electrode geometry among the considered cases, we investigate the effect of the design variables λ, T and H on the ultimate capacity and charging time.

The effect of the patterns height to thickness ratio H on the ultimate capacity improvement, compared to the bulk electrode with the same volume, is shown in Fig. 3(a). Note that for each point, the maximum capacity value with the specified H parameter is shown. The capacity starts close to no improvement for the low values of H, which is expected due to shape similarity to a bulk electrode. As H increases, the ultimate capacity improvement increases exponentially, that is associated to the higher stress relief by extracting more material around the pillar patterns. The maximum ultimate capacity is reached by almost fully extracting the material around the patterns at $H = 0.99$. Also the effect of the pattern fraction λ and thickness T are shown in Fig. 3(b); where each point shows a simulation

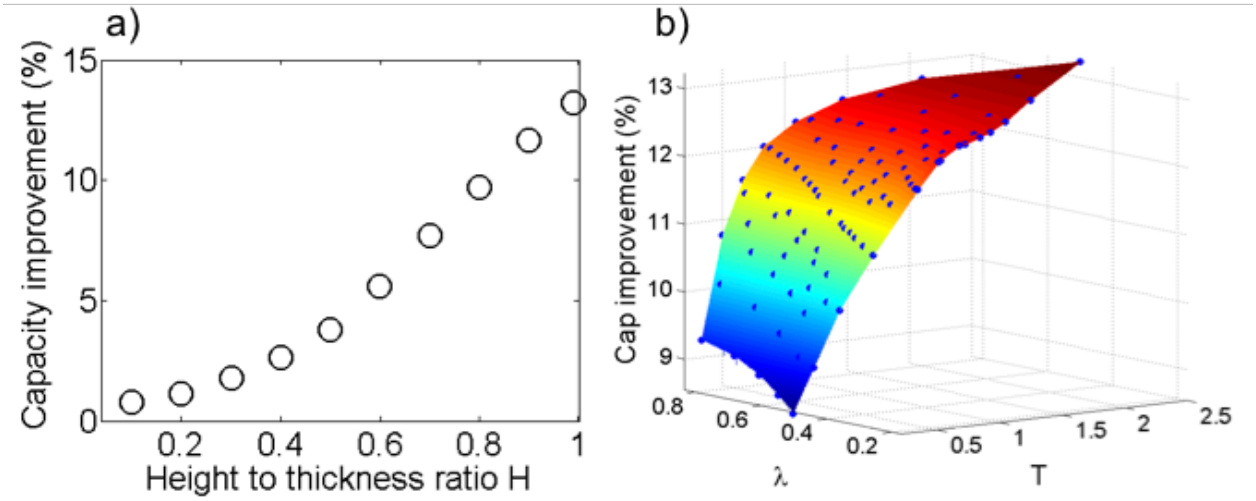

Figure 5.3: Ultimate capacity improvement, normalized with the ultimate capacity of a bulk electrode with the same volume, against a) pattern height to thickness ratio H, and b) dimensionless thickness T and pattern fraction λ.

case from the directory and its color represents the capacity improvement of the specified geometry with $H = 0.99$. The results reveal that electrodes with smaller pattern fraction have slightly higher ultimate capacity compared to the ones with greater fraction. Also, the ultimate capacity increases as the dimensionless thickness increases. The reason is the lower compressive stress generated in the geometries with taller patterns that have more stress relaxed area.

Moreover, the effect of the design variables on the normalized charging time, with respect to that of a bulk electrode with the same volume, are shown in Fig. 4(a). Note that the charging time is considered as the time to reach 95% of the ultimate capacity. The exposed surface area of the electrode and the stress state at the surface of the electrode affect the kinetics and charging time of the electrode, with the former is found to be more dominant. The electrodes with higher pattern height to thickness ratio H are charged faster, due the higher exposed surface area and more relaxed stress, while the charging time approaches

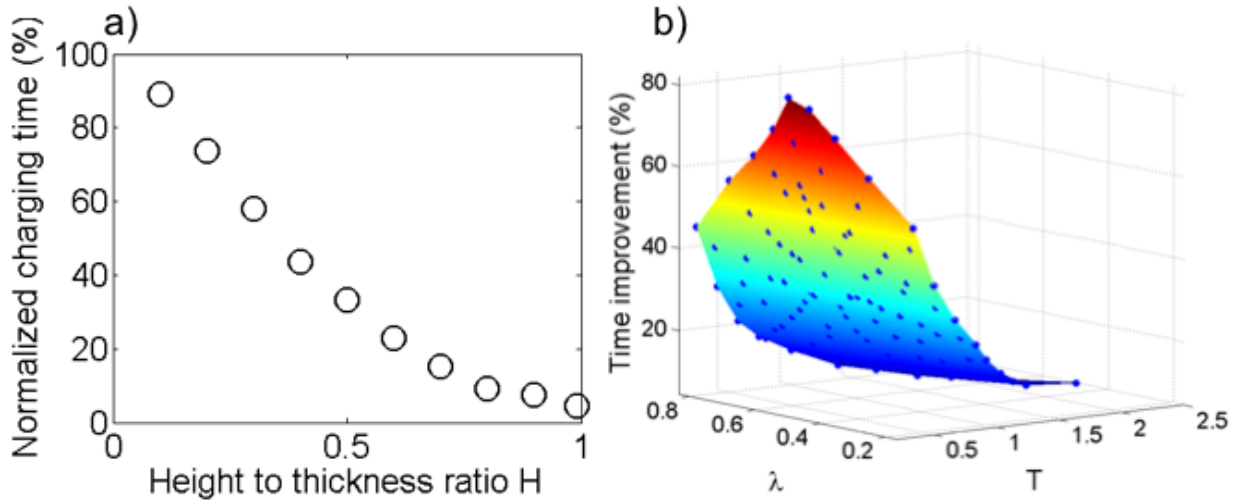

Figure 5.4: Normalized charging time, normalized with the charging time of a bulk electrode with the same volume, against a) pattern height to thickness ratio H, and b) dimensionless thickness T and pattern fraction λ.

to that of a bulk electrode for low H values. Also the effect of the pattern fraction λ and thickness T, with fixed $H = 0.99$, on the normalized charging time are shown in Fig. 4(b). Electrodes with greater pattern fraction λ show slightly lower charging time, while electrodes with higher height T show lower charging time. The dramatically higher surface area in such electrode rules the lower charging time compared to that of a bulk electrode.

Among considered geometries in this study, the optimum ultimate capacity of almost 13% higher than that of a bulk electrode with the same volume is expected to be achieved in the structured electrode with $H = 0.99$, $\lambda = 0.5$, $T = 2$. The time required to charge this electrode is also minimum among the considered geometries which is ideal. Note that the shape of the geometry with optimum performance is close to a pillar shape, which is consistent with the geometry of some of the recent high performance micro-structured electrodes [39].

5.4 Conclusion

In this chapter we adopted the developed thermodynamics-based modeling framework in pervious chapters to optimize the geometry of electrode to achieve optimum performance. In the previous chapter, our model predicted different ultimate capacities for electrodes with different geometries because of the coupling between mechanics and geometry. Therefore, in this chapter the goal was to find a geometry with the optimum performance. To this end, a mathematical description of the periodic surface profile with three design parameters was developed to fully describe the electrode geometries. Many electrode models with possible geometries were analyzed and postprocessed in Matlab with Comsol Livelink solver engine. The effect of the design parameters on the ultimate capacity and the charging time of the electrodes were investigated in the practical range. The geometry with the lowest stress state resulted in maximum ultimate capacity and minimum charging time. Finally, the electrode with optimum performance was presented.

Chapter 6

ELECTROCHEMICAL STRAIN MICROSCOPY: MODELING AND EXPERIMENT

6.1 Introduction

Electrochemical strain microscopy (ESM) is a relatively new scanning probe microscopy technique developed at Oak Ridge National Laboratory in 2010 [11, 9]. This method is recently used to probe the local electrochemical dynamics in solids and employed to investigate the active materials in energy storage and fuel cell systems.

The basics of this technique is to apply a time variant voltage, consisting DC and AC components, to the AFM tip to induce ion redistribution through diffusion or electrochemical mechanisms. The variations in the ion concentration results in molar volume variation and yet surface deflection beneath the SPM tip. This deflection is captured via the vertical and lateral motion of the cantilever and then detected through measuring the position of the reflected laser off the top surface of the cantilever. This measurements are very accurate to be able to measure small deflections of the cantilever. The schematic of the ESM technique is shown in Figure 6.1.

This technique is similar to the well-known piezoresponse force microscopy (PFM) technique for ferroelectric materials, which is widely used to probe ferroelectric materials. However, the ESM response interpretation is more complicated than the PFM response which is formed due to the piezoelectric mechanism. For instance, in a recent study, Chen et. al [20] showed that electrostatic and other effects can contribute to the ESM response. Therefore a detailed understanding of the ESM response signal formation and the different aspects

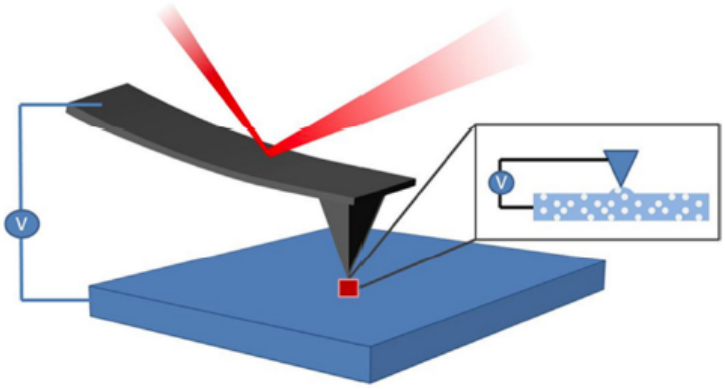

Figure 6.1: Schematic of electrochemical strain microscopy.

associated to the experiments, is essential.

There are different possible operation modes of the ESM technique. In this chapter we consider the operation mode that the tip induces an electric field that results in redistribution of ions beneath the tip but no electrochemical reaction occurs. The governing mathematical equations are implemented into Comsol and different aspects of the experiments are modeled numerically. The experiments complemented the modeling results through the chapter. At last the limitations and the complications of this technique are introduced.

6.2 Numerical Implementation

In this section, we explain the configuration of the investigated electrode-probe system and the employed numerical methods to solve the governing equations. In the schematic of the domain configuration shown in Figure 6.2, the electrostatic, electrochemical and mechanics governing equations and the boundary conditions are shown respectively from left to right. At each time-step, the potential, concentration and stress distributions are calculated by the electrostatics, electrochemical and mechanics solvers respectively, and passed to counterpart solver. Here, we consider an axisymmetric model geometry with the probe tip shown as a

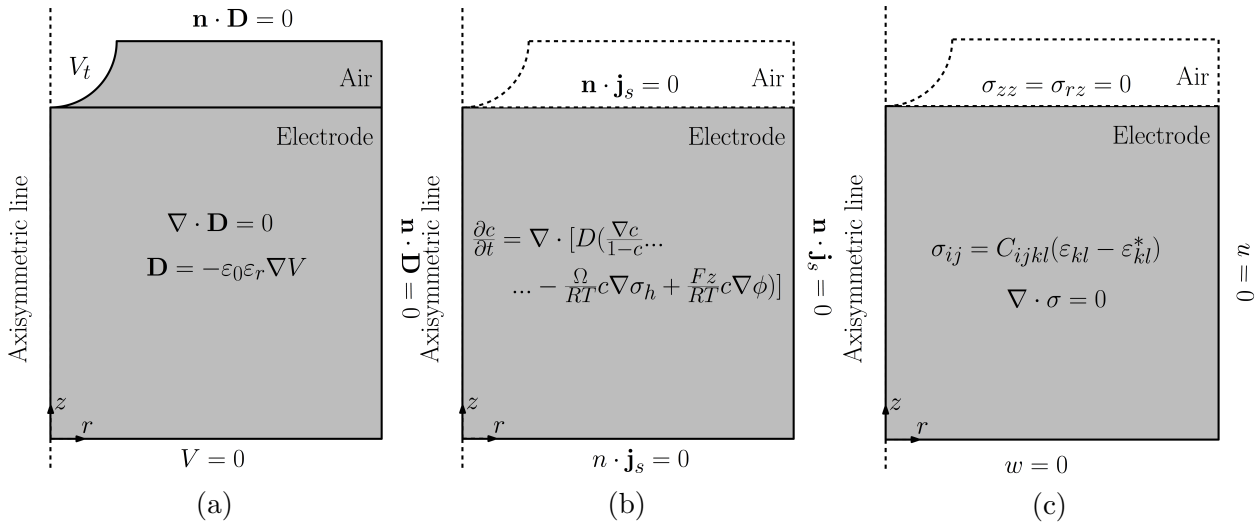

Figure 6.2: Configuration of axisymmetric model of ESM and the governing equations for (a) electrostatics, (b) electrochemistry and (c) mechanics. The bias V_t is applied to the tip on top of the electrode, the lower electrode surface is grounded ($V_t = 0$) and no electric charge ($\mathbf{n}\cdot\mathbf{D} = 0$) or ionic flux ($\mathbf{n}\cdot js = 0$) on the boundary surfaces. The lower surface of electrode is fixed in the vertical direction $w = 0$, the side surface is fixed in the radial direction $u = 0$ and the top surface of electrode is free ($\sigma_{zz} = \sigma_{rz} = 0$).

quarter circle and the surrounding air placed above the electrode. The electrostatic solver, solves for the potential field over the whole domain consisting electrode and the air. The probe potential is V_t, the bottom of the electrode is grounded, and the side surfaces have zero charge. The electrochemistry solver, solves for the concentration distribution within the electrode and considers the coupling with electric field and mechanical stress. The flux is considered to be zero over the boundaries. The mechanics solver, solves the mechanical equilibrium equation to find the hydrostatic stress field. The bottom surface and side surfaces are fixed with $w = 0$ and $u = 0$ respectively and the top surface is free.

This configuration is implemented into the Comsol multiphysics to solve the governing equations using Finite Element method. The material properties of graphite is used for the following simulations.

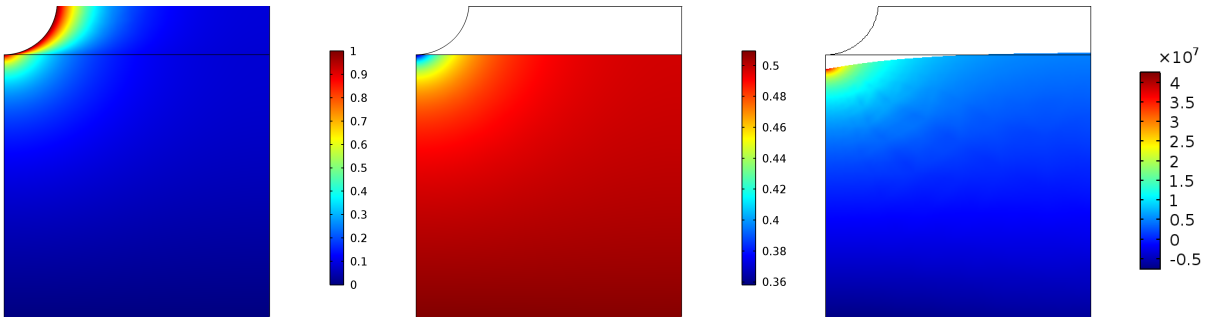

(a) (b) (c)

Figure 6.3: Distributions of a) potential, b) concentration and c) hydrostatic stress over deformation within the domains under a unit constant potential to the tip. Note that the positive potential repelled the ions and a downward deformation of the surface.

6.3 Results and Discussion

In this section the results of simulating a probe-electrode system is presented. The field parameters distributions with application of a unit constant voltage to the tip is shown in Figure 6.3. The potential distribution within the electrode and the surrounding air is shown in left. The potential is high around the probe and decreases farther from the probe surface. The discontinuity in the potential is because of the permittivity coefficient difference between the electrode and air. The ion concentration distribution is shown in the middle figure. The concentration is lower around the tip with higher positive potential that repels the ions. However, since the ions are conserved within the electrode, the concentration is higher at the bottom of the electrode. The hydrostatic stress field overlaid on the deformation is shown in the right figure. Around the tip with low concentration has the lowest compressive stress, while the surface moves downward.

ESM principle works with oscillating electric fields, therefore in order to verify our model in such condition we apply an oscillating voltage as shown in Figure 6.4(a). The resultant concentration variation beneath the tip and surface deformation are shown. As can be seen

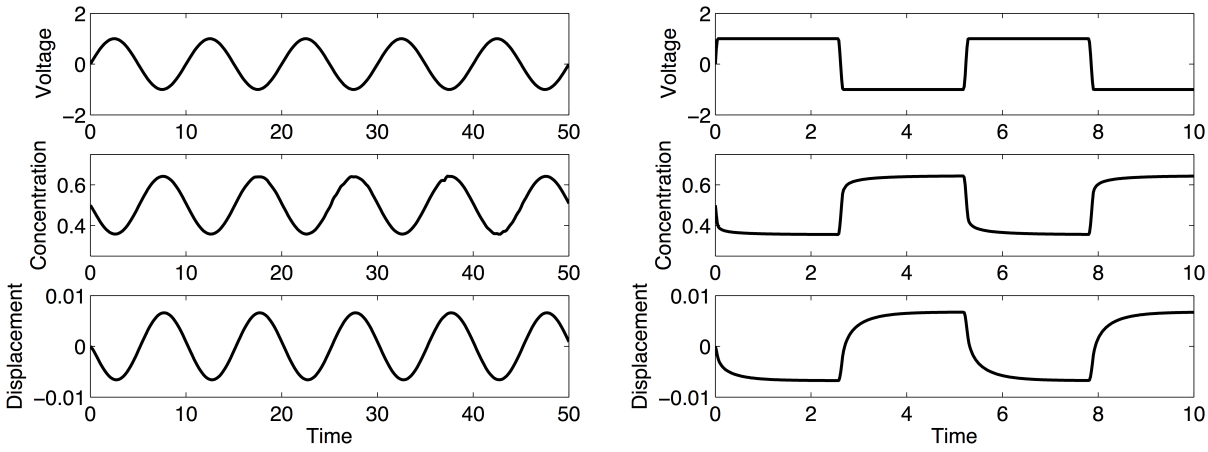

Figure 6.4: Applied sinusoidal and stepwise bias and the resulting concentration and displacement beneath the tip.

in such low frequency the concentration and deformation track the potential profile with 180 degree phase lag, which is because of the positive charge of ions.

Furthermore, the response of ions under step-like potentials is shown in Figure 6.4(b). The concentration and the resultant deformation response show a relaxation behavior. The relaxation profile gives information about the diffusion coefficient of ionic motion.

The frequency response of the displacement amplitude is shown in Figure 6.5. The displacement amplitude response is high in lower frequencies and dependent on the sample thickness due to the large penetration depth. However in high frequencies, which is the working frequency of ESM, the response decreases drastically. In order to detect such small responses, ESM works around the resonance frequency of the tip sample contact. Also, the high frequency response is not thickness dependent due to the small penetration depth. The phase also starts with 180 degree shift in low frequencies and changes 90 degree in high frequencies.

Another crucial aspect of the ESM measurement is the correlation between the average

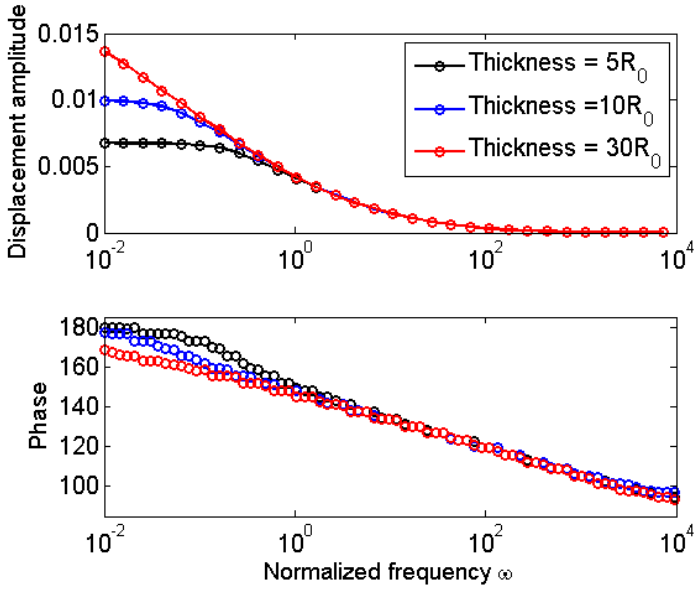

Figure 6.5: ESM displacement and phase transfer function.

concentration level and the displacement amplitude that is the fundamental of concentration mapping. Such relation is investigated via simulation for a linear diffusion model and the considered nonlinear model and shown in Figure 6.6. The relation shows that there is an increase in the displacement amplitude as the average concentration level increases for both models. However, for the nonlinear model because of the maximum concentration at $c = 1$, the response deviates from linearity at high concentrations.

In order to further appreciate the concentration sensitivity of ESM, a 3D model of the experiment is built. The average applied concentration level of the surface of the electrode is shown in Figure 6.7(b). This assimilated electrode is virtually probed using the ESM model and the displacement amplitude mapping is shown in Figure 6.7(c). This mapping, which is the output of an ESM mapping experiment, clearly corresponds to the variation in average concentration level of the electrode.

Nano-crystalline Ceria, is a well known electrode for fuel cells, and is known for its higher

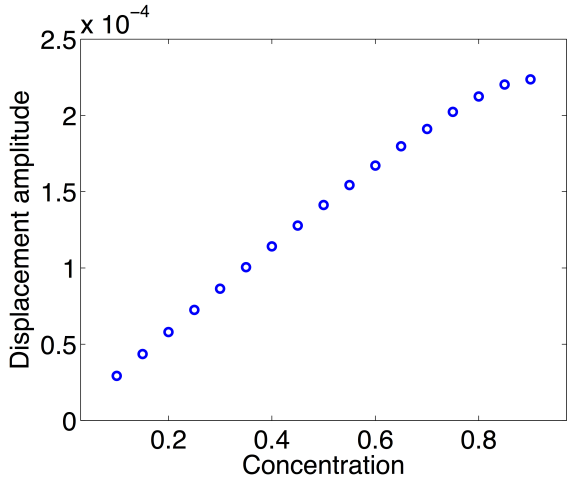

Figure 6.6: Displacement amplitude vs concentration.

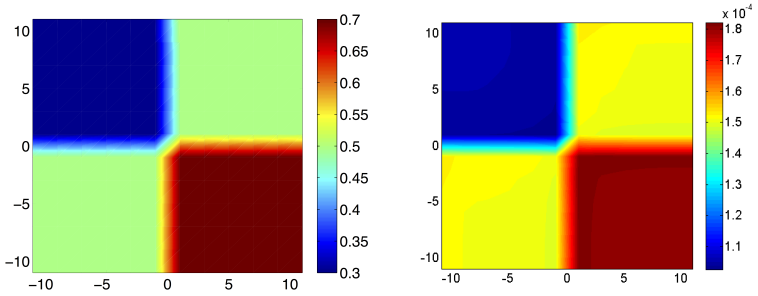

(a) (b)

Figure 6.7: a) Pre-Imposed concentration distribution and b) calculated ESM displacement amplitude mapping on Ceria.

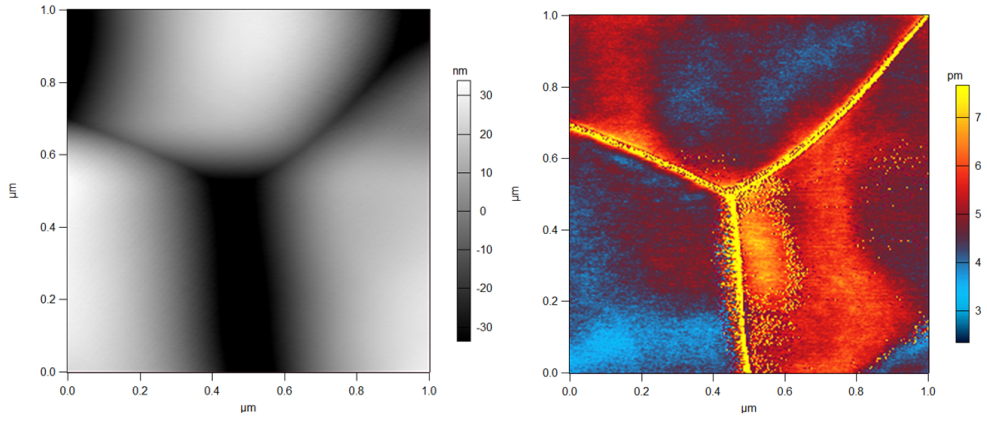

(a) (b)

Figure 6.8: a) Topography and b) ESM displacement amplitude on Ceria.

ionic conductivity compared to non-processed Ceria. Such behavior is considered to be due to higher ionic conductivity over the grain boundaries [103]. In this part we probe a nano-crystalline Ceria sample using the ESM mapping. The topography and ESM displacement amplitude mappings are shown in Figure 6.8. As the simulation results suggested, the higher amplitude at the grain boundaries shows the higher concentration level at these locations, which is consistent with the previous studies.

Spectroscopy is an important aspect of the ESM experiments for investigating the diffusion of ionic species. In the spectroscopy experiment, a DC bias waveform, as schematically shown in Figure 6.9(a), is applied to the tip while the AC bias is simultaneously applied to measure the concentration of species. Note that the DC bias drops to zero (OFF state) after some increase in the each step (ON state). The true measurements are conducted in the OFF states to avoid the electrostatic measurements in the ON states.

Such experiment, with the presented DC and AC waveform, is implemented into the current Comsol model. The output displacement profile is extracted from the model and the amplitude of the AC variations are computed using Fourier transform. The displacement

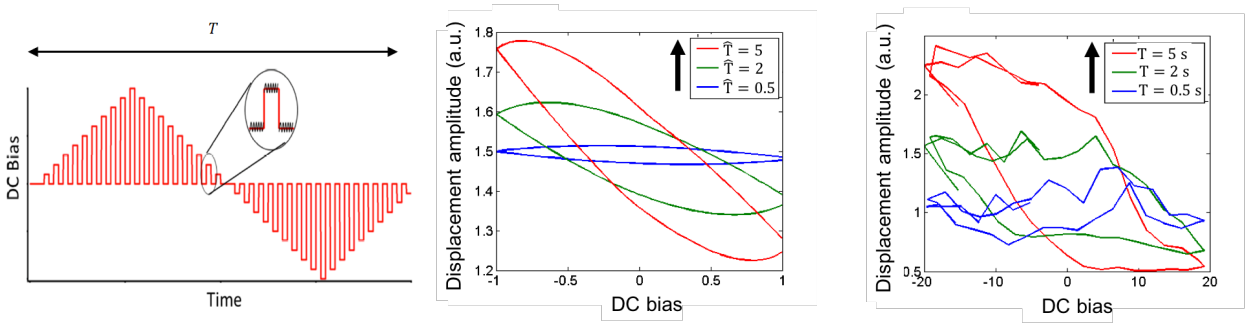

(a) (b) (c)

Figure 6.9: a) ESM spectroscopy waveform, and the resulted displacement amplitude vs DC bias hysteresis loops for a) simulation and b) experiment on $LiFePo_4$ with different periods (T).

amplitude in the OFF shows hysteresis loops against the voltage variation as shown in Figure 6.9(b). Also, the displacement amplitude value, that is related to the ionic concentration is higher in the negative bias that attracts the ions and results in higher concentration (species have positive charge). Also the amount of displacement amplitude and loop's area increases as the period of bias waveform increases. The reason is the required time for diffusion of ions that increases the concentration variation. The described behaviors of the spectroscopy loops are indeed observed qualitatively in the experiments as shown in Figure 6.9(b).

Although Electrochemical Strain Microscopy is proved to be a powerful technique to probe electrochemical activities, there has been serious questions and issues that are being discussed in the community. Recently, there has been a number of works [20, 82] reporting the domination of other contributions, such as electrostatic and dipoles, to the measured response in ESM. For instance, as showed in this chapter, the spectroscopy response due to contribution of ionic activities takes the loop shape. However, the several researchers [20, 82] observed the butterfly-shape spectroscopy reposes on materials that are know to be ionic (which could be due to electrostatic or dipole). This complications limits the application of

ESM for probing electrochemical activities. These limitations motivates us to move to the Chapter 7 to overcome some of the difficulties.

6.4 Conclusion

In this chapter, a mathematical model of the electrochemical strain microscopy (ESM) was developed and implemented into Comsol Multiphysics as an axisymmetric model for numerical solutions. The model was used to investigate various experimental aspects of the technique. The basic results of modeling periodic bias was investigated and discussed as the working principle of ESM. The study was extended to predict the frequency function of the displacement amplitude. The results showed the decreasing trend of the displacement amplitude as a function of the frequency.

The relation between the baseline concentration and displacement amplitude was also investigated. The result showed that the locations with higher concentration have higher displacement amplitude response. This behavior is the principle for ESM mapping. Furthermore, in order to model the ESM mapping, the finite model was extended to 3D and a predefined concentration was imposed into the domain. The resulted displacement amplitude was mapped over the surface of the domain and showed a correspondence to the imposed concentration distribution. This confirms the ESM mapping principle and possibility. The experimental ESM mapping on Ceria complimented the model.

Also, the ESM spectroscopy which is the the combination of DC and AC applied biases to the probe is modeled. The displacement amplitude as the function of the applied DC bias showed the expected spectroscopy loops. The effect of spectroscopy total time was investigated and compared for the model predictions and and experiments. The modeling results qualitatively agreed to the experimental measurements.

Lastly the serious limitations and complications of the ESM technique is discussed. This

limitations motivates developing a new technique that can overcome the difficulties involved in ESM.

Chapter 7

SCANNING THERMO-IONIC MICROSCOPY FOR PROBING LOCAL ELECTROCHEMISTRY AT THE NANOSCALE

7.1 Introduction

Electrochemistry is essential for energy conversion and storage in a wide variety of systems including lithium ion batteries [99, 114, 74], solid oxide fuel cells [78], supercapacitors [94], and resistive switching memristors [97, 92]. A growing body of research suggests that electrochemical processes underpinning these applications are largely governed by phenomena occurring at the nanoscale, such as ionic defect formation and transport [81, 1], interfacial chemistry and charge transfer [90, 28, 43], local cation segregation [52, 59], and phase nucleation and separation [77]. However, a deep fundamental understanding of these microscopic mechanisms, as well as technological advancement, is largely hampered by a lack of experimental techniques that can directly probe electrochemical processes at the nanoscale. Traditionally, many electrochemical characterization techniques are based on the measurements of current and voltage, which are very difficult to scale down to nanometer lengthscales, and which require detection of small currents (on the order of pA) that are beyond the capability of conventional charge amplifiers [53]. Although scanning electrochemical microscopy (SECM) utilizes custom-made ion-conducting electrodes to study local electrochemistry [3], it is typically limited to micrometer length scales [13, 12]. Over the past several years, researchers have begun to employ Vegard strain [31, 105], i.e. the strain associated with changes in defect concentration, to provide an alternative imaging mechanism for electrochemical processes with high spatial resolution. For example, the topography variation of

electrode material during charging and discharging of lithium ion batteries has been mapped by atomic force microscopy (AFM) [101], reflecting accumulation of Vegard strain over both space and time. Likewise, electrochemical strain microscopy (ESM) is sensitive to local fluctuation in ionic and electronic defects, induced by changes in potential of a conductive scanning probe tip [10, 73, 120]. However, with all these techniques, it can be difficult to distinguish Vegard strain from other electromechanical effects, such as piezoelectric effect, electrostatic interactions, and capacitive forces [82, 21], and it is also quite challenging to carry out ESM in operando, due to the possible interference between the scanning probe potential and any global voltage perturbation applied to the system. Further information about scanning probe microscopy (SPM) techniques based on dynamic strain measurement can be found in a recent review [65]. In this work, we present results of a new technique to probe local electrochemistry at the nanoscale, scanning thermo-ionic microscopy (STIM), which is based on imaging of thermally induced Vegard strain. In contrast to ESM, our method is based on the fluctuation of ionic or electronic defect concentrations caused directly or indirectly by temperature fluctuations induced by a heated scanning probe. As a result, STIM has several potential advantages over ESM. First, the heated probe is electrically insulated from the sample and thus the measurement is not complicated by other electromechanical mechanisms such as electrostatic interactions discussed earlier. STIM also easily distinguishes nonlinear strain associated with ionic and electronic defects from linear thermomechanical sources, such as thermal expansion, due to differences in harmonic responses. Thus, STIM gives us a clean method to probe local defect structure with high sensitivity and spatial resolution that is decoupled from other strain contributions, as well as allowing mapping of local thermomechanical response. This technique can be applied to investigate a wide range of electrochemical systems including electrode materials for lithium ion batteries and solid oxide electrolysis and fuel cells. Initial results on LiFePO4 and Sm-doped Ceria

are presented here as examples.

7.2 Principle and Method

Many solids exhibit Vegard strain defined broadly as a lattice volume change associated with a change in the concentration of one or more ionic or electronic defects [31, 105]. While mechanical deformation is generally not desirable for the operation of lithium ion batteries and other solid state electrochemical devices, such strain provide an alternative imaging mechanism to probe local ionic activities with high spatial resolution, as demonstrated by ESM [10, 73, 120]. From thermodynamic point of view, Vegard strain induced by concentration changes also suggests a converse effect, that diffusion of ionic and electronic species can be driven by gradients in hydrostatic stress in addition to gradients in concentration c and electric potential ϕ. Such a theory has been developed by Larch and Cahn in the 1970s [60, 36],

$$\frac{\partial c}{\partial t} = \nabla \cdot \left(D \nabla c \right) + \nabla \cdot \left(\frac{DFz}{RT} c \nabla \phi \right) - \nabla \cdot \left(\frac{D\Omega}{RT} c \nabla \sigma_h \right) \tag{7.1}$$

where D, z, and ϕ are the diffusivity, charge, and partial molar volume of a defect, F and R are Faraday's constant and the ideal gas constant, and T and t are absolute temperature and time, respectively.Chap7 Note that the principle of ESM is based on electro-migration, the second term in Eq. 7.1. What we are interested in here is if we can utilize diffusion driven by the stress gradient, the third term in the equation, for the imaging, which would allow us to overcome a number of difficulties associated with ESM, especially the coupling with other electromechanical contributions. The most straightforward method of applying local oscillating stress is vibrating the scanning probe mechanically. However, this implementation complicates the measurement of the resulting displacement, and also severely limits the magnitude of stresses possible. As shown in Figure 1(a), an alternative strategy is to impose

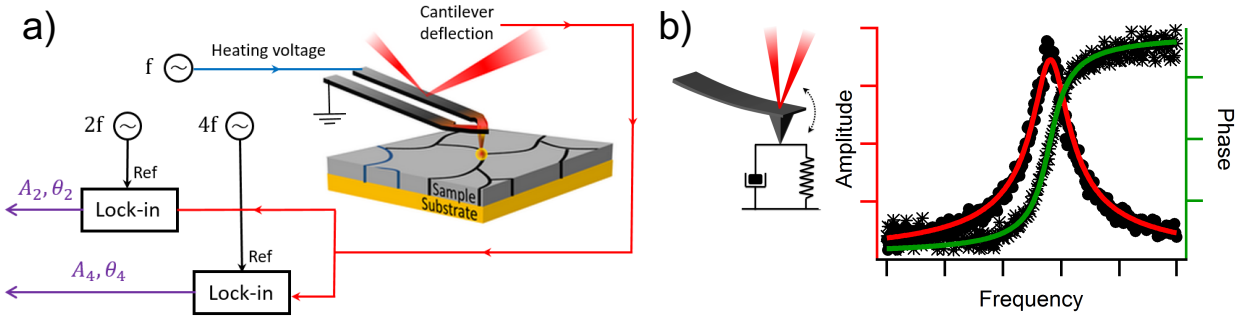

Figure 7.1: The schematics of STIM; (a) the heated scanning probe is driven by an AC current at frequency f, while the second and fourth harmonics of resulted cantilever vibrations are measured, reflecting local thermal expansion and thermo-ionic activities, respectively; (b) the cantilever vibration can be approximated as a damped driven harmonic oscillator, enabling quantitative analysis near resonance with high sensitivity.

stress locally by heating the sample through a thermal probe [57, 62], by passing an AC current through the microfabricated resistor localized on top of the tip. In this method, the thermal probe is heated by a sinusoidal current $I[\omega t] = I_0 cos(\omega t)$ at an angular frequency $\omega = 2\pi f$. With resistance β, the resulted power dissipation p is given by,

$$p[2\omega t] = \beta I^2 = \frac{I_0^2 \beta}{2}(1 + cos[2\omega t]) \tag{7.2}$$

which generates a second harmonic temperature oscillation under the heated probe around average temperature rise ΔT_{DC},

$$\Delta T[2\omega t] = \Delta T_{DC} + \Delta T_{AC} cos[2\omega t + \phi] \tag{7.3}$$

where θ is the phase delay. Such local temperature variation in turn produces a concentrated

thermal expansion strain $\boldsymbol{\varepsilon}^*$ and thus thermal stress $\boldsymbol{\sigma}$ at the second harmonics,

$$\boldsymbol{\varepsilon}^*[2\omega t] = \alpha \Delta T[2\omega t]\boldsymbol{I}, \quad \boldsymbol{\sigma}[2\omega t] = \boldsymbol{C}\big(\boldsymbol{\varepsilon}^* - \boldsymbol{\varepsilon}[2\omega t]\big), \tag{7.4}$$

where α and $\boldsymbol{C}$ are the thermal expansion coefficient and stiffness tensor of the material, $\boldsymbol{\varepsilon}$ is the total strain consisting of thermal strain and elastic strain, and $\boldsymbol{I}$ is a second rank unit tensor. Now substituting Eq. 7.4 into 7.1, and expanding T into Taylor series around averaging temperature T_0, we obtain the local concentration oscillation driven by the thermal probe,

$$\frac{\partial c}{\partial t} = -\nabla \cdot \left(\frac{D\Omega}{RT_0}\big(1 - \frac{\Delta T[2\omega t]}{T_0}\big) c_0 \nabla \big(\frac{1}{3}\mathrm{tr}(\boldsymbol{C}(\boldsymbol{\varepsilon}) - \alpha \Delta T[2\omega]\boldsymbol{I})\big) \right) \tag{7.5}$$

From Eq. 7.5, it is evident that the local concentration fluctuation Δc has a second harmonic component as,

$$\Delta c[2\omega t] = -\nabla \cdot \left(\frac{D\Omega}{RT_0} c_0 \nabla \big(\frac{1}{3}\mathrm{tr}(\boldsymbol{C}(\boldsymbol{\varepsilon}) - \alpha \Delta T[2\omega]\boldsymbol{I})\big) \right) \tag{7.6}$$

and a forth harmonics component as,

$$\Delta c[4\omega t] = \nabla \cdot \left(\frac{D\Omega}{RT_0^2} \Delta T[2\omega t] c_0 \nabla \big(\frac{1}{3}\mathrm{tr}(\boldsymbol{C}(\boldsymbol{\varepsilon}) - \alpha \Delta T[2\omega]\boldsymbol{I})\big) \right) \tag{7.7}$$

which translate into second and forth harmonic Vegard strains that can be measured through cantilever vibrations, as schematically shown in Fig. 1(a). Note that the second harmonic vibration consists of contributions from both thermal expansion and Vegard strain, as revealed by Eqs. 7.4 and 7.6, and is generally dominated by thermal expansion. However, the fourth harmonic response can only arise from the nonlinear contributions of Vegard strain, and thus can be used to unambiguously detect shifts in defect concentration. It is this sensitivity of the higher harmonic response to shifts in defect concentration that forms the underlying principle of STIM. It should be noted that the third term in Eq. 7.1 is only one of many

possible sources of nonlinear response associated with shifts in defect concentration. Others not treated here include thermally-induced defect formation and thermally driven transport (Soret/Dufour effects). However, like strain-driven transport we expect strong contributions from these sources to appear in the 4th and higher order harmonic response, and thus high sensitivity of STIM to local shifts in defect concentration.

7.3 Results and Discussions

Our current implementation of STIM utilizes an Asylum Research MFP-3D AFM using Anasys ThermaLever AN2-300 thermal probe. The cantilever-sample contact resonance is determined as f_0 first, and then the thermal probe is driven at $f_0/2$ and $f_0/4$, respectively, with the corresponding cantilever vibration measured at contact resonant frequency f_0 using lock-in to enhance the sensitivity. These give us the second and forth harmonic responses that correspond to local thermal expansion and thermoionic activities, respectively, as demonstrated by Eqs. (4-7). To verify the concept of STIM, we first examine the harmonic responses of two types of samples, one is Sm-doped ceria, a polycrystalline solid containing both ionic and electronic defect, and the other is polytetrafluoroethylene (PTFE), an insulating polymer which serves as the control. As discussed earlier, the second harmonic response is dominated by thermal expansion that is universal in all materials, and this is indeed what we observe in both Ceria and PTFE, as shown in Fig. 2(a), where prominent resonant peaks are evident in both systems. Note that Ceria is stiffer, and thus has higher contact stiffness and resonant frequency. On the other hand, as shown in Fig. 2(b), the fourth harmonic response, which we expect to be sensitive to shifts in defect concentration, is observed much more strongly in ceria. This results demonstrates the feasibility using STIM to image thermionic activities. Another consequence of Eq. 7.5 is that the STIM response is correlated with baseline concentration c_0, which can be manipulated by contact force im-

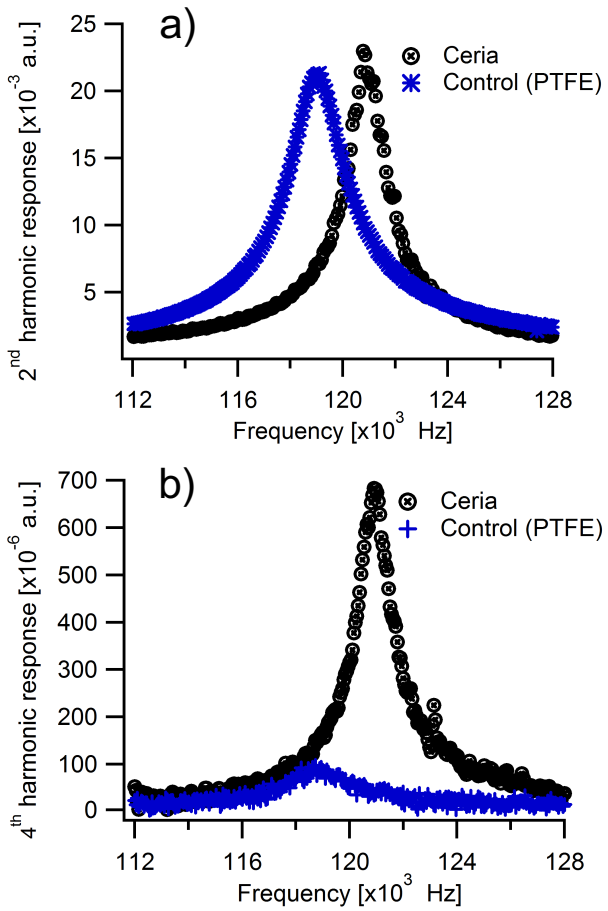

Figure 7.2: Comparison of (a) second and (b) forth harmonic responses of Ceria and PTFE, demonstrating the feasibility of STIM.

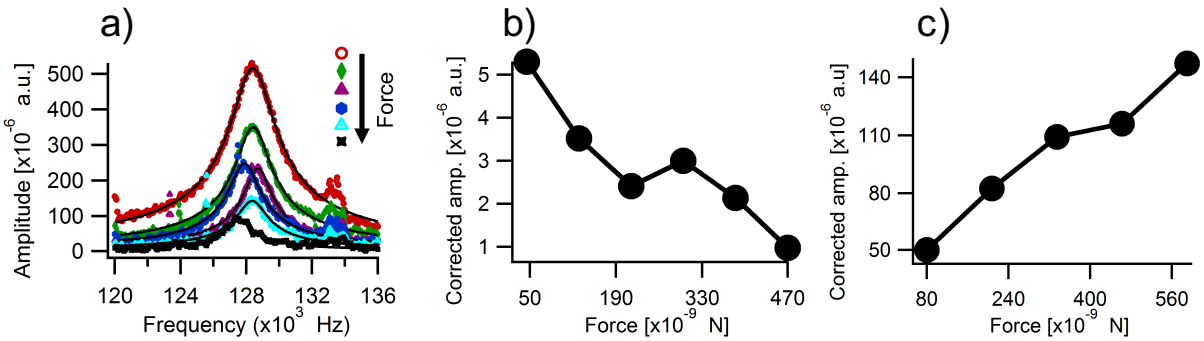

Figure 7.3: The effect of contact force on STIM responses; (a) STIM responses of Ceria under different contact forces; (b) corrected STIM amplitude of Ceria versus applied force; (c) corrected PFM amplitude of lithium niobate versus applied force.

posed by the thermal probe, a larger contact force would increase the chemical potential, and thus reduce c_0 underneath the probe, resulting in reduced STIM amplitude. This is in contrast to piezoresponse force microscopy (PFM), for example, wherein larger contact force improves electric contact between the conductive probe and sample, and thus enhances the PFM amplitude within certain extent. To verify this analysis, we probe STIM response of Ceria under different contact forces, as shown in Fig. 3(a), and it is observed that the peak amplitude does decrease with increased force. To see this more clearly, the response versus frequency is fitted using the damped driven harmonic oscillator model (Fig. 1b) [37, 37], and the intrinsic amplitude, derived from the peak amplitude at resonance divided by quality factor, is plotted versus contact force (Fig. 3b). The overall decreasing trend with increased contact force is evident in STIM, as expected. Similar measurement is also carried out on lithium niobate using PFM for comparison, which exhibits an opposite trend (Fig. 3c), that higher contact force results in better electric contact, and thus higher PFM response. It is well known that nanocrystalline Ceria exhibits total conductivity that is orders of magnitude higher than bulk Ceria [103], currently understood to be caused by accumulation of mobile electrons in the diffuse space charge regions near the surface and at grain bound-

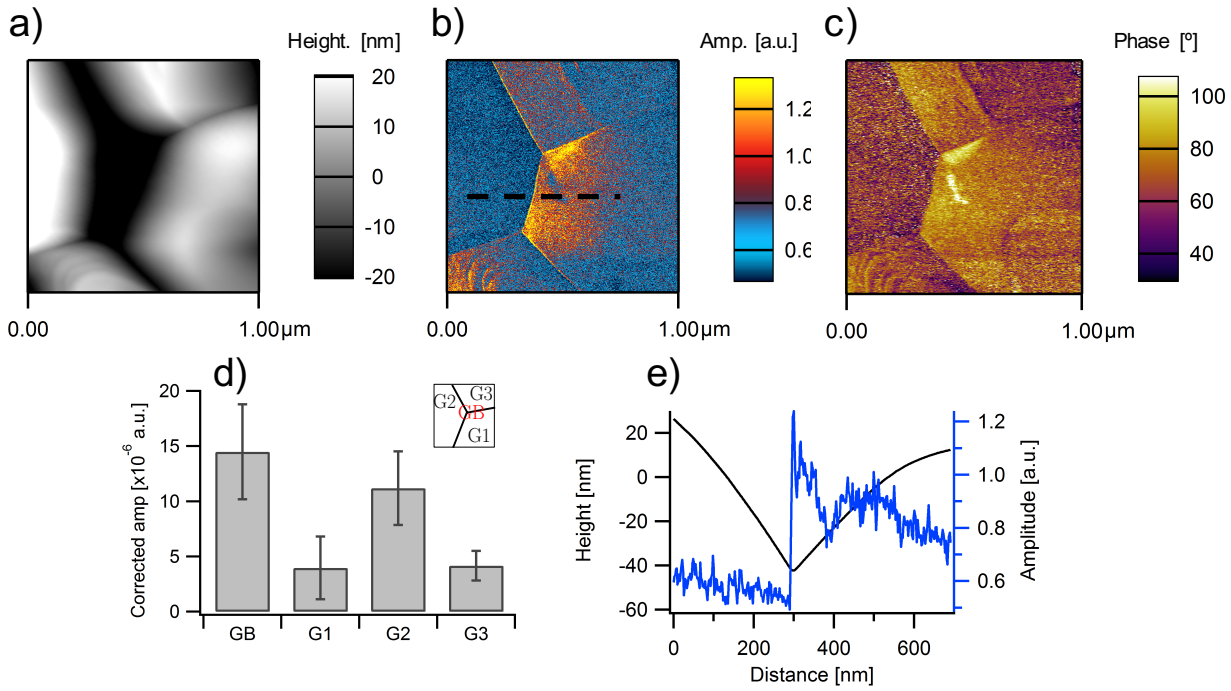

Figure 7.4: STIM Mapping of Ceria; (a) topography; (b) amplitude; (c) phase; and (d) comparison of corrected STIM amplitudes at grain boundaries and within grains.

aries [104, 24], as recently imaged by ESM [19]. Using STIM, we have mapped the fourth harmonic response of Ceria as well. The topography mapping in Fig. 4(a) reveals clear grain boundaries at junctions of four grains. The STIM amplitude mapping in Fig. 4(b) shows not only higher response at the grain boundaries, but also different responses in different grains, suggesting its dependence on grain orientation. The phase mapping in Fig. 4(c) exhibits little variation, as expected, since the phase delay is not supposed to be reversed for thermo-ionic activities, unlike PFM mapping of ferroelectric domains with opposite polarization. It is worth pointing out that during the STIM scanning, a single frequency method at resonance is used without tracking its variation, with fixed force. As such, crosstalk with topography cannot be eliminated. Either dual frequency resonance tracking [88] or band excitation [49] techniques can be used to solve this problem. However, we are running out of available lock-ins for tracking in our current system, and this is a minor technical difficulty that we will overcome in the future implementation. In order to accurately reflect their different responses, we compare corrected amplitude at grain boundary and within grains (Fig. 4d), averaged over ten different points probed in each area, and the higher STIM response at grain boundary is evident, due to the accumulation of space charges. This is consistent with ESM mapping we reported earlier [73]. STIM can also be applied to study electrode materials for lithium ion batteries as well, and we use $LiFePO_4$ as an example. The fourth harmonic amplitude and phase versus driving frequency is shown in Fig. 5(a), exhibiting a clear resonant peak as expected in any ionic system. The topography mapping is shown in Fig. 5(b), wherein grain structure is evident. The STIM amplitude mapping in Fig. 5(c) again reveals higher response near grain boundaries, consistent with what we observed before using ESM 38, though some of the regions inside grains have significant STIM response as well. As such, this technique can be applied to study a wide range of electrochemical systems.

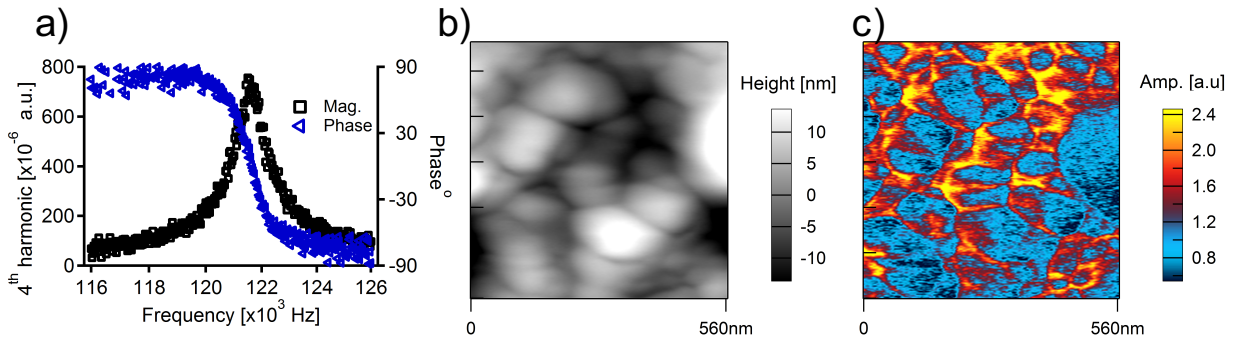

Figure 7.5: STIM Mapping of $LiFePO_4$; (a) amplitude and phase versus driving frequency; (b) topography mapping; and (c) amplitude mapping.

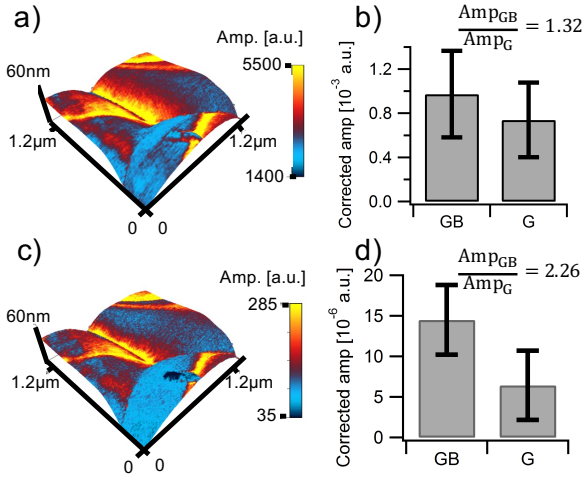

Figure 7.6: STIM amplitude mapping overlaid on topography and comparison of corrected STIM amplitudes at grain boundaries and within grains in ceria for a,b) second harmonic and c,d) forth harmonic responses.

7.4 Conclusion

In the past few years, it has been realized that electrically induced Vegard strain can provide an effective imaging mechanism for electrochemical processes with high spatial resolution, though it is difficult to distinguish Vegard strain from other electromechanical sources. In this chapter, a new STIM technique to probe local electrochemistry at the nanoscale via imaging of thermally induced Vegard strain, based on the fluctuation of defect concentrations resulting from local temperature oscillations driven by a heated scanning probe was developed. The thermal probe was electrically insulated from the sample and thus there was no electric interference as in ESM, and the measurement is not complicated by electrostatic forces or other electromechanical mechanisms. By decoupling second harmonic thermal expansion and forth harmonic Vegard strain, both local thermomechanical and electrochemical properties can be mapped, and it was applied to probe Sm-doped Ceria and $LiFePO_4$, revealing higher defect activity near grain boundaries. The STIM gives us a powerful method to probe local electrochemistry with high sensitivity and spatial resolution, and it can be applied to investigate a wide range of electrochemical systems

Chapter 8

CONCLUSION AND FUTURE WORK

8.1 Conclusion

This dissertation was focused on the effect of couplings between ionic diffusion and mechanics in battery electrode materials. In 3.7 a thermodynamics-based modeling framework for the ionic motion as well as surface kinetics was presented. This model considered the effect of entropy as well as the mechanical energy involved in insertion of atoms into the lattice host. Also the surface reaction model is adopted as a chemical potential dependent Arrhenius kinetics. The resulted governing equations recognize a maximum concentration and coupling between mechanics and electrochemistry.

In Chapters 3 and 4 the governing equations are solved numerically for battery electrodes with heterogeneity and various boundary mechanical/electrochemical conditions. The ionic motion in homogenous electrodes as well as electrodes with periodic inhomegenouties are numerically modeled and the effect of coupling to mechanics is investigated. Also, the governing equations were implemented into the Comsol finite element platform to model the performance of electrodes with different boundary conditions and geometries. Three electrode geometries were considered and compared their charging capacities that showed a relation between their stress level and the ultimate capacities.

The results motivated the next Chapter 5, for optimizing a battery electrode geometry that shows an optimum performance. In this chapter a framework for the optimization was introduced and the considered electrode geometries with three design variables were introduced. The effect of design variables on the ultimate capacity and the charging time

were investigated to find a geometry with optimum performance.

Another important aspect of the coupling between electrochemistry and mechanics in nano-scale characterizations is considered in Chapter 6. A method to probe the electrochemical in batteries using biased probe in atomic force microscopy was investigated using modeling and experiment in this chapter. The electrostatics physics is added the to the previous Comsol model to simulate this technique. Various aspects of the characterizations were modeled and an experimental evaluation experiments were also conducted for comparison with modeling results.

The Shortcomings involved in the ESM measurements motived me to invent a new method based on the understanding from the coupled physics of ionic motion. In Chapter 7, the mathematical foundations of the new method is described in details. In the new method, temperature variations of the AFM tip is used with the coupling between ionic motion and mechanics to probe the electrochemical activities. This method resolves the complications with applying electric potential to the tip such as electrostatic effect, dipole effect and others.

8.2 Future work

The mathematical modeling framework and the numerical implementations in this dissertation provide the required tools for investigating battery electrodes. While intercalation of ions into many electrodes follows the considered model, there are some electrodes that have more complicated behaviors. For instance Silicon, which is a candidate for future of high capacity electrodes experiences phase transformation due to insertion of ions. Such behaviors are required to be considered for future modelings of these electrodes. Also the material properties considered in this study are necessary to be determined preciesly from characterization experiments for better predictions. Furthermore, the numerical implementation and analysis of the structured electrodes could be extended for 3D structures with possibly more

improvements in the performance.

The Electrochemical Strain Microscopy is proved in recent years to be a powerful technique to probe the electrochemical activities at the nano-scale. The ESM signal formation due to electrochemical activities mechanism is confirmed in this dissertation by modeling and experimentation. However there are many other sources that can contribute to the overall signal detected in different materials. Therefore, it is critical for the development of this technique to be able to separate other contributions from the electrochemical response. A particular contributing mechanism is electrostatic effects between probe and sample surface. There are some preliminary experimental works on separating contributions by the relations by looking at the linear and quadratic responses which separates the contributions from linear mechanisms such as ferroelectric and Vegard strain and nonlinear mechanisms such as electro-strictive. Such experiments are still vague and the contributions are not throughly understood. Therefore, a comprehensive mathematical model that considers all the possible contributing mechanisms is required to design experimental techniques that could separate the signal of interest.

The recently developed Scanning Thermo-Ionic Microscopy, developed in this dissertation, has showed promising preliminary results. In order to further verify this technique, many more experimental investigations are required to be conducted and compare to the current understanding of the electrochemical activities. In this technique the output signal is known to be from the electrochemical activities including the ionic concentration and diffusivity. A possible direction of experiments is to develop spectroscopy techniques that could separate the diffusivity from concentration of ions by measuring ionic redistribution time. The preliminary results of experiments on this aspect of the technique have verified the concept. Furthermore, we presented the mathematical analysis for one possible source of the of the nonlinear response in the STIM technique. However there are other sources, such as

thermally-induced defect formation and thermally driven transport (Soret/Dufour effects), that can contribute to the signal. Expanding the analysis and modeling of the technique is rather essential to appreciate the effect of all contributions and possibly design of new experiments.

BIBLIOGRAPHY

[1] SB Adler. Factors governing oxygen reduction in solid oxide fuel cell cathodes. *Chemical reviews*, 104(10):4791–4844, 2004.

[2] Katerina E Aifantis, Stephen A Hackney, and R Vasant Kumar. *High energy density lithium batteries: materials, engineering, applications*. John Wiley & Sons, 2010.

[3] S Amemiya, AJ Bard, FRF Fan, and MV Mirkin. Scanning electrochemical microscopy. *Annual Review of Analytical Chemistry*, 1(1):95–131, 2008.

[4] Antonino Salvatore Arico, Peter Bruce, Bruno Scrosati, Jean-Marie Tarascon, and Walter Van Schalkwijk. Nanostructured materials for advanced energy conversion and storage devices. *Nature materials*, 4(5):366–377, 2005.

[5] Michel Armand and J-M Tarascon. Building better batteries. *Nature*, 451(7179):652–657, 2008.

[6] Pankaj Arora, Ralph E White, and Marc Doyle. Capacity fade mechanisms and side reactions in lithium-ion batteries. *Journal of the Electrochemical Society*, 145(10):3647–3667, 1998.

[7] Ali Awarke, Sven Lauer, Michael Wittler, and Stefan Pischinger. Quantifying the effects of strains on the conductivity and porosity of lifepo¡ sub¿ 4¡/sub¿ based li-ion composite cathodes using a multi-scale approach. *Computational Materials Science*, 50(3):871–879, 2011.

[8] Michael J Aziz, Paul C Sabin, and Guo-Quan Lu. The activation strain tensor: nonhydrostatic stress effects on crystal-growth kinetics. *Physical Review B*, 44(18):9812, 1991.

[9] N Balke, S Jesse, AN Morozovska, E Eliseev, DW Chung, Y Kim, L Adamczyk, RE Garcia, N Dudney, and SV Kalinin. Nanoscale mapping of ion diffusion in a lithium-ion battery cathode. *Nature Nanotechnology*, 5(10):749–754, 2010.

[10] Nina Balke, Stephen Jesse, Yoongu Kim, Leslie Adamczyk, Alexander Tselev, Ilia N Ivanov, Nancy J Dudney, and Sergei V Kalinin. Real space mapping of Li-ion transport

in amorphous Si anodes with nanometer resolution. *Nano letters*, 10(9):3420–5, sep 2010.

[11] Nina Balke, Stephen Jesse, Yoongu Kim, Leslie Adamczyk, Alexander Tselev, Ilia N Ivanov, Nancy J Dudney, and Sergei V Kalinin. Real space mapping of li-ion transport in amorphous si anodes with nanometer resolution. *Nano letters*, 10(9):3420–3425, 2010.

[12] AJ Bard and MV Mirkin. *Scanning electrochemical microscopy*. CRC Press, 2012.

[13] Anna L. Barker, Marylou Gonsalves, Julie V. Macpherson, Christopher J. Slevin, and Patrick R. Unwin. Scanning electrochemical microscopy: beyond the solid/liquid interface. *Analytica Chimica Acta*, 385(1):223–240, 1999.

[14] LY Beaulieu, KW Eberman, RL Turner, LJ Krause, and JR Dahn. Colossal reversible volume changes in lithium alloys. *Electrochemical and Solid-State Letters*, 4(9):A137–A140, 2001.

[15] Esther Bohn, Thomas Eckl, Marc Kamlah, and Robert McMeeking. A model for lithium diffusion and stress generation in an intercalation storage particle with phase change. *Journal of The Electrochemical Society*, 160(10):A1638–A1652, 2013.

[16] BA Boukamp, GC Lesh, and RA Huggins. All-solid lithium electrodes with mixed-conductor matrix. *Journal of the Electrochemical Society*, 128(4):725–729, 1981.

[17] John Cannarella and Craig B Arnold. Stress evolution and capacity fade in constrained lithium-ion pouch cells. *Journal of Power Sources*, 245:745–751, 2014.

[18] Candace K Chan, Hailin Peng, Gao Liu, Kevin McIlwrath, Xiao Feng Zhang, Robert A Huggins, and Yi Cui. High-performance lithium battery anodes using silicon nanowires. *Nature nanotechnology*, 3(1):31–35, 2007.

[19] Qian Nataly Chen, Stuart B. Adler, and Jiangyu Li. Imaging space charge regions in Sm-doped ceria using electrochemical strain microscopy. *Applied Physics Letters*, 105(20):201602, nov 2014.

[20] Qian Nataly Chen, Yun Ou, Feiyue Ma, and Jiangyu Li. Mechanisms of electromechanical coupling in strain based scanning probe microscopy. *Applied Physics Letters*, 104(24):242907, 2014.

[21] Qian Nataly Chen, Yun Ou, Feiyue Ma, and Jiangyu Li. Mechanisms of Electromechanical Coupling in Strain Based Scanning Probe Microscopy. *Applied Physics Letters*, 104(24), 2014.

[22] Yang-Tse Cheng and Mark W Verbrugge. Evolution of stress within a spherical insertion electrode particle under potentiostatic and galvanostatic operation. *Journal of Power Sources*, 190(2):453–460, 2009.

[23] Yang-Tse Cheng and Mark W Verbrugge. Diffusion-induced stress, interfacial charge transfer, and criteria for avoiding crack initiation of electrode particles. *Journal of the Electrochemical Society*, 157(4):A508–A516, 2010.

[24] Y.-M. Chiang, E.B. Lavik, and D.A. Blom. Defect thermodynamics and electrical properties of nanocrystalline oxides: pure and doped CeO2. *Nanostructured Materials*, 9(1):633–642, 1997.

[25] Jaephil Cho, Geun Bae Kim, Hong Sup Lim, Chan-Soo Kim, and Sang-Im Yoo. Improvement of structural stability of limn2 o 4 cathode material on 55 c cycling by sol-gel coating of licoo2. *Electrochemical and Solid-State Letters*, 2(12):607–609, 1999.

[26] John Christensen and John Newman. A mathematical model of stress generation and fracture in lithium manganese oxide. *Journal of The Electrochemical Society*, 153(6):A1019–A1030, 2006.

[27] John Christensen and John Newman. Stress generation and fracture in lithium insertion materials. *Journal of Solid State Electrochemistry*, 10(5):293–319, 2006.

[28] EJ Crumlin, E Mutoro, SJ Ahn, and GJ la O'. Oxygen reduction kinetics enhancement on a heterostructured oxide surface for solid oxide fuel cells. *The Journal of*, 1(21):1948–7185, 2010.

[29] Zhiwei Cui, Feng Gao, and Jianmin Qu. A finite deformation stress-dependent chemical potential and its applications to lithium ion batteries. *Journal of the Mechanics and Physics of Solids*, 60(7):1280–1295, 2012.

[30] WIF David, MM Thackeray, LA De Picciotto, and JB Goodenough. Structure refinement of the spinel-related phases li2mn2o4 and li0.2mn2o4. *Journal of Solid State Chemistry*, 67(2):316–323, 1987.

[31] A. R. Denton and N. W. Ashcroft. Vegard's law. *Physical Review A*, 43(6):3161–3164, mar 1991.

[32] Gaelle Derrien, Jusef Hassoun, Stefania Panero, and Bruno Scrosati. Nanostructured sn–c composite as an advanced anode material in high-performance lithium-ion batteries. *Advanced Materials*, 19(17):2336–2340, 2007.

[33] Rutooj Deshpande, Yang-Tse Cheng, and Mark W Verbrugge. Modeling diffusion-induced stress in nanowire electrode structures. *Journal of Power Sources*, 195(15):5081–5088, 2010.

[34] N Ding, J Xu, YX Yao, Gerhard Wegner, X Fang, CH Chen, and Ingo Lieberwirth. Determination of the diffusion coefficient of lithium ions in nano-si. *Solid State Ionics*, 180(2):222–225, 2009.

[35] Marc Doyle, Thomas F Fuller, and John Newman. Modeling of galvanostatic charge and discharge of the lithium/polymer/insertion cell. *Journal of the Electrochemical Society*, 140(6):1526–1533, 1993.

[36] Ahmadreza Eshghinejad. The coupled lithium ion diffusion and stress in battery electrodes. *Mechanics of Materials*, 91:343–350, 2015.

[37] A Gannepalli, D G Yablon, A H Tsou, and R Proksch. Mapping nanoscale elasticity and dissipation using dual frequency contact resonance AFM. *Nanotechnology*, 22(35):355705, sep 2011.

[38] R Edwin Garcia, Yet-Ming Chiang, W Craig Carter, Pimpa Limthongkul, and Catherine M Bishop. Microstructural modeling and design of rechargeable lithium-ion batteries. *Journal of The Electrochemical Society*, 152(1):A255–A263, 2005.

[39] Mino Green, Elizabeth Fielder, Bruno Scrosati, Mario Wachtler, and Judith Serra Moreno. Structured silicon anodes for lithium battery applications. *Electrochemical and Solid-State Letters*, 6(5):A75–A79, 2003.

[40] Alexei Gruverman, Orlando Auciello, and Hiroshi Tokumoto. Imaging and control of domain structures in ferroelectric thin films via scanning force microscopy. *Annual review of materials science*, 28(1):101–123, 1998.

[41] Hamed Haftbaradaran, Huajian Gao, and WA Curtin. A surface locking instability for atomic intercalation into a solid electrode. *Applied Physics Letters*, 96(9):091909, 2010.

[42] Hamed Haftbaradaran, Jun Song, WA Curtin, and Huajian Gao. Continuum and atomistic models of strongly coupled diffusion, stress, and solute concentration. *Journal of Power Sources*, 196(1):361–370, 2011.

[43] JW Han and B Yildiz. Mechanism for enhanced oxygen reduction kinetics at the (La, Sr) CoO 3 δ/(La, Sr) 2 CoO 4+ δ hetero-interface. *Energy & Environmental Science*, 5(9):8598–8607, 2012.

[44] JW Han and B Yildiz. Mechanism for enhanced oxygen reduction kinetics at the (La, Sr) CoO 3 δ/(La, Sr) 2 CoO 4+ δ hetero-interface. *Energy & Environmental Science*, 5(9):8598–8607, 2012.

[45] Linda L Horton. Basic research needs to assure a secure energy future. *Energy*, 2002.

[46] Yuhang Hu, Xuanhe Zhao, and Zhigang Suo. Averting cracks caused by insertion reaction in lithium–ion batteries. *Journal of Materials Research*, 25(06):1007–1010, 2010.

[47] RA Huggins and WD Nix. Decrepitation model for capacity loss during cycling of alloys in rechargeable electrochemical systems. *Ionics*, 6(1-2):57–63, 2000.

[48] Robert Huggins. *Advanced batteries: materials science aspects*. Springer Science & Business Media, 2008.

[49] Stephen Jesse, Sergei V Kalinin, Roger Proksch, A P Baddorf, and B J Rodriguez. The band excitation method in scanning probe microscopy for rapid mapping of energy dissipation on the nanoscale. *Nanotechnology*, 18(43):435503, oct 2007.

[50] Stephen Jesse, Sergei V Kalinin, Roger Proksch, AP Baddorf, and BJ Rodriguez. The band excitation method in scanning probe microscopy for rapid mapping of energy dissipation on the nanoscale. *Nanotechnology*, 18(43):435503, 2007.

[51] Stephen Jesse, Boris Mirman, and Sergei V Kalinin. Resonance enhancement in piezoresponse force microscopy: Mapping electromechanical activity, contact stiffness, and Q factor. *Applied physics letters*, 89(2):022906, 2006.

[52] WC Jung and HL Tuller. Investigation of surface Sr segregation in model thin film solid oxide fuel cell perovskite electrodes. *Energy & Environmental Science*, 5(1):5370–5378, 2012.

[53] Sergei V. Kalinin and Nina Balke. Local Electrochemical Functionality in Energy Storage Materials and Devices by Scanning Probe Microscopies: Status and Perspectives. *Advanced Materials*, 22(35):E193–E209, sep 2010.

[54] S. Kalnaus, K. Rhodes, and C. Daniel. A study of lithium ion intercalation induced fracture of silicon particles used as anode material in Li-ion battery. *Journal of Power Sources*, 196(19):8116–8124, 2011.

[55] Uday Kasavajjula, Chunsheng Wang, and A John Appleby. Nano-and bulk-silicon-based insertion anodes for lithium-ion secondary cells. *Journal of Power Sources*, 163(2):1003–1039, 2007.

[56] Sangtae Kim, Soon Ju Choi, Kejie Zhao, Hui Yang, Giorgia Gobbi, Sulin Zhang, and Ju Li. Electrochemically driven mechanical energy harvesting. *Nature communications*, 7, 2016.

[57] William P. King, Thomas W. Kenny, Kenneth E. Goodson, Graham Cross, Michel Despont, Urs Durig, Hugo Rothuizen, Gerd K. Binnig, and Peter Vettiger. Atomic force microscope cantilevers for combined thermomechanical data writing and reading. *Applied Physics Letters*, 78(9):1300–1302, 2001.

[58] Robert Kostecki and Frank McLarnon. Microprobe study of the effect of li intercalation on the structure of graphite. *Journal of power sources*, 119:550–554, 2003.

[59] CR Kreller, TJ McDonald, and SB Adler. Origin of Enhanced Chemical Capacitance in La0. 8Sr0. 2CoO3-δ Thin Film Electrodes. *Journal of The Electrochemical Society*, 160(9):F931–F942, 2013.

[60] F Larché and J.W Cahn. A linear theory of thermochemical equilibrium of solids under stress. *Acta Metallurgica*, 21(8):1051–1063, 1973.

[61] F Larché and JW Cahn. A linear theory of thermochemical equilibrium of solids under stress. *Acta Metallurgica*, 21(8):1051–1063, 1973.

[62] Jungchul Lee, Thomas Beechem, Tanya L. Wright, Brent A. Nelson, Samuel Graham, and William P. King. Electrical, thermal, and mechanical characterization of silicon microcantilever heaters. *Journal of Microelectromechanical Systems*, 15(6):1644–1655, 2006.

[63] James Chen-Min Li. Physical chemistry of some microstructural phenomena. *Metallurgical Transactions A*, 9(10):1353–1380, 1978.

[64] JCM Li, RA Oriani, and LS Darken. The thermodynamics of stressed solids. *Zeitschrift für Physikalische Chemie*, 49(3_5):271–290, 1966.

[65] Jiangyu Li, Jing-Feng Li, Qi Yu, Qian Nataly Chen, and Shuhong Xie. Strain-based scanning probe microscopies for functional materials, biological structures, and electrochemical systems. *Journal of Materiomics*, 1(1):3–21, 2015.

[66] Juchuan Li, Alan K Dozier, Yunchao Li, Fuqian Yang, and Yang-Tse Cheng. Crack pattern formation in thin film lithium-ion battery electrodes. *Journal of The Electrochemical Society*, 158(6):A689–A694, 2011.

[67] Chang Liu, Feng Li, Lai-Peng Ma, and Hui-Ming Cheng. Advanced materials for energy storage. *Advanced materials*, 22(8), 2010.

[68] Ou Mao, RA Dunlap, and JR Dahn. Mechanically alloyed sn-fe (-c) powders as anode materials for li-ion batteries: I. the sn2fe-c system. *Journal of The Electrochemical Society*, 146(2):405–413, 1999.

[69] Matthew T McDowell, Seok Woo Lee, Chongmin Wang, William D Nix, and Yi Cui. Studying the kinetics of crystalline silicon nanoparticle lithiation with in situ transmission electron microscopy. *Advanced Materials*, 24(45):6034–6041, 2012.

[70] J.W. Park M.H. Kim, S.H. Ahn and J.A. Ascencio. Electrochemical characteristics of a si/ge multilayer anode for lithium-ion batteries. *Journal of the Korean Physical Society*, 49:1107–1110, 2006.

[71] Charilaos Mousoulis, Teimour Maleki, Babak Ziaie, and Corey P Neu. Atomic force microscopy-coupled microcoils for cellular-scale nuclear magnetic resonance spectroscopy. *Applied Physics Letters*, 102(14):143702, 2013.

[72] COMSOL Multiphysics. Livelink for matlab®. *User's guide, Version*, 4.

[73] Qian Nataly Chen, Yanyi Liu, Yuanming Liu, Shuhong Xie, Guozhong Cao, and Jiangyu Li. Delineating local electromigration for nanoscale probing of lithium ion intercalation and extraction by electrochemical strain microscopy. *Applied Physics Letters*, 101(6):2–7, 2012.

[74] GA Nazri and G Pistoia. *Lithium batteries: science and technology*. Springer Science & Business Media, 2008.

[75] Gholam-Abbas Nazri and Gianfranco Pistoia. *Lithium batteries: science and technology*. Springer Science & Business, 2008.

[76] John Newman and Karen E Thomas-Alyea. *Electrochemical systems*. John Wiley & Sons, 2012.

[77] D Oh and D Gostovic. Mechanism of La 0.6 Sr 0.4 Co 0.2 Fe 0.8 O 3 cathode degradation. *Journal of Materials Research*, 27(15):1992–1999, 2012.

[78] RP O'Hayre, SW Cha, W Colella, and FB Prinz. *Fuel cell fundamentals*. John Wiley & Sons, 2006.

[79] David L Olmsted, Rob Phillips, and WA Curtin. Modelling diffusion in crystals under high internal stress gradients. *Modelling and Simulation in Materials Science and Engineering*, 12(5):781, 2004.

[80] Jos FM Oudenhoven, Loïc Baggetto, and Peter HL Notten. All-solid-state lithium-ion microbatteries: A review of various three-dimensional concepts. *Advanced Energy Materials*, 1(1):10–33, 2011.

[81] P Poizot, S Laruelle, S Grugeon, and L Dupont. Nano-sized transition-metal oxides as negative-electrode materials for lithium-ion batteries. *Nature*, 407:496–499, 2000.

[82] R. Proksch. Electrochemical strain microscopy of silica glasses. *Journal of Applied Physics*, 116(6):066804, aug 2014.

[83] S Prussin. Generation and distribution of dislocations by solute diffusion. *Journal of Applied Physics*, 32(10):1876–1881, 1961.

[84] Nataly Chen Qian, Feiyue Ma, Shuhong Xie, Yuanming Liu, Roger Proksch, and Jiangyu Li. High sensitivity piezomagnetic force microscopy for quantitative probing of magnetic materials at the nanoscale. *Nanoscale*, 5(13):5747–5751, 2013.

[85] BV Ratnakumar, MC Smart, A Kindler, H Frank, R Ewell, and S Surampudi. Lithium batteries for aerospace applications: 2003 mars exploration rover. *Journal of power sources*, 119:906–910, 2003.

[86] Sindhuja Renganathan, Godfrey Sikha, Shriram Santhanagopalan, and Ralph E White. Theoretical analysis of stresses in a lithium ion cell. *Journal of the Electrochemical Society*, 157(2):A155–A163, 2010.

[87] Kevin Rhodes, Nancy Dudney, Edgar Lara-Curzio, and Claus Daniel. Understanding the degradation of silicon electrodes for lithium-ion batteries using acoustic emission. *Journal of the Electrochemical Society*, 157(12):A1354–A1360, 2010.

[88] Brian J Rodriguez, Clint Callahan, Sergei V Kalinin, and Roger Proksch. Dual-frequency resonance-tracking atomic force microscopy. *Nanotechnology*, 18(47):475504, nov 2007.

[89] Brian J Rodriguez, Clint Callahan, Sergei V Kalinin, and Roger Proksch. Dual-frequency resonance-tracking atomic force microscopy. *Nanotechnology*, 18(47):475504, 2007.

[90] M Sase, F Hermes, K Yashiro, and K Sato. Enhancement of oxygen surface exchange at the hetero-interface of (La, Sr) CoO3/(La, Sr) 2CoO4 with PLD-layered films. *Journal of the*, 155(8):B793–B797, 2008.

[91] M Sase, F Hermes, K Yashiro, and K Sato. Enhancement of oxygen surface exchange at the hetero-interface of (La, Sr) CoO3/(La, Sr) 2CoO4 with PLD-layered films. *Journal of the*, 155(8):B793–B797, 2008.

[92] A Sawa. Resistive switching in transition metal oxides. *Materials today*, 11(6):28–36, 2008.

[93] Bruno Scrosati and Jürgen Garche. Lithium batteries: Status, prospects and future. *Journal of Power Sources*, 195(9):2419–2430, 2010.

[94] P Sharma and TS Bhatti. A review on electrochemical double-layer capacitors. *Energy Conversion and Management*, 51(12):2901–2912, 2010.

[95] Gogi K Singh, Gerbrand Ceder, and Martin Z Bazant. Intercalation dynamics in rechargeable battery materials: General theory and phase-transformation waves in lifepo¡ sub¿ 4¡/sub¿. *Electrochimica Acta*, 53(26):7599–7613, 2008.

[96] MC Smart, BV Ratnakumar, LD Whitcanack, KB Chin, S Surampudi, R Gitzendanner, F Puglia, and J Byers. Lithium-ion batteries for aerospace. *IEEE Aerospace and Electronic Systems Magazine*, 19(1):18–25, 2004.

[97] DB Strukov, GS Snider, DR Stewart, and RS Williams. The missing memristor found. *nature*, 453:80–83, 2008.

[98] J-M Tarascon and Michel Armand. Issues and challenges facing rechargeable lithium batteries. *Nature*, 414(6861):359–367, 2001.

[99] J.M. Tarascon and M. Armand. Issues and challanges facing rechargeable lithium batteries. *Nature*, 414(November):359–367, 2001.

[100] Michael M Thackeray, Christopher S Johnson, John T Vaughey, N Li, and Stephen A Hackney. Advances in manganese-oxide compositeelectrodes for lithium-ion batteries. *Journal of Materials Chemistry*, 15(23):2257–2267, 2005.

[101] Ye Tian, Adam Timmons, and J. R. Dahn. In Situ AFM Measurements of the Expansion of Nanostructured SnCoC Films Reacting with Lithium. *Journal of The Electrochemical Society*, 156(3):A187, 2009.

[102] Georgios A Tritsaris, Efthimios Kaxiras, Sheng Meng, and Enge Wang. Adsorption and diffusion of lithium on layered silicon for li-ion storage. *Nano letters*, 13(5):2258–2263, 2013.

[103] Andreas Tschöpe, Jackie Y. Ying, and Harry L. Tuller. Catalytic redox activity and electrical conductivity of nanocrystalline non-stoichiometric cerium oxide. *Sensors and Actuators B: Chemical*, 31(1):111–114, 1996.

[104] Harry L. Tuller. Ionic conduction in nanocrystalline materials. *Solid State Ionics*, 131(1):143–157, 2000.

[105] L. Vegard. Die Konstitution der Mischkristalle und die Raumfullung der Atome. *Zeitschrift fur Physik*, 5(1):17–26, jan 1921.

[106] Mark W Verbrugge and Yang-Tse Cheng. Stress and strain-energy distributions within diffusion-controlled insertion-electrode particles subjected to periodic potential excitations. *Journal of the Electrochemical Society*, 156(11):A927–A937, 2009.

[107] Deyu Wang, Xiaodong Wu, Zhaoxiang Wang, and Liquan Chen. Cracking causing cyclic instability of lifepo 4 cathode material. *Journal of Power Sources*, 140(1):125–128, 2005.

[108] Haifeng Wang, Young-Il Jang, Biying Huang, Donald R Sadoway, and Yet-Ming Chiang. Tem study of electrochemical cycling-induced damage and disorder in licoo2 cathodes for rechargeable lithium batteries. *Journal of the Electrochemical Society*, 146(2):473–480, 1999.

[109] Peiqi Wang, Qian Nataly Chen, Shuhong Xie, Xiaoyan Liu, and Jiangyu Li. Enhanced lithium ion storage in nanoimprinted carbon. *Applied Physics Letters*, 107(4):043904, 2015.

[110] Martin Winter, Jürgen O Besenhard, Michael E Spahr, and Petr Novak. Insertion electrode materials for rechargeable lithium batteries. *Advanced materials*, 10(10):725–763, 1998.

[111] William H Woodford, Yet-Ming Chiang, and W Craig Carter. Electrochemical shock of intercalation electrodes: a fracture mechanics analysis. *Journal of the Electrochemical Society*, 157(10):A1052–A1059, 2010.

[112] Chien H Wu. The role of eshelby stress in composition-generated and stress-assisted diffusion. *Journal of the Mechanics and Physics of Solids*, 49(8):1771–1794, 2001.

[113] Fuqian Yang. Interaction between diffusion and chemical stresses. *Materials Science and Engineering: A*, 409(1):153–159, 2005.

[114] Wei-Jun Zhang. A review of the electrochemical performance of alloy anodes for lithium-ion batteries. *Journal of Power Sources*, 196(1):13–24, 2011.

[115] Wei-Jun Zhang. Lithium insertion/extraction mechanism in alloy anodes for lithium-ion batteries. *Journal of Power Sources*, 196(3):877–885, 2011.

[116] Xiangchun Zhang, Ann Marie Sastry, and Wei Shyy. Intercalation-induced stress and heat generation within single lithium-ion battery cathode particles. *Journal of The Electrochemical Society*, 155(7):A542–A552, 2008.

[117] Xiangchun Zhang, Wei Shyy, and Ann Marie Sastry. Numerical simulation of intercalation-induced stress in li-ion battery electrode particles. *Journal of the Electrochemical Society*, 154(10):A910–A916, 2007.

[118] Kejie Zhao, Matt Pharr, Joost J Vlassak, and Zhigang Suo. Fracture of electrodes in lithium-ion batteries caused by fast charging. *Journal of Applied Physics*, 108(7):073517, 2010.

[119] Kejie Zhao, Matt Pharr, Qiang Wan, Wei L Wang, Efthimios Kaxiras, Joost J Vlassak, and Zhigang Suo. Concurrent reaction and plasticity during initial lithiation of crystalline silicon in lithium-ion batteries. *Journal of The Electrochemical Society*, 159(3):A238–A243, 2012.

[120] Jing Zhu, Jinkui Feng, Li Lu, and Kaiyang Zeng. In situ study of topography, phase and volume changes of titanium dioxide anode in all-solid-state thin film lithium-ion battery by biased scanning probe microscopy. *Journal of Power Sources*, 197:224–230, jan 2012.